AD-A070 898 DYNETICS INC HUNTSVILLE ALA F/G 17/5
DESIGN OF IRSS PROJECTORS.(U)
NOV 78 DAAK40-78-C-0070
UNCLASSIFIED MIRADCOM-78-0070-022 NL

1 OF 2
AD
A070898

(2) LEVEL II

Dynetics, Inc.
P. O. DRAWER S
HUNTSVILLE, ALABAMA 35806

TR-78-MIRADCOM-0070-022

FINAL REPORT

DESIGN OF IRSS PROJECTORS

The views, opinions, and/or findings contained in this report are those of the author(s) and should not be construed as an official Department of the Army position, policy, or decision unless so designated by other official documentation.

30 NOVEMBER 1978

prepared for

U.S. ARMY MISSILE RESEARCH
AND DEVELOPMENT COMMAND
REDSTONE ARSENAL, ALABAMA 35809

DAAK40-78-C-0070

Dynetics, Inc.
P. O. DRAWER B
HUNTSVILLE, ALABAMA 35805

(18) TR-78-MIRADCOM-0070-022

(19) 78-0070-022

(9) FINAL REPORT. 30 Jan - 30 Nov 78

(6) DESIGN OF IRSS PROJECTORS

(11) 30 NOVEMBER 1978

(12) 166 p.

prepared for

U.S. ARMY MISSILE RESEARCH
AND DEVELOPMENT COMMAND
REDSTONE ARSENAL, ALABAMA 35809

(15) DAAK40-78-C-0070

TABLE OF CONTENTS

TABLE OF CONTENTS (Continued)

LIST OF ILLUSTRATIONS

LIST OF ILLUSTRATIONS (Concluded)

LIST OF TABLES

LIST OF TABLES (Concluded)

1. INTRODUCTION

This final report documents the efforts expended in performance of *Design of IRSS Projectors*, Contract DAAK40-78-C-0070, with the U.S. Army Missile Research and Development Command during the period 30 January 1978 to 30 November 1978. The report is organized into eight sections, of which this *Introduction* is one, plus supporting appendices. Following is Section 2., *Summary*, that outlines the salient study results and scope of the effort; Section 3., *Technical Background* details the basis of operation of the IRSS display system and projector set, Section 4., *Requirements*, which present the basis on which designs will be evaluated; Section 5., *Test and Evaluation*, a section which summarizes the findings of diagnostic tests performed on the projector-display system; These portions are followed by Section 6., *Analyses*, and Section 7., *Performance of Selected Concept*. These two sections describe analytically the capabilities of the present projector through development of a radiometric model, and demonstrate how performance is increased to meet the requirements by use of new components. Finally, in Section 8., *Recommendations*, are suggested additional tasks required to fully substantiate the recommended design.

In the five appendices are presented the mathematical details of (A) Radiometric Operations, (B) Vane Analyses, and (C) Mirror Analysis, all of which support the system analysis. Also, a brief analysis of the flare projector as applied to UV operation, and a discussion of high technology alternate projector concepts, are given.

2. SUMMARY

2.1 OBJECTIVE

New classes of optical homing anti-aircraft missiles, of which STINGER/POST is a prime example, utilize seekers capable of dual-mode operation, with a band at near-ultraviolet wavelengths in addition to the usual mid-IR band (normally between 3 and 5 μm). The thorough testing of these seekers requires that UV and IR scenes of the proper geometrical and radiometric relationships be presented to the seeker that is undergoing dynamical testing. In the Infrared Simulation System (IRSS), this requirement is fulfilled by implementing the principle of *compound projection*, by which each spatial portion of the target-background scene complex, including flare countermeasures, is spectrally projected and all portions are recombined at the seeker entrance pupil. This technique results in a composite scene in proper spatial registration.

Although some improvement could be recommended in the IR portions of the projection subsystem, the present systems function at a performance level adequate for testing most mid-IR seekers, including the IR mode of STINGER/POST. The UV-projector (actually, UV/visible) was found to correctly present the target-(fuselage)-background spatial relationships, but the radiance of both target and background as seen by the seeker was approximately twenty times lower than the minimum required to test STINGER/POST. Therefore, the foremost objective of the study was to develop design concepts capable of increasing the ultraviolet radiance levels of the target and background.

2.2 APPROACH

Many UV projector design concepts could be developed that would enable successful testing of STINGER/POST and similar seekers. These concepts range from relatively simple modifications to the present projector, conceivably involving nothing more than replacement of low-performing concepts, to advanced but immature concepts based upon obscure analytical formulations and employing devices and techniques still in laboratory development. In order to constrain the number of concepts to a manageable few and to establish a base for concept evaluation and final selection, a requirements hierarchy was developed. These requirements were categorized as *minimum*, *desirable*, and *optional*, with the last category including those requirements which, if implemented, would result in system functional simulation of second or third order effects. Several preliminary concepts that are responsive to these requirements were than evaluated, and the less promising concepts were rejected from further consideration and analysis.

While a significant parallel analysis was performed on advanced concepts, the major emphasis was placed on seeking the *minimum* modifications to the present projector that would meet the requirements. In this way, the goal of a low cost, minimum risk system design concept could evolve which could be verified and implemented in a timely manner. In order to achieve this goal, a significant portion of the total effort was allocated to test and analysis of the present projector, and subsequent development of a radiometrical model. Thus, by determining each components' contribution to

total radiance throughput, an assessment could be made of possible throughput increases achievable from new components or simple configuration changes.

2.3 RESULTS

The ability to quickly pinpoint design deficiencies in the projector was limited by incomplete documentation, specifications, and supporting analyses on both the original design and the modification that was later performed. Furthermore, lack of suitable optical instrumentation, including a radiometer uncalibrated in the band of interest, greatly compounded diagnostic problems. However, it was possible from analyses of the available data, to determine (using first order ray trace analysis) that the design of the UV projector was basically sound. The lens focal lengths and separation of components were correct for that configuration and entrance and exit pupils (stops) were correctly located. However, results of the radiometric measurements program indicated that the unexpectedly high losses in the UV band were repeated in the visible band. This fact obviated the possibility that a spectrally sensitive system component, such as a lens of UV opaque glass acting as an inadvertent filter, created the high losses. This led to an examination of components or phenomenology that were spectrally insensitive. The results of these examinations were used in the development of the projector radiance model, whose predicted results agreed quite well with the measured data. Analysis of modelled components demonstrated that the losses in the system are caused by the reflecting elements in the projector itself, principally the diffuse, low-reflectance, stainless-

steel transparency vanes in the background side, and the dielectric diffuser in the target side.

Several design concepts were analyzed and developed that would increase target and background radiance, but the recommended configuration completely fulfills the design requirements for POST missile testing while still meeting the program goals of a low-cost, minimum-risk configuration. This is achieved by only changing components and not by performing major modifications. The design changes are simply:

1. Use of semi-specular high reflectance vanes (with aluminum-coated, low-roughness ground glass as a baseline design component) for the background side, and a semi-specular dielectric transparency for the target side.
2. Dielectric mirrors in background projector leg.
3. Varian 800 watt xenon lamp with integral parabolic reflectors, with new condenser configuration and lens for the target leg.
4. Servo-controlled iris in target side.
5. Improved cloud wheel to dynamically adjust spatial radiance variations.
6. Deletion of mirrors in target side.

This new design will enable contrast ratios of one hundred percent to about four percent at cloud radiance levels of greater than 1 mW/cm^2-ster, between 0.35 μm and 0.40 μm. (Fresnel reflection and scattering from the target diffuser will always result in a residual target radiance, even with the target lamp off). In addition, lower values of background radiance typical of low-altitude clear blue sky (~400 $\mu W/cm^2$-ster) may be simulated

with the cloud wheel filter; target radiance (i.e., contrast) may be dynamically controlled during a simulated engagement by servo-control of the iris diaphragm. Finally, recommendations are presented for an evaluation of these concepts in subsequent programs.

3. TECHNICAL BACKGROUND

The IRSS is a complete simulation system that provides missile-seeker evaluation and test from launch to intercept. A view of the IRSS system is shown in Figure 3-1, as taken from Reference [3-1].

The functions of the IRSS target generation subsystem are to (1) maintain before the sensor under test a window into a target space whenever the sensor is tracking, (2) generate a spatially and spectrally complex target system whose geometry and spectral radiance characteristics appear as they would in a real-world scenario, (3) ensure that the radiation from the target scenes fill the sensor aperture completely and uniformly during the sensor tracking mission.

The target generation system is based on the principle of compound projection. That is, each scene element to be projected is generated by a separate projector. These scene elements are then superimposed in their proper relative spatial orientation in such a manner as to ensure filling the sensor entrance pupil. The composite image is formed on a special dimpled diffusing mirror that is located at the focal point of a spherical collimating mirror which intercepts the radiation from each of the projectors. The dimpled mirror expands the solid angle of radiation from each of the projectors to ensure filling the sensor aperture from each scene element. A second spherical collimating mirror than forms a virtual image of the combined scene elements at infinity.

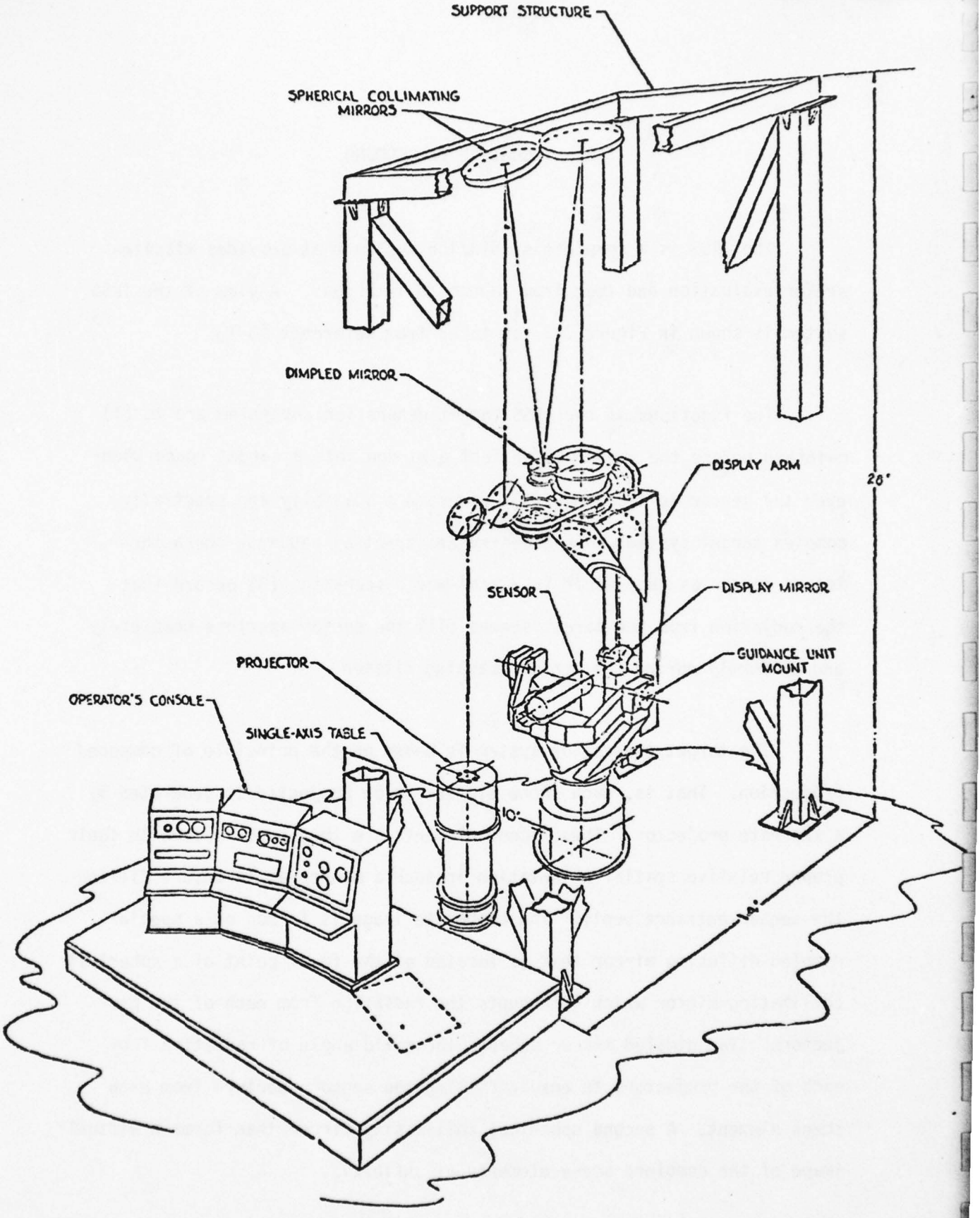

FIGURE 3-1. INFRARED SIMULATION SYSTEM

As mentioned earlier, the emphasis of this effort was to enhance the radiance transfer capacity of the UV/VIS background fuselage projector subsystem. The following section presents requirements for meeting the improvement goals.

4. REQUIREMENTS

4.1 REVIEW

Requirements for enhancing performance of the IRSS to accurately simulate signatures of typical tactical aircraft and ultraviolet sky backgrounds are presented in this section. The STINGER/POST system is used as a requirements guideline, but the general requirements are applicable to other seeker system designs based on UV detection and tracking of aircraft targets.

The spectral and spatial characteristics of the targets and backgrounds presented to the system must be indistinguishable from a real-world scenario, as perceived by the seeker under test. To ensure this, target size, shape, radiant intensity, and background radiance must be accurately simulated. Examination of the strictly kinematical requirements, as might be imposed by POST-type missile systems, was beyond the scope of this effort.

4.2 RADIANCE REQUIREMENTS FOR SIMULATED BACKGROUNDS

As discussed above, the minimum performance requirement for the UV/VIS background projector is to generate a background scene with an effective radiance commensurate with that of an actual blue sky background. In order to quantify the requirement, approximately thirty ultraviolet spectral radiance plots (available from General Dynamics/Pomona) of different background scenes were examined in order to determine average

radiance levels for typical scenes. Representative spectral curves are shown in Figure 4-1. Presented in Tables 4-1 and 4-2 are accumulations of tabulated data from the ultraviolet background radiance plots used to determine effective simulated background radiance requirements in the UV/VIS projector. It is seen that there is considerable overlap in the distribution functions, with some of the brightest sky radiances larger than the duller clouds, and vise-versa.

Analysis of this data indicates that an average (median) sky background scene can be simulated if an effective background radiance of 638 $\mu W/cm^2$-sr in the 0.35 μm-0.40 μm wavelength interval can be provided at the display window. This is considered a *minimum* requirement. A typical sunlit cloud can be simulated if modifications are made to the present projector subsystem to provide increases in the average simulated background radiance to above 900 $\mu W/cm^2$-ster which is a highly desirable requirement. There is evidence, most of which is (unfortunately) classified, that there is some UV radiation from jet plumes of potential targets. Providing this capability is considered an optional requirement and, therefore, it is assumed that the sky background is always dominant. Also, in tail-on engagements, the UV radiance of the aircraft tailpipe will contribute to the signal at the seeker, especially at short range where atmospheric attenuation of UV radiation is less significant. The radiation emitted from the tailpipe is primarily visible, depending on engine configurations and operating conditions, but may approximate a 1500° K blackbody in a few instances.

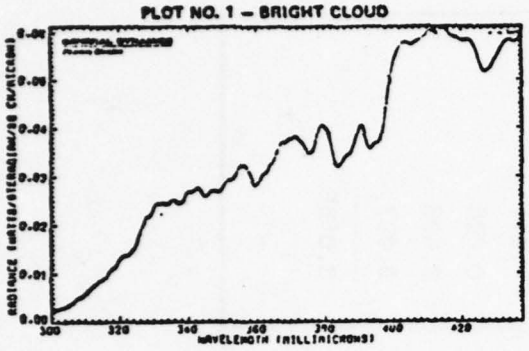

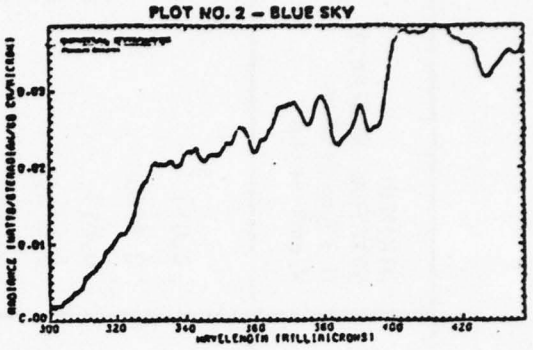

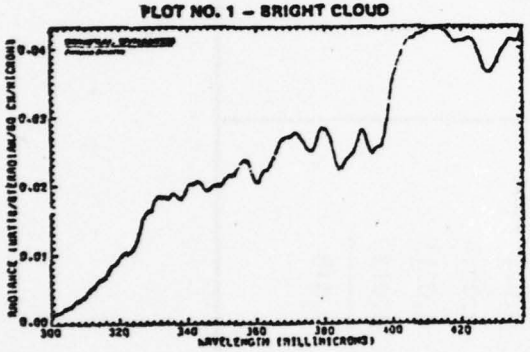

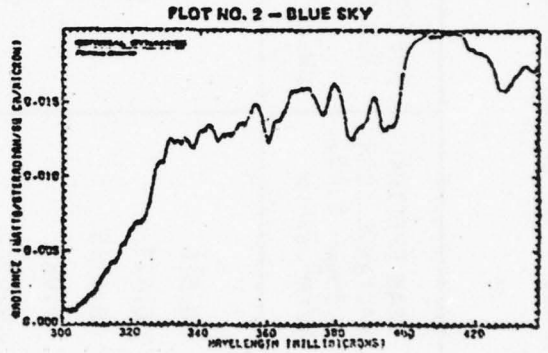

FIGURE 4-1. REPRESENTATIVE SPECTRAL RADIANCE CURVES OF BACKGROUND SCENES

TABLE 4-1. TABULATION OF SKY BACKGROUND RADIANCE DATA

PEAK SPECTRAL RADIANCE FROM 0.35μm- 0.40μm W/cm^2-sr-μm	AVERAGE RADIANCE FROM 0.35μm-0.40μm $\mu W.cm^2sr$	MINIMUM SPECTRAL RADIANCE 0.35μm-0.40μm W/cm^2-sr-μm
0.016	600	0.011
0.023	1000	0.0125
0.0215	925	0.013
0.021	650	0.0125
0.0325	1100	0.021
0.018	700	0.012
0.0155	600	0.0115
0.017	600	0.010
0.016	600	0.009
0.0115	475	0.008
0.0125	400	0.0065
0.017	550	0.009
0.019	600	0.0105
0.022	650	.011
0.0014	525	0.008
0.0115	500	0.008
0.012	400	0.007
0.018	638	0.0106

TABLE 4-2. TABULATION OF CLOUD BACKGROUND RADIANCE DATA

PEAK SPECTRAL RADIANCE FROM 0.35μm-0.40 m W/cm^2-sr-μ	AVERAGE RADIANCE FROM 0.35μ - 0.40μ $\mu W/cm^2$-sr	MINIMUM SPECTRAL RADIANCE FROM 0.35μ - 0.40μ W/cm^2-sr-μ
0.026	900	0.015
0.027	950	0.015
0.037	1350	0.021
0.043	1500	0.023
0.029	1050	0.017
0.051	1700	0.026
0.033	1200	0.020
0.014	450	0.0075
0.016	500	0.011
0.020	600	0.010
0.0115	500	0.0085
0.011	425	0.0075
0.017	650	0.01
0.0258	906	0.0147

The tailpipe signature simulation, as well as flare countermeasures are taken as *optional* requirements. A brief discussion of their possible implementation is contained in Appendix D.

4.3 VARIABLE CONTRAST

In addition to providing accurate absolute radiometric simulations of the target fuselage and surrounding background, a highly desirable requirement exists to control the relative radiance values between the target and background during a simulated engagement. Target radiance must be variable from near-zero to background levels in order to simulate one hundred percent and zero percent contrasts, respectively. Means of dynamically varying target radiance are required to simulate range closure. Changing the contrast ratio in real-time provides simulation of contrast change with range as actually occurs with an ultraviolet seeker. If there is no provision for variable contrast, then effects of atmospheric attenuation upon seeker performance at low signal-to-noise conditions cannot be accurately simulated.

Aircraft targets can be detected in the ultraviolet because they block UV radiation from the sky and thus appear darker than their surroundings. This phenomenon is termed negative contrast. Influencing factors that determine target irradiance H_T and hence target contrast are illustrated in Figure 4-2 . The UV background can be characterized by

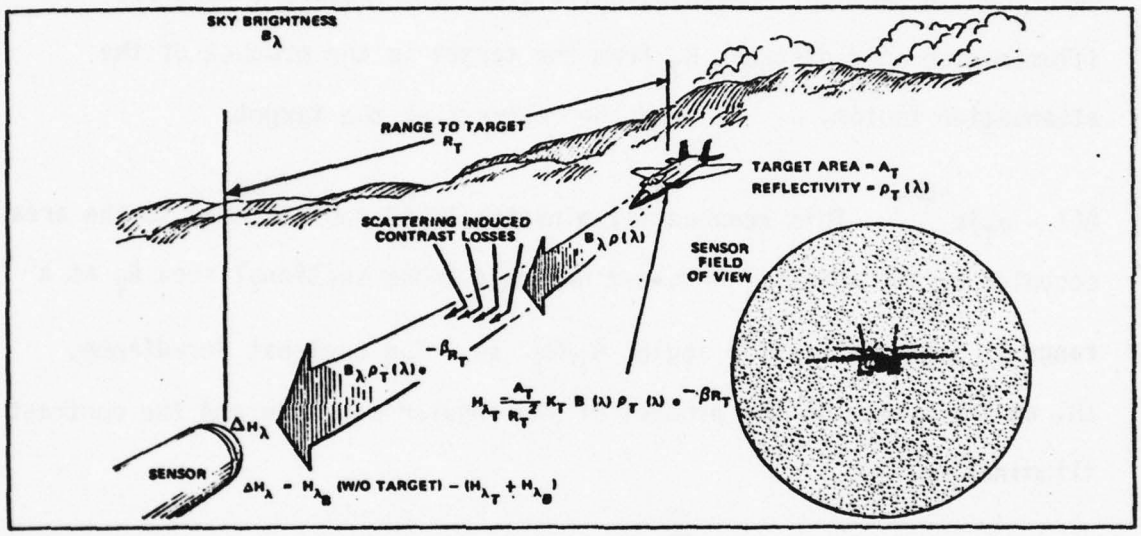

FIGURE 4-2. PARAMETER AFFECTING NEGATIVE CONTRAST DETECTION

its radiance B due to reflected and scattered sunlight. If the reflectivity of the target surface is ρ_T then the illumination produced by the target is $B\rho_T$. As the target range, R_T, increases, the atmosphere produces additional scattering, decreasing the contrast exponentially with range. The rate of decay in contrast with range is defined by a scattering coefficient β, which is a function of atmospheric conditions and can be described in terms of meterological visibility. Apparent contrast illumination at a distance R_T from the target is the product of the attenuation factor, $e^{-\beta R_T}$, and the contrast at the target

$B(1 - \rho_T)e^{-\beta R_T}$. This reduced illumination level applies only to the area occupied by the target. A target having a cross sectional area A_T at a range R_T subtends a solid angle A_T/R_T^2 sr. The contrast irradiance, ΔH, at the seeker is the product of the angular coverage and the contrast illumination, is

$$\Delta H = \frac{A_T}{R_{T2}} \quad (1-\rho_T)e^{-BR_T} \tag{4-1}$$

4.4 FUSELAGE TARGET SIZE

Target size and shape is generated through motion of the target projector vane mechanism. Fuselage targets are generated by controlling the vanes to produce rectangles of varying aspects in order to completely evaluate sensor performance from acquisition to intercept. Capability to generate target sizes smaller than sensor resolution capabilities should

be available. Capability to simulate a $1m^2$ square target at a range of 5 Km (0.2 mrad) should be adequate for evaluation of present state-of-the art UV seeker systems. Table 4-3 presents a requirement summary for both the background and fuselage projectors.

4.5 PROJECTOR SIZE

In addition to the requirements in the previous paragraphs, which can be considered system requirements, there are other constraints placed upon any new projector design relating to size, weight, maintainability, and reliability. No firm requirements were established in these areas, and only general rules are presented here.

New projector designs or modifications to present projectors should be limited so that the design that results is compatible with the existing IRSS single axis projector table and can be readily interfaced to the exterior display optics system. Electrical, cooling or gas tubing, and support cables (if needed) should not interfere with the projector table rotation. Also, new designs should require minimum maintenance, and not necessitate use of highly trained technical personnel in operation of the proposed system.

TABLE 4-3. SIMULATION REQUIREMENT SUMMARY FOR UV/VIS FUSELAGE AND BACKGROUND PROJECTOR

ITEM	PARAMETER	ORDER OF REQUIREMENT		
		MINIMUM	DESIRABLE	OPTIONAL
SPECTRAL PASSBAND		0.35μm - 0.40μm	0.30μm - 0.40μm	0.30μm - 0.7μm
BLUE SKY BACKGROUND	RADIANCE	638μW/cm^2-sr	800μW/cm^2-sr	1 mW/cm^2-sr
CLOUD BACKGROUND	RADIANCE	800μW/cm^2-sr	900μW/cm^2-sr	1.4 mW/cm^2-sr
FUSELAGE TARGET	SIZE	3m x 20m	1m x 20m	1m x 20m
	RANGE	3 Km	5 Km	9 Km
	ANGULAR SUBTENSE	1 mrad - 6 mrad	0.2 mrad - 6.0 mrad	0.1 mrad - 6 mrad
	CONTRAST	100% BACKGROUND RADIANCE	5% - 100% BACKGROUND RADIANCE	0% - 100% BACKGROUND RADIANCE

5. TEST AND EVALUATION

5.1 TEST RATIONALE

In order to carry out a thorough performance evaluation and radiometric analysis on the UV projection subsystem, a series of tests were conducted to determine present capabilities of the system and to complement available data on projector components. Presented in this section are test results relating to the present performance capabilities of the UV/VIS projector subsystem. These results are used to support the development of the analytical radiometric model to be described in Section 6. This model was developed to determine a total system radiometric transfer function (throughput) by measuring the lamp radiance and the radiance at the display mirror and, where possible, to evaluate the performance characteristics of individual system components. The effective (apparent) target and background radiances were measured at the display window of the exterior optics. By making effective radiance measurements at the projection lens and of the target and background sources, radiance transfer characteristics of the entire UV/VIS projector and the IRSS exterior optics display system could be determined.

During the course of the radiometric tests, it was determined that the radiance transfer characteristics of the projection system were not adequate to meet preliminary design requirements. A possible cause of the low projector output was suspected to be a low radiance from the xenon source lamps. To verify this, the lamps were removed from the projector

table and their radiances measured directly to determine if they were within manufacturers specifications. Results of all these tests are discussed in detail in the following paragraphs.

5.2 RADIOMETER OPERATION

Tests were performed in both the ultraviolet and visible wavebands with a Barnes Engineering, Spectral Master Research Radiometer model 12-550. This radiometer employs a Cassegrain optical system with a silicon UV/VIS detector package and quartz relay lens. The radiometer was used to determine effective radiance values of simulated fuselage targets and sky backgrounds by measuring the effective radiance in a plane past the display mirror. Where possible, the radiometric transfer of system elements were determined through measurement differences at the display mirror.

The radiometer detector-filter combination was functional only in the wavelength interval 0.28μm - 0.37μm and not in the primary wavelength interval of interest 0.35μm - 0.40μm. All absolute radiometric qualtities pertaining to the 0.35μm - 0.40μm interval were extrapolated from the measured data in the 0.28μm - 0.37μm waveband. It must be noted that the measurements as quoted in subsequent paragraphs are the *apparent radiances*, related to the actual radiance by the source weighting factor as derived in Appendix A.

When a target or source fills the radiometer field of view (18 mrad) the equation which relates the effective radiance, N_s, to the radiometer output voltage, V_0, is given by:

$$N_S = \frac{AV_0}{K_S} \tag{5-1}$$

Where A is the product of the electrical attenuation and filter factors, K_S is the system response factor provided by the manufacturer and is given in Reference [5-1].

The fractional portion of the field filled by the source must be calculated to determine the radiance when the source does not fill the radiometer field-of-view. That fractional portion, X, is given by the ratio of the area of the source target A_S, to the area covered by the radiometer field-of-view, A_R, or

$$X = \frac{A_S}{A_R} \tag{5-2}$$

The effective measured source radiance becomes

$$N_S = \frac{AV_0}{XK_S} \tag{5-3}$$

The radiant intensity of the source, J_S, is then the radiance of the source N_S multiplied by the area of the source A_S

$$J_S = N_S A_S \tag{5-4}$$

Since the radiometer was not sensitive in the primary waveband of interest, 0.35μm - 0.40μm, it was necessary to extrapolate from measurements taken in the 0.28μm - 0.37μm waveband by estimating the relative output of the xenon source in those wavebands. These extrapolations can be made only if it is assumed that all optical elements in the UV/VIS projections and exterior optics display system have the same absorption, transmission, and reflection characteristics in the two wavebands. Table 5-1 lists percentage output with wavelength of a xenon spectrum for a lamp with a silver reflector. As given by this table, the percentage output of the xenon lamp between 0.28μm and 0.37μm is 2.55% of the total output. There is 3.26% of the total lamp output between 0.35μm and 0.40μm. Hence, with the previous assumption, to extrapolate to the 0.35μm - 0.40μm interval, a factor of 3.26/2.55 or 1.28 is introduced.

5.3 EFFECTIVE BACKGROUND AND TARGET RADIANCE OF THE UV/VIS PROJECTOR

The first series of tests were performed to determine the effective radiance of the simulated background and target. That is, the effective radiance of the target vanes in the background projector and the surface of the diffusing plate in the target projector were measured. The radiance of these objects can be measured because they both act as secondary sources within the projection system since their surfaces have a diffusing characteristic.

TABLE 5-1. SPECTRAL DISTRIBUTION OF RADIATION FOR A XENON ARC LAMP WITH A SILVER REFLECTOR

WAVELENGTH (nm)	RADIATED POWER %	CUMULATIVE SUM %
280	0.10	0.45
290	0.09	0.54
300	0.08	0.62
310	0.05	0.69
320	0.10	0.73
330	0.25	0.90
340	0.47	1.27
350	0.55	1.80
360	0.60	2.38
370	0.63	3.00
380	0.66	3.65
390	0.71	4.33
400	0.73	5.06
410	0.76	5.79
420	0.75	6.56
430	0.75	7.30
440	0.76	8.07
450	0.85	8.87
460	1.02	9.77
470	0.99	10.86
480	0.91	11.78
490	0.89	12.69
500	0.83	13.52
510	0.84	14.36
520	0.84	15.20
530	0.84	16.04
540	0.83	16.87
550	0.83	17.70
560	0.82	18.53
570	0.82	19.35
580	0.82	20.17
590	0.81	20.99
600	0.80	21.80
610	0.83	22.61
620	0.82	23.44
630	0.80	24.25
640	0.79	25.03
650	0.78	25.83
660	0.78	26.60
670	0.79	27.38
680	0.86	28.21
690	0.76	29.04
700	0.72	29.75

5.3.1 Effective Background Radiance

The Barnes radiometer was mounted at the IRSS exterior optics display window. With the background lamp operating at its rated electrical input power of 500 W and the vane mechanism closed, the radiometer was aligned so its field-of-view covered one side of the target vane with no obscuration. The cloud wheel filter was in its maximum aperture position. The radiometer output voltage was recorded and the effective background radiance calculated as indicated in Section 5.2. Table 5-2 gives the results of the background radiance measurements.

5.3.2 Effective Fuselage Target Radiance

For this test, the radiometer was aligned on the center portion of the vane mechanism with the vanes at their minimum aperture. The target projector lamp was on but the background projector lamp was off. This ensured that the measurement would be taken at the center of the diffusing plate. The vanes were opened to their maximum aperture and the radiometer output voltage recorded. Both visible and ultraviolet radiances were measured. Results of this test are given in Table 5-3.

5.4 MEASUREMENTS AT THE PROJECTOR LENS

It was anticipated that by measuring effective radiance values at the projector lens, with the radiometer looking back at the diffusion plate of the fuselage target projector, the radiance transfer of the entire exterior optics display system could be determined separately.

TABLE 5-2. RESULTS OF EFFECTIVE BACKGROUND RADIANCE MEASUREMENTS

PARAMETER \ WAVELENGTH INTERVAL	0.28μ - 0.37μ	0.40μ - 0.70μ	0.35μ - 0.40μ*
LAMP INPUT POWER	500 W	500 W	500 W
RADIOMETER OUTPUT VOLTAGE (V_0)	6.8 V	8.4 V	-
RADIOMETER OPTICAL ATTENUATION FACTOR	1	24.17	-
RADIOMETER ELECTRICAL ATTENUATION	11.2	31.6	-
RADIOMETER TRANSFER COEFFICIENT (K_s)	7.16×10^7 V/Wcm^2-sr	3.82 x 10 V/Wcm^2-sr	-
EFFECTIVE RADIANCE $N_s = \frac{V_0 A}{K_s}$	10.6 μW/cm^2-sr	168 μW/cm^2-sr	13.6 μW/cm^2-sr *

Constant Test Conditions:

Vanes at minimum aperture
Iris at maximum aperture

* Denotes extrapolated value

TABLE 5-3. RESULTS OF EFFECTIVE FUSELAGE TARGET RADIANCE MEASUREMENTS

PARAMETER \ WAVELENGTH INTERVAL	0.28μ - 0.37μ	0.40μ - 0.70μ	0.35μ - 0.40μ*
LAMP INPUT POWER	300 W	300 W	-
RADIOMETER OUTPUT VOLTAGE V	8.5 V	8.6 V	-
RADIOMETER OPTICAL ATTENUATION	1	24.17	-
RADIOMETER ELECTRICAL ATTENUATION	15.8	22.3	-
RADIOMETER TRANSFER COEFFICIENT (K_s)	7.16×10^6 V/W/cm^2-sr	3.82×10^7 V/W/cm^2-sr	-
EFFECTIVE RADIANCE (N_s) $N_s = \frac{AV_0}{K_s}$	18.8 μW/cm^2-sr	121 μW/cm^2-sr	155 μW/cm^2-sr*

Constant Test Conditions:

Vanes at maximum aperture
IRIS at maximum aperture
* Denotes extrapolated value

Due to physical mounting problems in the laboratory and the Cassegrain configuration of the radiometer, the field-of-view of the radiometer could not entirely be filled with the diffusing plate. Therefore, there could be no accurate measurement made at the projector lens. Instead, the radiance transfer of the display optics was based on the product of the calculated values for the mirror reflectance for the nine mirrors, and a *pupil expansion factor*, defined as

$$P.E. = \frac{d^2}{(11.64)^2} \tag{5-5}$$

where d is the diameter in inches of the source in the projector lens. Since d has a maximum value of one inch (the physical mounting stop), and was measured (in Section 5.3.3) as one inch, the pupil expansion factor was:

$$P.E. = 0.00738 \tag{5-6}$$

The mirror reflectance will be analyzed in Appendix C of this report.

5.5 COMPONENT TRANSMITTANCES

The ability to determine the transmittance of each component, by comparison of measurements of total system transmittance before and after its removal, is naturally limited to those components that have no optical power, that is, those elements that do not shape the radiation beam, nor have any imaging characteristics. In addition, those elements

that merely move the beam (i.e., mirrors) were not amenable to measurement. Following are the results of tests on those few elements for which the above restrictions do not apply.

5.5.1 Cloud Wheel Transmittance

The cloud wheel is a circular plate of fused quartz that provides spatial variations of intensity to simulate clouds during a sensor test. Transparent portions of the wheel pass through the optical beam as the wheel continually rotates. The edges of the transparent portions of the wheel are imaged upon the vane mechanism by the relay lens. The transmittance of this element could be measured since it has no optical power. The effective background radiance was measured at the display window both with and without the cloud wheel filter. Only the ratio of the radiomenter outputs was needed for this test and not the absolute radiances. Results of this experiement are outlined in Table 5-4. These results indicate that a small gain in system radiance transfer could be realized if a different type of cloud wheel filter was incorporated into the system. Alternatives will be discussed in Section 8. of this report.

5.5.2 Beam Splitter Transmittance

The next series of tests were to determine the transmittance and reflectance characteristic of the beam splitter in the UV/VIS background - fuselage projector. The beam splitter redirects the diverging cone of radiation from the relay lens onto the vane assembly. Radiation from the background source passes through the beam splitter twice, while the radiation from the target projector passes through the beam

TABLE 5-4. CLOUD WHEEL TRANSMITTANCE MEASUREMENTS

PARAMETER	WAVELENGTH INTERVAL			
	0.28μm- 0.37μm		0.40μm- 0.70μm	
Cloud Wheel Position	IN	OUT	IN	OUT
Radiometer Output (volts)	8.0	7.0	8.3	9.5
Radiometer Filter Factor	1	1	1	24.17
Radiometer Electrical Attenuation Factor	7.94	11.2	707.9	31.6
% Increase in Radiance Transfer As a Result of Removing Cloud Wheel	23%		23%	

Constant Conditions During Test:

Lamp Input Power	480 W
Vanes	Closed
Iris	Open

splitter only once. The radiometer was again positioned at the display mirror looking back into the display optics at the diffusing plate of the target projector. The target lamp was operated at 300 W input electrical power with both the iris and target vanes opened to their maximum apertures. Results of these tests are presented in Table 5-5.and indicate that the beam splitter has a transmittance ratio of approximately 42% for unpolarized light. Since dielectric beam splitters are about 95% effective, the reflectance is about 55%.

TABLE 5-5. RESULTS OF BEAMSPLITTER TRANSMITTANCE AND REFLECTANCE MEASUREMENTS

PARAMETER \ WAVELENGTH INTERVAL	0.28μm- 0.37μm		0.4μm- 0.7μm	
Beamsplitter position	IN	OUT	IN	OUT
Radiometer Output Voltage	7.9V	6.6V	7.0V	8.6V
Radiometer Filter Factor	1	1	24.17	24.17
Radiometer Electrical Attenuation Factor	15.8	44.6	22.3	44.6
Resultant Beam Splitter Transmittance	42%		41%	

5.5.3 Iris Transmission Factor

The next sequence of tests were designed to determine the effect of the iris on the system radiance transfer. The iris is located adjacent to the UV/VIS background - fuselage projection lens assembly

and is used to control the simulated target radiance after the vane mechanism has reached its minimum mechanical limits. It was not known, however, if the iris also affected the background radiance transfer.

Iris diameter is adjusted by controlling the voltage across a feedback potentiometer in the iris motor feedback loop. The iris diameter, y, is determined by the equation $y = 4.1\left(\frac{mm}{V}\right) x + 3.5$ (mm) when x is the control voltage. Minimum and maximum iris diameters are 3.5 mm and 49.5 mm respectively. Table 5-6 gives the relationship between iris control voltage and iris open diameter. Ideally, the iris should be positioned so that the effective radiance as measured at the display window varies directly with the open area of the iris. In order to realize this relationship, the

TABLE 5-6. IRIS CONTROL DATA

CONTROL VOLTAGE	OPEN DIAMETER (mm)	OPEN AREA (cm^2)	% TOTAL AREA
0	3.5	0.10	0.5
1	8.6	0.58	3.0
2	13.7	1.47	7.6
3	18.8	2.78	14.4
4	23.9	4.49	23.3
5	29.0	6.61	34.3
6	34.1	9.13	47.4
7	39.2	12.07	62.7
8	44.3	15.41	80.1
9	49.5	19.24	100

iris position must coincide with the location of the image of the source, that is, inside the projection lens. Clearly,this is an impossibility. An alternate solution is to place the iris as close as possible to the projection lens and measure the iris transmission factor as a function of aperture diameter. With this method, the measured effective radiance at the display window will not follow an ideal relationship; however, a calibration factor can be determined so the effective radiance can be controlled.

In the present UV/VIS background-fuselage projector, the iris is considerably larger than the clear aperture of the projection lens, 49.5 mm for the iris as compared to 25.4 mm for the lens. It is obvious that an iris opening of anything greater than 25.4 mm has no effect upon the radiance transfer characteristics of the projection system. It will be considered that an iris opening of 25.4 mm will correspond to a maximum effective aperture.

The radiometer was mounted at the display window of the exterior optics and looked back at the vane assembly. For the first test the target lamp was on and the background lamp off. The vanes were closed to their minimum open aperture and the radiometer was aligned on the center of the illuminated aperture. The iris was opened in steps and the radiometer output was recorded. Results of this test are presented in Table 5-7 and Figure 5-1. Only the relative radiometer output voltages were needed for this test and not the absolute effective radiance values.

TABLE 5-7. EFFECT OF IRIS UPON UV/VIS TARGET PROJECTOR WITH VANE AT MINIMUM APERTURE

IRIS CONTROL VOLTAGE	IRIS DIA. (mm)	IRIS AREA (cm^2)	% OF MAXIMUM EFFECTIVE AREA	RADIOMETER OUTPUT VOLTAGE	RADIOMETER ELECTRICAL ATTENUATION	% OF MAX OUTPUT	IDEAL % OUTPUT
0	3.5	0.10	1.9	0.38	1	15.2	1.9
1	8.6	0.58	11.5	0.90	1	36.0	11.5
2	13.7	1.47	29.1	1.43	1	57.2	29.1
3	18.8	2.78	54.9	1.98	1	79.2	54.9
4	23.9	4.49	88.7	2.5	1	100	88.7

CONSTANT TEST PARAMETERS:

Target lamp on; background lamp off

Vanes at minimum aperture

0.28μm - 0.37μm wavelength interval

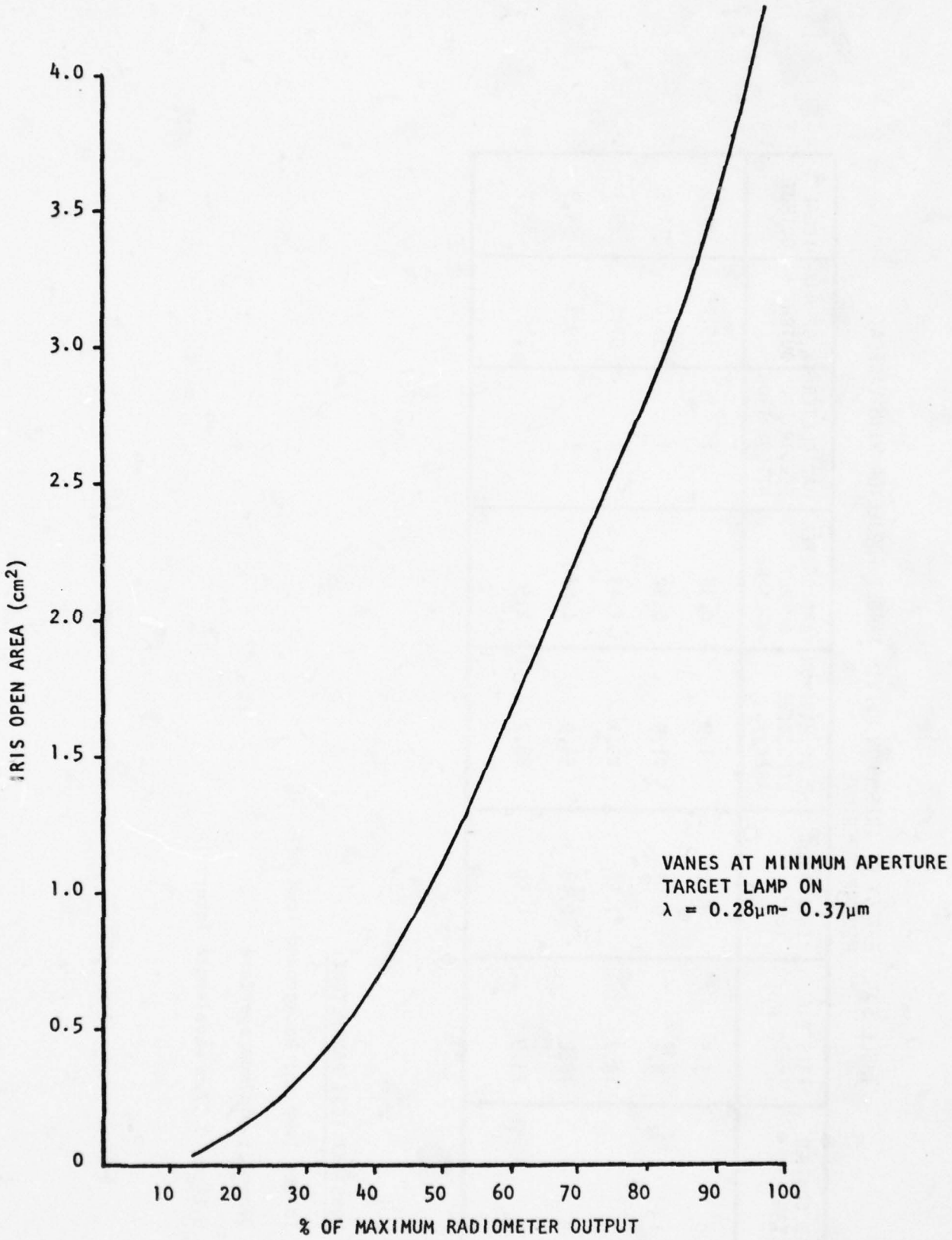

FIGURE 5-1. FUSELAGE TARGET PROJECTOR OUTPUT AS A FUNCTION OF IRIS OPENING

The second test in this series was essentially the same as that described above except that the vanes were opened to their maximum aperture. The iris was again opened incrementally and the radiometer output recorded. The results of this test are given in Table 5-8 and Figure 5-2.

The next test was to determine the effect of the iris upon the effective background radiance as measured from the display window. To determine this relationship, the target projector lamp was turned off and the background lamp on. The vane mechanism was closed to its minimum aperture, the iris opened, and the radiometer output voltage recorded. Results of this test are presented in Table 5-9 and Figure 5-3.

5.5.4 Projector Source

As the series of tests on the IRSS system continued, it became obvious that the radiometric output of the system did not meet earlier program requirements. Preliminary analysis of available data indicated that there was no single optical element that was responsible for a large percentage of the losses in the system. With the exception of the vane mechanism (Appendix B), manufacturers data (when available) and test results showed all components functioning within normal limits.

A possible cause of low output from the UV/VIS projection system was that the projector lamp radiance was not meeting minimum output requirements. As mentioned in Section 3, the source for the UV/VIS background projector is a Varian VIX-500 W xenon illuminator. In order to

TABLE 5-8. EFFECT OF IRIS UPON UV/VIS TARGET PROJECTOR WITH VANES AT MAXIMUM APERTURE

IRIS CONTROL VOLTAGE	IRIS DIA (mm)	IRIS AREA (cm^2)	% OF MAXIMUM EFFECTIVE AREA	RADIOMETER OUTPUT VOLTAGE	RATIOMETER ELECTRICAL ATTENUATION	% OF MAXIMUM OUTPUT	IDEAL % OUTPUT
0	3.5	0.10	1.9	4.5	1.41	11.5	1.9
1	8.6	9.58	11.5	0.8	15.8	22.9	11.5
2	13.7	1.47	29.1	1.8	15.8	51.4	29.1
3	18.8	2.78	54.9	2.8	15.8	80.0	54.9
4	23.9	4.49	88.7	3.5	15.8	100	88.7

CONSTANT TEST PARAMETERS:

Target lamp on; background lamp off

Vanes at maximum aperture

0.28μm- 0.37μm wavelength interval

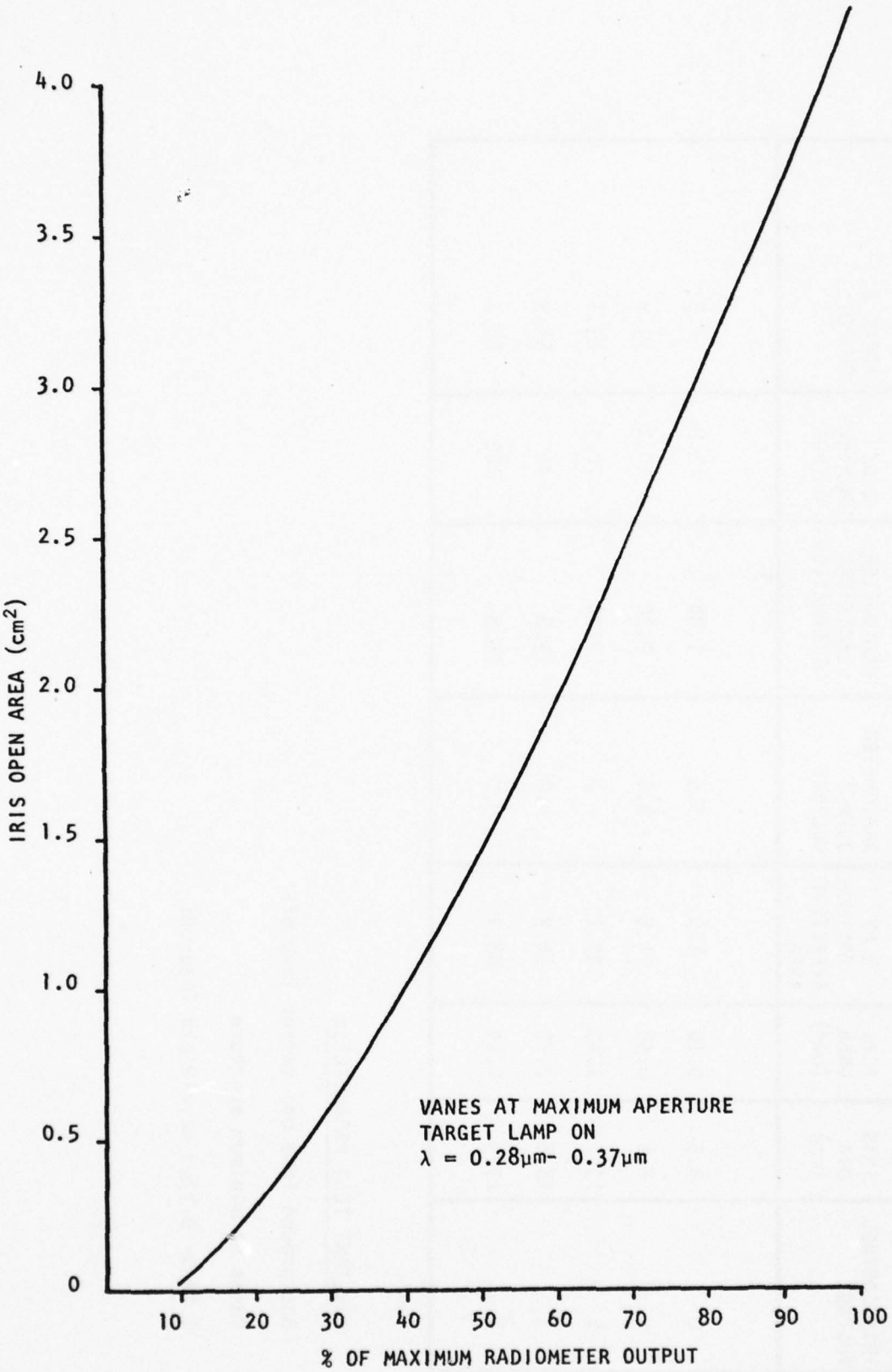

FIGURE 5-2. PROJECTOR OUTPUT AS A FUNCTION OF IRIS OPENING

TABLE 5-9. EFFECT OF IRIS UPON UV/VISIBLE BACKGROUND PROJECTOR WITH VANES AT MINIMUM APERTURE

IRIS CONTROL VOLTAGE	IRIS DIA (mm)	IRIS AREA (cm^2)	% OF MAXIMUM EFFECTIVE AREA	RADIOMETER OUTPUT VOLTAGE	RADIOMETER ELECTRICAL ATTENUATION	% OF MAXIMUM OUTPUT	IDEAL % OUTPUT
0	3.5	0.10	1.9	5.5	1.98	13.8	1.9
1	8.6	0.58	11.5	4.0	7.94	40.2	11.5
2	13.7	1.47	29.1	7	7.94	70.3	29.1
3	18.8	2.78	54.9	4.8	15.8	96	54.9
4	23.9	4.49	88.7	5.0	15.8	100	88.7

CONSTANT TEST PARAMETERS:

Background lamp on; target lamp off

Vanes at minimum aperture

0.28μm- 0.37μm wavelength interval

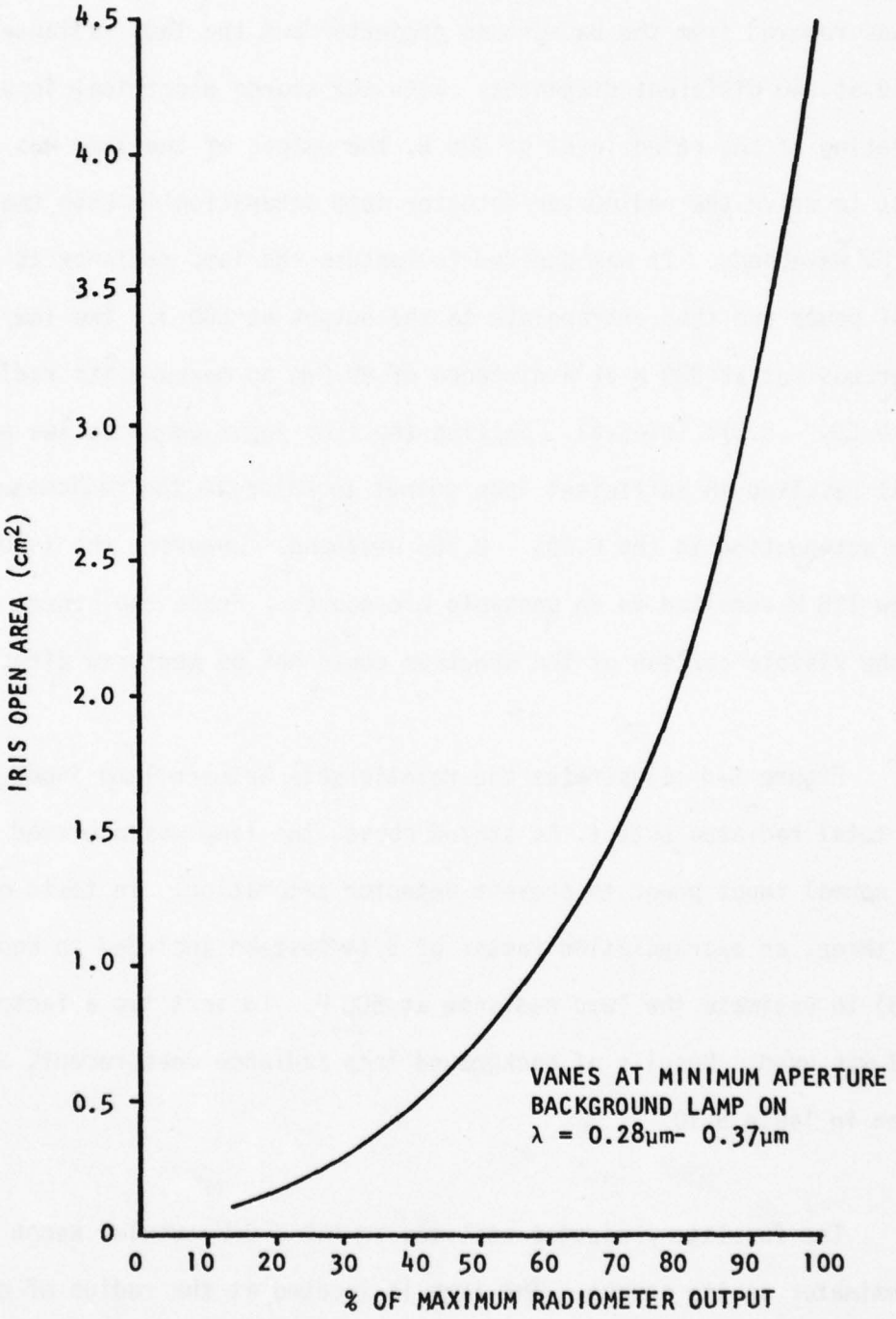

FIGURE 5-3. PROJECTOR OUTPUT AS A FUNCTION OF IRIS OPENING

determine if the lamp output was meeting manufacturers specifications, it was removed from the background projector and the lamp radiance measured at two different distances. With the source electrical input power operating at the rated level of 500 W, the output of the lamp was sufficient to drive the radiometer detector into saturation in both the visible and UV wavebands. It was decided to measure the lamp radiance at a lower input power and then extrapolate to the output at 500 W. The lamp input power was set at 330 W at a distance of 86.9 m to measure its radiance in the 0.28μ - 0.37μ interval. Setting the lamp input power as low as 198 W still resulted in sufficient lamp output to saturate the radiometer at maximum attenuation in the 0.40μ - 0.70μ waveband. Lowering the input power below 198 W resulted in an unstable arc source. Hence the source output in the visible portion of the spectrum could not be measured directly.

Figure 5-4 illustrates the relationship between lamp input power and total radiated output. As stated above, the lamp was operated below its normal input power to prevent detector saturation. In tests one and three, an extrapolation factor of 3.14 must be included in Equation (5-3) to estimate the lamp radiance at 500 W. In test two a factor of 1.33 was used. Results of background lamp radiance measurements are given in Table 5-10.

The fuselage projector utilizes an ILC 300 W tubular xenon illuminator as its source. The lamp is located at the radius of curvature of an aluminized spherical reflector that serves to increase the

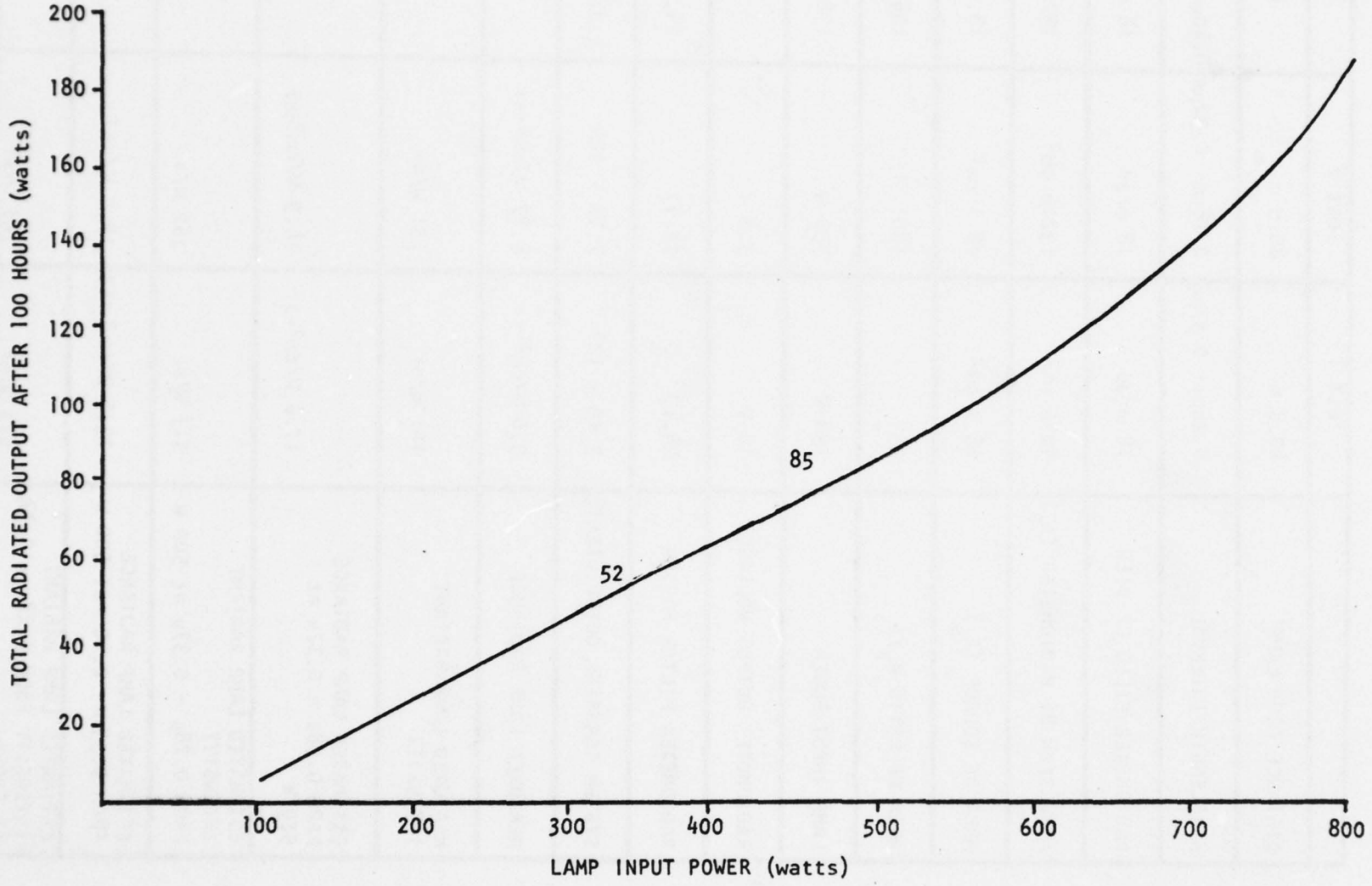

FIGURE 5-4. RADIATED OUTPUT VS ELECTRICAL INPUT FOR XENON ARC LAMP

TABLE 5-10. RESULTS OF BACKGROUND SOURCE MEASUREMENTS

	Test 1	Test 2	Test 3
DISTANCE FROM LAMP	40.8 m	86.9 m	86.9 m
WAVELENGTH INTERVAL	0.28μm- 0.37μm	0.28μm- 0.37μm	0.40μm-0.70μm
RADIOMETER FIELD OF VIEW	18 mrad	18 mrad	18 mrad
AREA SEEN BY RADIOMETER (A_R)	4236 cm^2	19216 cm^2	19216 cm^2
AREA OF SOURCE (A_s)	18.1 cm^2	18.1 cm^2	18.1 cm^2
AREA OF RATIO A_R/A_s	234	1061	1061
LAMP INPUT POWER	198 W	330 W	198 W
RADIOMETER OUTPUT VOLTAGE	10 V	3.5 V	-
RADIOMETER FILTER FACTOR	24.17	24.17	24.17
SYSTEM TRANSFER COEFFICIENT	7.16×10^6	7.16×10^6	3.82×10^7
MEASURED LAMP RADIANCE	5.6 W/cm^2-sr	8.87 W/cm^2-sr	-
MEASURED LAMP RADIANT INTENSITY	101 W/sr	151 W/sr	-
ESTIMATED LAMP RADIANCE FROM 0.28μ - 0.37μ at 500 W	17.6 W/cm^2-sr	14.5 W/cm^2-sr	-
ESTIMATED LAMP RADIANT INTENSITY FROM 0.28μ - 0.37μ at 500 W	317 W/sr	262 W/sr	-
ESTIMATED LAMP RADIANCE FROM 0.35 μ- 0.40 μat 500 W	23.4 W/cm^2 -sr	19.3 W/cm^2-sr	-
ESTIMATED LAMP RADIANT INTENSITY FROM 0.28 μ- 0.37μ AT 500 W	217 W/sr	262 W/sr	-

radiance of the source. Due to the geometry and mounting of the lamp housing and reflector, it was not possible to remove the target lamp to make an actual radiance measurement. In addition, during the radiometric test the tubular lamp failed to ignite and was determined to be beyond its performance limit.

A rough measurement of the ratio of the UV radiance from 0.28μm - 0.37μm to the visible radiance from 0.40μm - 0.70μm was made, however. It was possible to turn the ILC lamp housing slightly so that the beam was directed away from the projector table and toward the radiometer. The radiometer was turned into the beam sufficiently to indicate a maximum output voltage reading in the visible portion of the spectrum. The output voltage due to the UV radiance in this position was also recorded. The results of this ratio measurement are presented in Table 5-11. There was no available data on the ILC tubular lamp.

Figure 5-5 shows the relationship between radiant intensity and radiant intensity variation with cone half angle for the Varian VIX-500 illuminator. From Figure 5-5a, a 100 hour lamp has a total radiant intensity on axis of approximately 12,500 W/sr. The radiant intensity from 0.28μm - 0.37μm is then approximately 319 W/sr and from 0.35μm - 0.40μm is 408/sr, based on percentage radiant output in those spectral intervals.

Table 5-12 compares the calculated and measured background lamp radiance and radiant intensity values.

TABLE 5-11. FUSELAGE TARGET LAMP RELATIVE RADIANCE VALUES

	Test 1		Test 2	
WAVELENGTH INTERVAL	0.20μm - 0.37μm	0.40μm - 0.70μm	0.28μm - 0.37μm	0.40μm-0.70μm
RADIOMETER OUTPUT VOLTAGE	3.7 V	10 V	3.9 V	9.5 V
RADIOMETER FILTER FACTOR	24.17	24.17	24.17	24.17
RADIOMETER ELECTRICAL ATTENUATION	707.9	707.9	707.9	707.9
SYSTEM RESPONSE FUNCTION	7.16×10^6	3.82×10^7	7.16×10^6	3.82×10^7
RATIO OF VIS/UV	14.2		13.1	

CHARACTERISTIC CURVES
Typical performance values

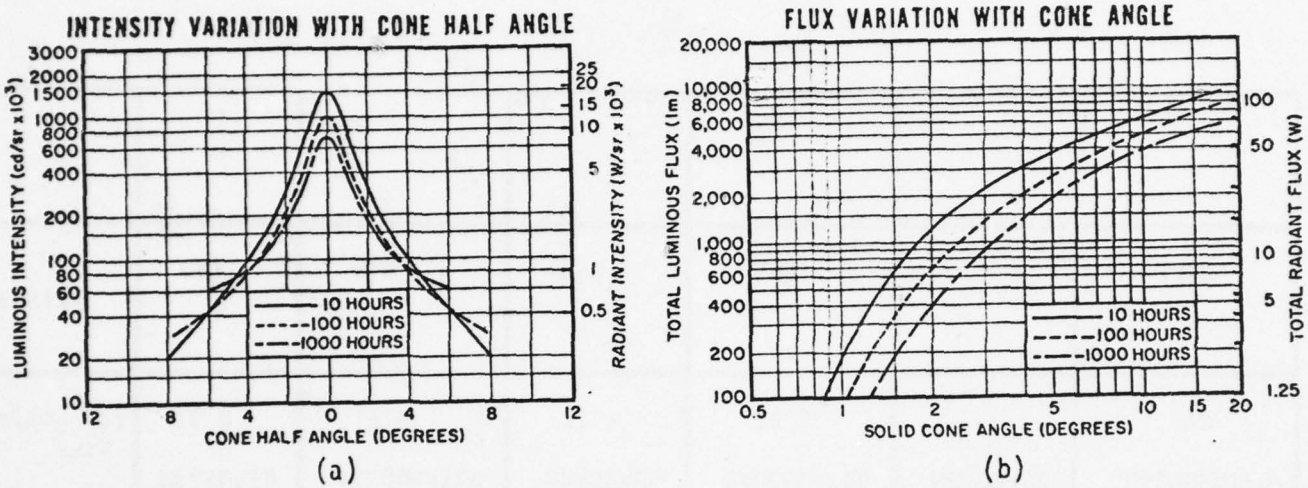

FIGURE 5-5. VARIAN VIX-500 PERFORMANCE VALUES

TABLE 5-12. COMPARISON OF CALCULATED AND MEASURED BACKGROUND LAMP RADIANCE

WAVELENGTH INTERVAL	0.28μm - 0.37μm		0.35μm - 0.40μm		0.40μm - 0.70μm	
	MEASURED	CALCULATED	MEASURED	CALCULATED	MEASURED	CALCULATED
RADIANCE (W/cm^2-sr)	16.0	17.6	21.4*	22.5	-	170
RADIANT INTENSITY (W/sr)	290	319	290*	408	-	3086

* Denotes Extrapolated Values

5.6 POLARIZATION TESTS

It is well known that reflection from metallic mirrors at angles far from normal incidence results in a partial polarization of the resultant beam. Successive reflections from mirrors in similar orientations may result in one polarization state being highly attenuated, and the other much less so. The large number of mirrors in both the projector and display optics opened the question of polarization effects accounting for the unexpectedly high radiance losses.

Polarization may be treated as a transfer problem, with each element modifying the state of polarization as received from the previous element. Of course, a complete determination of polarization state change requires a polarizer, a quarter wave plate, and the ability to make radiance measurements at the output of each component. Such a complete radiometeric analysis was not possible, not only from the mechanical constraints imposed by the projector system itself, but also by the radiometer configuration.

The only analysis tool available (other than the radiometer) was an inexpensive sheet polarizer. Insertion of this device into various locations in the projector optics, and rotating the polarizer while monitoring the radiometer output, enabled a rough analysis of polarization effects to be made. Also, visual observation of the final (display mirror) and intermediate images, as seen through the rotated polarizer, permitted additional qualitative judgements to be made.

Figure 5-6 shows the (relative) radiometer output as a function of polarizer position for the polarizer inserted between mirror m_1 and lens L_3 (see Section 6.) of the background projector. This same ratio held at all measurable locations in the background projector.

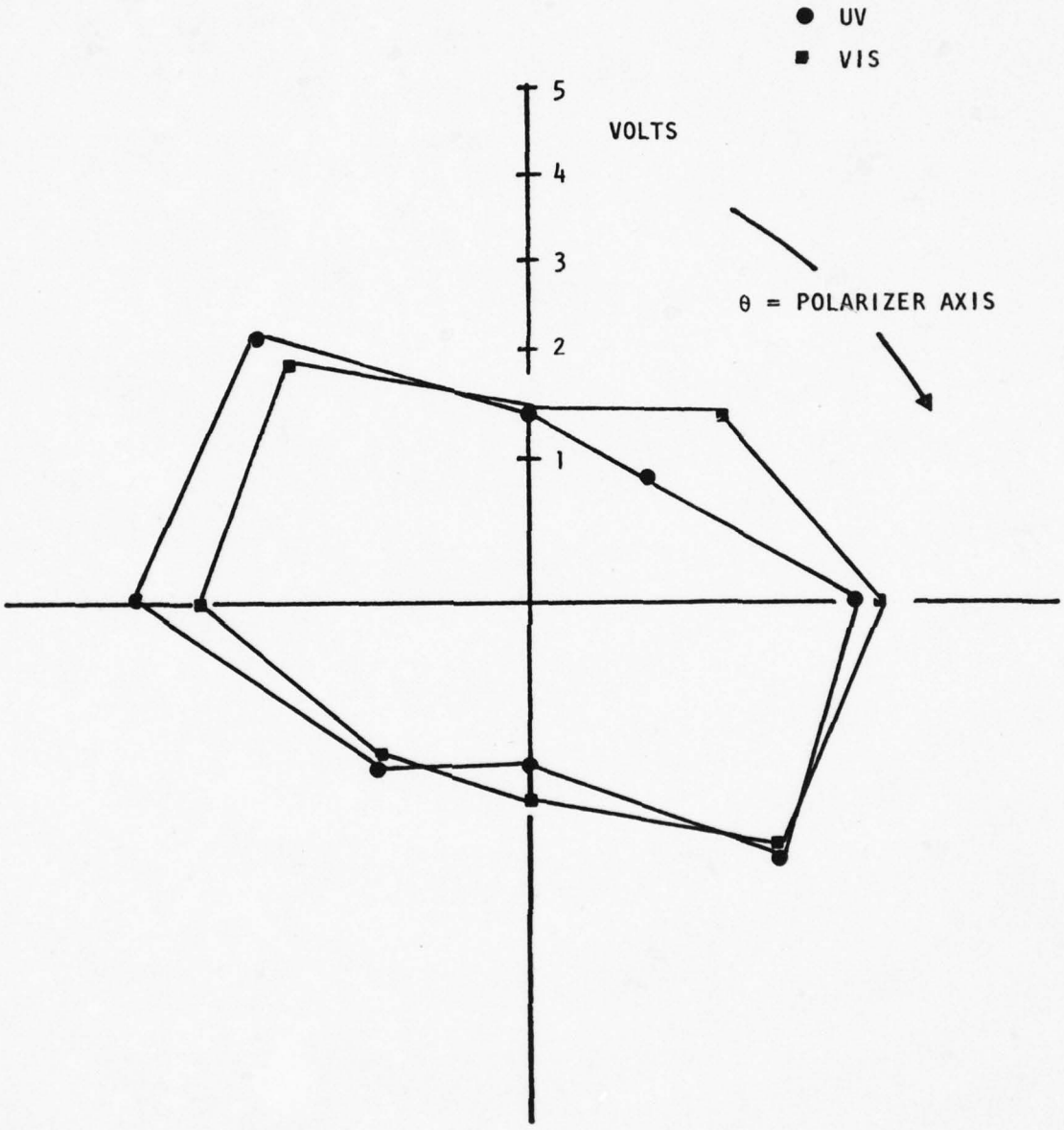

FIGURE 5-6. POLARIZATION AT FIRST MIRROR
(MEASUREMENT AT DISPLAY MIRROR)

6. ANALYSIS

6.1 GENERAL

In this section performance capabilities of the present UV/VIS projector are presented. By utilizing background information, results of the tests performed upon the projection system, analysis contained in the appendices of this report and available drawings from G.E., Reference [3-1], a model of the present projector system was developed. Analyses which support this model can conveniently be divided into two somewhat interdependent categories, (1) geometric and (2) radiometric. The geometric analysis deal with imaging properties of the system and how the final simulated scene is presented to the sensor under test. The radiometric analysis develops system radiance transfer parameters by assigning "opacity" values to individual system components. These values were primarily determined through the tests described in Section 5 of this report.

Section 6, Analysis, is further subdivided into a subsystem level in which the background projector, the fuselage target projector and the exterior optics display system are discussed. A simplified view of the optical configuration of the UV/VIS projection system and exterior optics is shown in Figure 6-1.

6.2 GEOMETRICAL OPTICS OF THE UV/VIS PROJECTOR SYSTEM

6.2.1 Background Projection Subsystem

Illustrated in Figure 6-2 is an optical schematic of the background projector assembly. The source of radiation for the projector is a model VIX-500, 500 W xenon illuminator, manufactured by the Varian Corporation,

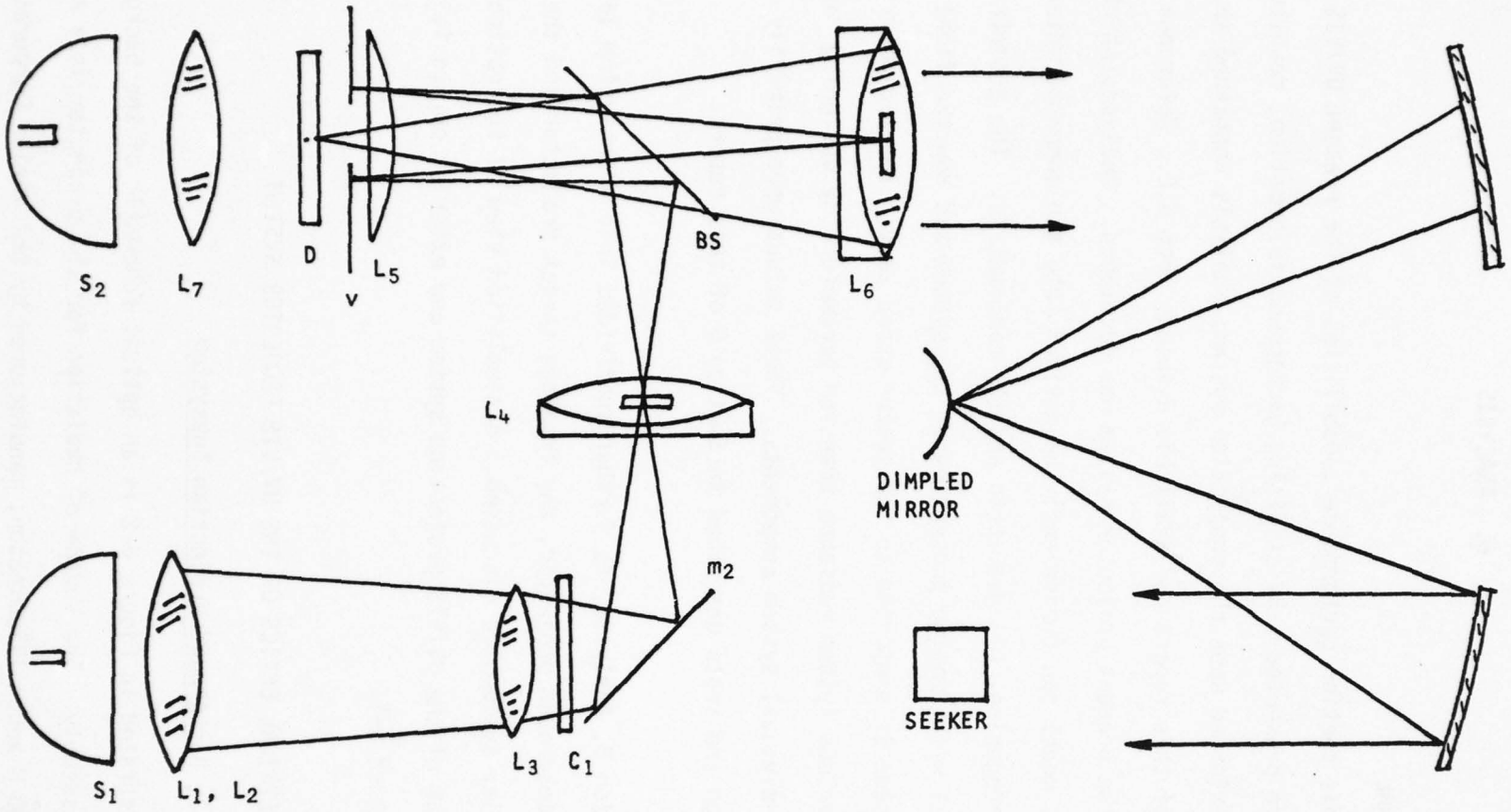

FIGURE 6-1. GENERAL OPTICAL SCHEMATIC OF UV/VIS PROJECTOR

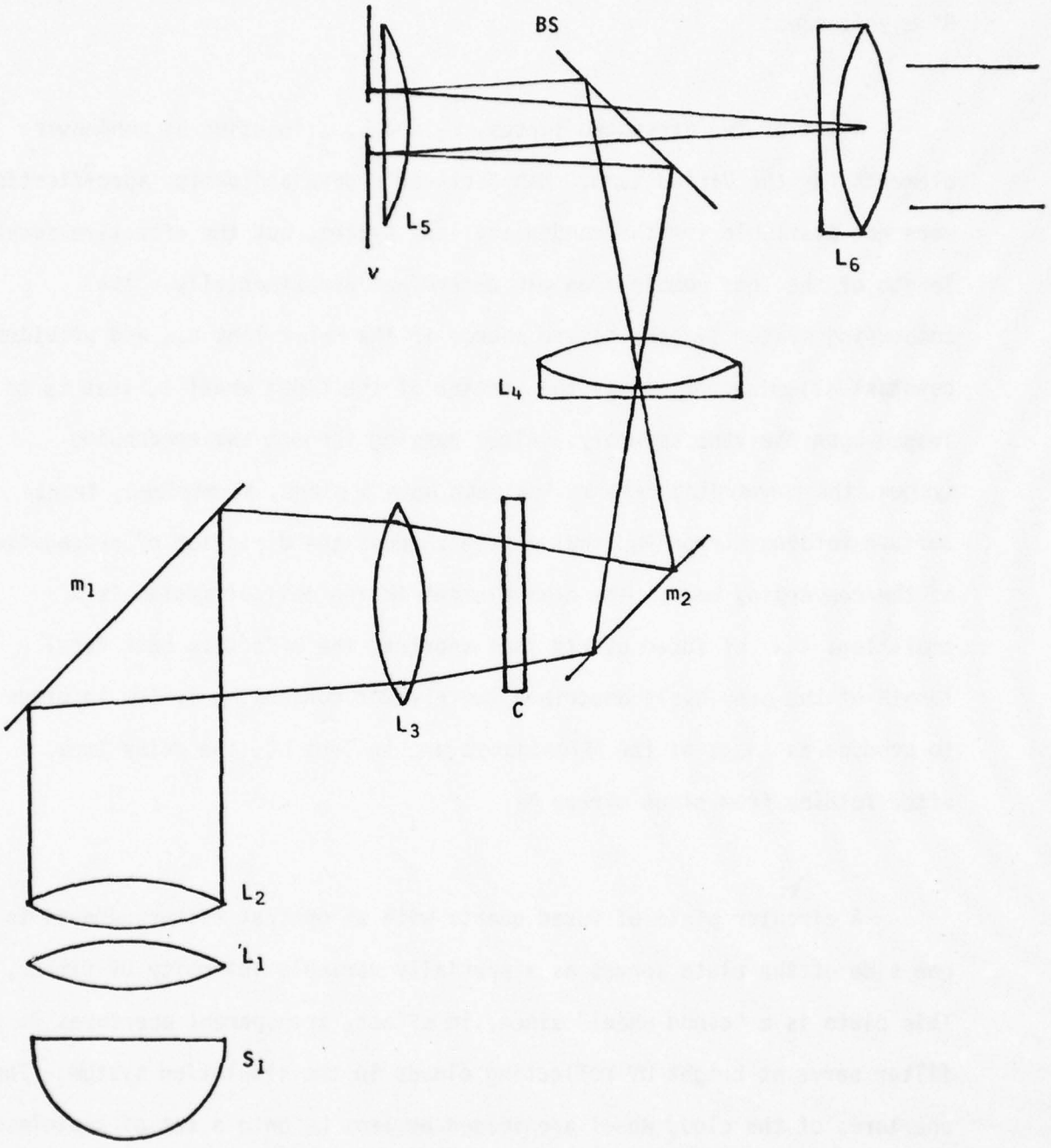

FIGURE 6-2. OPTICAL DIAGRAM OF THE VIS/UV BACKGROUND PROJECTOR ASSEMBLY

denoted S_1 in the figure. The arc output is quasi-collimated by a silver-coated parabolic reflector. The output beam is 48 mm in diameter with an 8° divergence.

A set of two airspaced lenses, L_1 and L_2 , function as condensor elements for the Varian lamp. Manufacturer's data and design specifications were not available for the condensing lens system, but the effective focal length of the lens combination was determined experimentally. The condensing system images the arc source in the relay lens L_4, and provides constant illumination across the portion of the cloud wheel C, that is to be imaged upon the vane assembly. After passing through the condensing system, the converging beam is incident upon a plane, aluminized, front-surface folding mirror (M_1) that merely changes the direction of propagation of the converging beam. The next element in the optical system is a small lens L_3, of fused quartz that shortens the effective back focal length of the previously described two element condensing system in order to produce an image of the illuminator arc in lens L_4, the relay lens, after folding from plane mirror M_2.

A circular plate of fused quartz with an optical filter adhered to one side of the plate serves as a spatially variable intensity UV filter, C. This plate is a "cloud wheel" since, in effect, transparent apertures in the filter serve as bright UV reflecting clouds in the simulation system. The apertures of the cloud wheel are imaged by lens L_4 onto a set of stainless steel vanes, v, that also function as the object for the fuselage projector. Thus, the relay lens functions as a subsidiary projection lens. The center of the relay lens is coincident with the effective back focal length of

lenses L_1, L_2, and L_3 which image the arc of the Varian lamp into the relay lens, thus providing even illumination across the vane mechanism. The cloud wheel is located at one conjugate point of the relay lens while the vane mechanism is located at the effective back focal length of the relay lens L_4 and the field lens L_5. Positioning of the relay lens provides a 3:1 magnification of the cloud wheel onto the vane mechanism.

The beam, now diverging, is incident upon an approximately 50-percent-transmitting 40-percent-reflecting beam splitter, (BS). The beamsplitter is placed at a 45 degree angle to the incident beam and 45 degrees with respect to the vane mechanism. The beam splitter was provided by Broomer Research Corporation, but no other performance specifications were available. It should be noted that the beam splitter and the subsequent two optical elements, the field lens and the main projection lens, are common elements to both the background and fuselage projectors. The centers of these elements are coincident with the optical axes of both projectors.

The diverging cone of radiation from the relay lens is incident upon a field lens L_5 that is positioned adjacent to the vane mechanism, v. The field lens is in a no power position with respect to the vane mechanism, that is, the image of the vane mechanism produced by the field lens is virtual and lies coincident with the object position.

Rays exiting the field lens onto the vanes are nearly parallel to the optical axis since the image of the source in the relay lens is at the focal length of the field lens. The radiation is now reflected off the

vanes back through the field lens and the beam splitter, and is focused into the center of the main UV/VIS projector lens, L_6. The diffusing characteristics of the vanes provide a mechanism by which the cloud wheel can be imaged onto the vane mechanism and function as the object for the main projection lens. Light passing through the aperture produced by the vanes is lost in the system, so the result is a background scene with a hole of variable size (i.e., the fuselage) in it. This hole is then filled by an image of the source whose brightness is less than that of the background scene, thereby producing the required fuselage/background contrast ratio of less than one. The field lens in its present position serves a dual purpose; first, to prevent vignetting as the seeker under test looks back into the exterior optics from the flight table and second, to re-image the arc source into the main projector lens. A complete discussion of the properties of the vanes is presented in Appendix B of this report.

The projection lens functions to provide an image at infinity of the vane mechanism and the cloud scene incident upon the vane assembly. The slightly diverging beam from the projection lens is incident upon a small front surface mirror that serves as an interface to the exterior optics display system. This system will be discussed in Section 6.2.3.

To better illustrate the function of the background projector, an analogy can be drawn between it and a refractive counterpart, the lantern slide projector. A lantern slide projector is drawn with the

background projector in Figure 6-3 for ease of comparison. Actually the background projector functions as two subprojector systems. First a projector to image the cloud wheel upon the vane mechanism and second a projector to image the target vanes at infinity for the exterior display optics.

Under normal operation a slide projector produces a real image of an illuminated object. An essential part of the projector is the condensing lens, a system of lenses placed in front of the slide. In order to provide uniform illumination of the projection screen and to minimize the size of the projection lens, projectors are designed so that the condenser system images the source at the projection lens. Under these conditions, the aperture stop of the optical system coincides with the mounting of the projection lens and full use is made of the dimensions of the lens. The condensing system is designed such that light from all points on the source illuminates every point on the slide.

When comparing the UV background projector to a lantern slide projector, the slide corresponds to the cloud wheel, the projection lens to the relay lens, and the screen can be compared to the target vanes. These comments correspond to the subsidiary projection system.

The second refractive analogy is somewhat more difficult and complex. In this projector subsystem the vanes correspond to the film or field stop to be projected, but the source for this projector subsystem

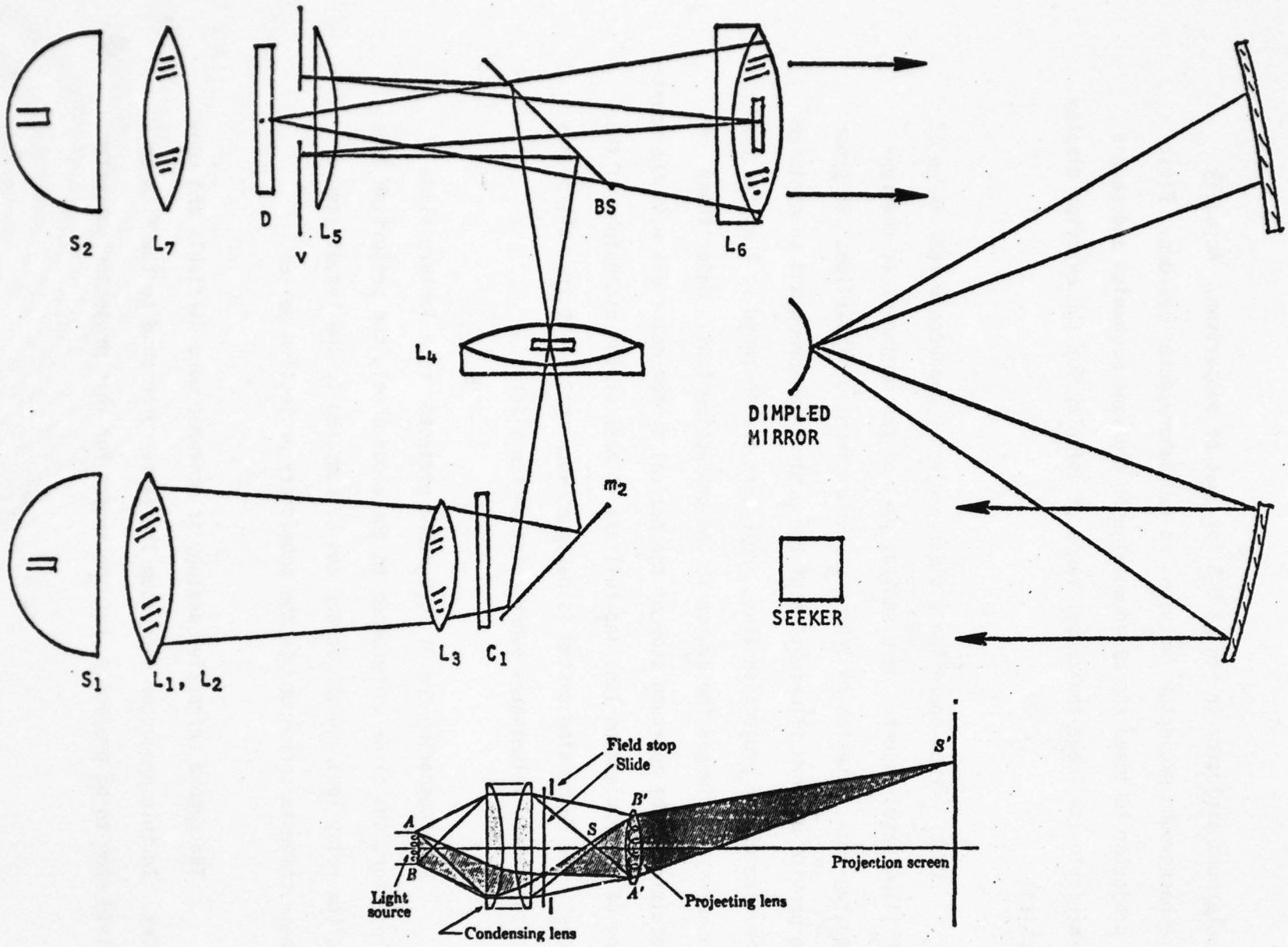

FIGURE 6-3. COMPARISON OF UV/VIS BACKGROUND PROJECTOR AND A LANTERN SLIDE PROJECTOR

is the image of the actual source in the relay lens. The problem is compounded by the fact that the radiation makes two passes through the field lens, once before and once after the reflection off the vanes. The refractive analogue of this projection subsystem is illustrated in Figure 6-4a. Using the thin lens equations, the effect of two field lenses can be combined so it can be assumed that only one lens is present as shown in Figure 6-4b. Then a direct analogy can be made with a standard lantern slide projector with the field lens as the condenser and the vane mechanism as the slide. Again, it should be noted that every point in the arc source contributes to the illumination of the vane mechanism.

6.2.2 UV/VIS Fuselage Projector

The UV/VIS fuselage (target) projection subsystem provides illumination for simulated fuselage targets. An ILC 300 W xenon tubular lamp serves as the present source for this projector. The lamp is located at the radius of curvature of an aluminized spherical reflector that acts to increase the effective lamp radiance. The fuselage target projector is illustrated in Figure 6-5.

Two air spaced lenses, L_7 and L_8, act as collimating elements to illuminate a diffusing plate located near the target vane assembly. The tubular lamp is located at approximately the effective front focal length of the two lenses. In effect, this optical system is operating in a "searchlight" configuration. Radiation exiting the collimating lenses is redirected via two front surface aluminized mirrors, M_3 and M_4, to a quartz diffusing plate.

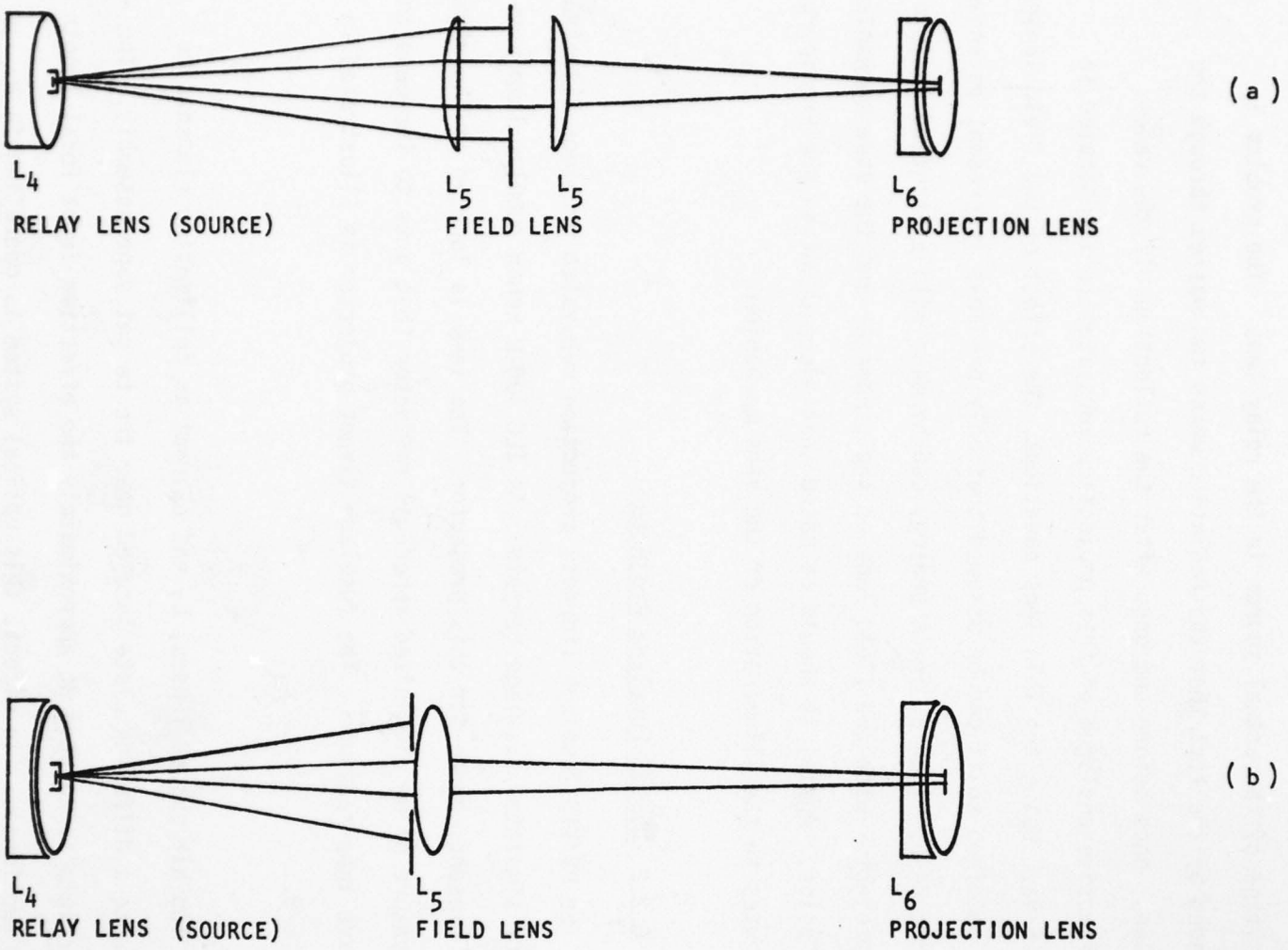

FIGURE 6-4. REFRACTIVE ANALOG OF BACKGROUND PROJECTION SUBSYSTEM

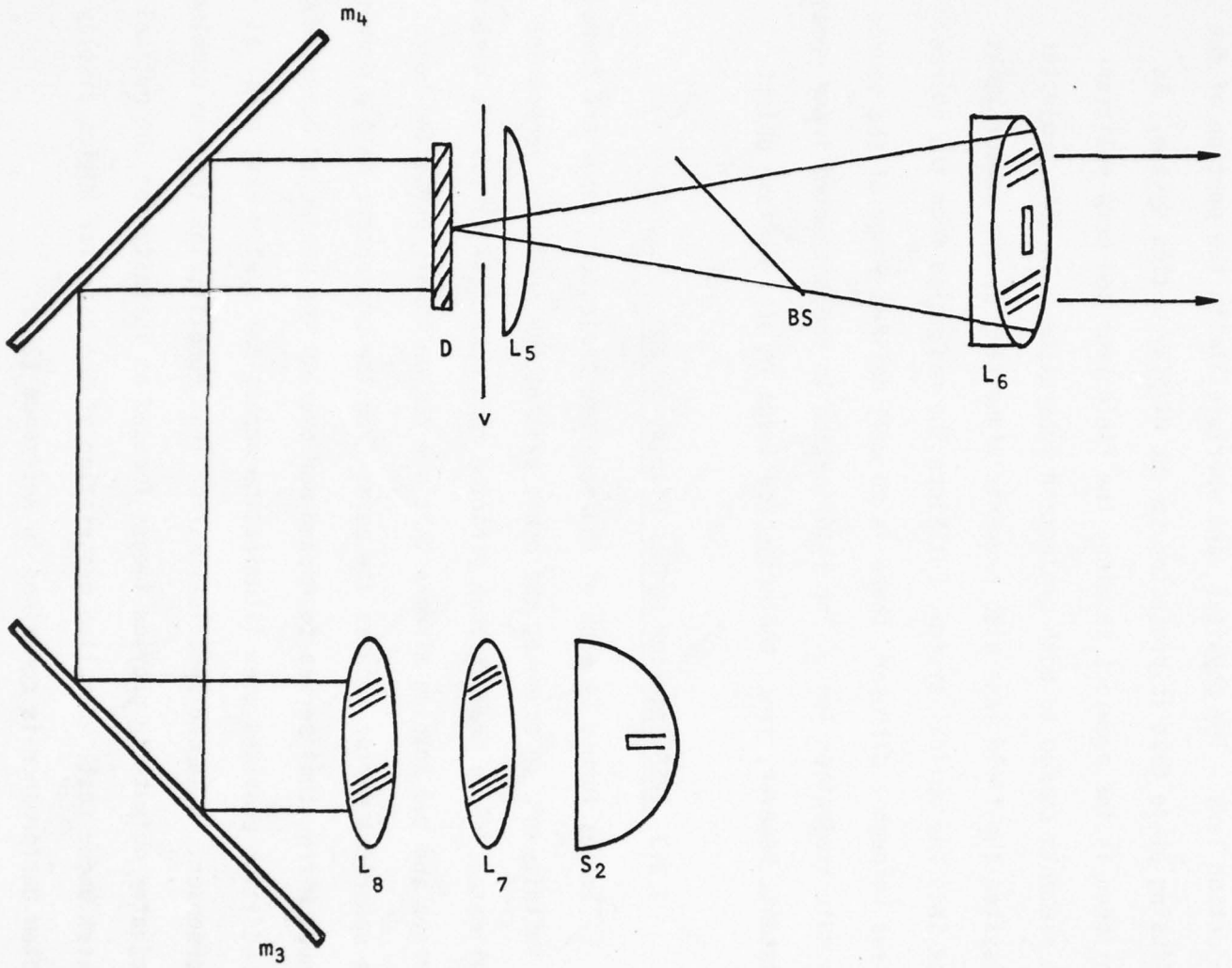

FIGURE 6-5. UV/VIS FUSELAGE TARGET PROJECTOR

The illuminated diffusing plate acts as an object for the main projection lens. The physical vane aperture limits the portion of the diffusing plate that is projected to the display optics system. As mentioned in the previous section, the field lens and beam splitter are elements common to both projection subsystems. In this projector subsystem the field lens also prevents vignetting as the sensor looks back into the optical system, but since the radiation from the source passes through a diffuser, there is no well defined image of the source in the main projection lens. The illumination in the projected image remains constant, however, since the projected image is of a diffuse object.

6.2.3 IRSS Exterior Optics Display System

Images formed by each of the separate projector lenses are formed at infinity or, in essence, the beams exiting the projector lenses are collimated. Each beam is then directed to a spherical mirror via directional mirrors and two folding mirrors that are common to all projected beams. The spherical mirror focuses the beams from the projectors onto a dimpled convex mirror that serves to expand and overlap the projected beams and, in addition provides even illumination across the system exit pupil at the sensor. A second spherical mirror than recollimates the now combined projector outputs to provide images focused at infinity for the optical system under test. Detailed description of the exterior optics display system performance is contained in Reference [3-1].

It should be noted that any modification to the exterior optics display system was beyond the scope of this effort. In effect, any radiance transfer characteristic inherent in the present exterior optical display system must remain unchanged since it will affect the performance of the other projection subsystems within the IRSS.

Table 6-1 lists all optical components of the UV/VIS projection system with pertinent parameters and functions.

6.3 DEVELOPMENT OF RADIOMETRIC MODEL

6.3.1 Rationale

The foregoing discussion, and the analytical developments contained in Appendices B and C, have been supplemented by the test data of Section 5, and all have been utilized to determine the appropriate total system transfer function T (radiance throughput) to be used in the geometrical radiance invariance theorem:

$$N_i = TN_s \tag{6-1}$$

where N_i is the radiance of the final image, and N_s is the source radiance. It is obvious that T includes transmission and reflection losses; however, for those beam geometries where the radiance theorem is invalid, an appropriate additional loss factor must be inserted.

TABLE 6-1. OPTICAL COMPONENT LIST FOR UV/VISIBLE PROJECTORS

OPTICAL ELEMENT	FUNCTION	TRANS-MISSION VALUE*	PHYSICAL CHARACTERISTICS
S_1, Varian VIX-500 Xenon illuminator	Source of radiation for background projector		Electrical Input Power: 500 W Exit Port Diameter: 48 mm Beam Divergence: 8° Arc Spacing: 2.5 mm Reflector Surface: Silver Parabola Reference: Manufacturer
L_1, L_2 condensing lenses for Varian lamp	Forms an image of the arc source into the relay lens, L_4, and provides even illumination across the cloud wheel filter for projection onto the vane assembly	τ=0.92	Diameter: 2 in. Effective Focal Length: Approximately 25.5 in. Material: Fused Quartz Reference: None Available
M_1, Folding Mirror	Beam steering device	ρ=0.78	Surface: Front aluminized Vendor: Edmund Scientific Reference: Test results and Appendix B
L_3	Shortens effective back focal length of L_1, L_2	τ=0.92	Material: Fuzed Quartz Focal Length (White Light): 4 in. Clear Aperture: 1.25 in. Thickness: 0.25 in. Shape: Plano-convex Reference G.E. Drawing No. 47C149055
C, Cloud Wheel	Filter to provide cloud scene images	τ=0.77	Material: Fused Quartz and Dielectric Filter Reference: IRSS Operation and Maintenance Manual Vol. II and Test Results

*ρ = reflectance in ultraviolet
τ = transmittance in ultraviolet

TABLE 6-1. OPTICAL COMPONENT LIST FOR UV/VISIBLE PROJECTORS (Continued)

OPTICAL ELEMENT	FUNCTION	TRANS-MISSION VALUE*	PHYSICAL CHARACTERISTICS
M_2, Folding Mirror	Beam steering device	ρ=0.78	Surface: Front Aluminized Reference: Appendix C
L_4, Relay Lens	Images cloud wheel onto vane mechanism	τ=0.92	Effective Focal Length: 2.249 in. Diameter: 1.2 in. Thickness: 1.06 in. Vendor: Diffraction Limited Reference: Diffraction Limited Test Report
BS, Beam Splitter	Beam steering device	τ=0.43 ρ=0.57	Transmittance/Reflectivity: 43%/57% *Vendor: Broomer Research* Reference: Test Results
L_5, Field Lens	Prevents vignetting as seen from the exterior optics display and re-images source into main projection lens	τ=0.92	Diameter: 2.9 in. Focal Length: 8 in. Thickness: 0.4 in. Material: Fused Quartz Reference: G.E. Drawing No. 47C149055
L_6, Projection Lens	Main projection lens for fuselage and background projections	τ=0.92	Clear Diameter: 1.2 in. Focal Length: 7.5 in. Vendor: Diffraction Limited Thickness: 1.5 in. Type: Double Convex Refractive Achromat Reference: Diffraction Limited Test Report

*ρ = reflectance in ultraviolet
τ = transmittance in ultraviolet

TABLE 6-1. OPTICAL COMPONENT LIST FOR UV/VISIBLE PROJECTORS (Concluded)

OPTICAL ELEMENT	FUNCTION	TRANS-MISSION VALUE*	PHYSICAL CHARACTERISTICS
S_2, Fuselage Projector Source	Provides illumination for fuselage targets	—	Input Power: 300 W Vendor: ILC Technology Reference: None Available
L_7, Collimating Element for ILC Source Lamp	Collimates radiation to illuminate diffusing plate	τ=0.92	Clear Aperture: 1.875 in. Focal Length: 7 in. Type: Plano Convex Thickness: 0.25 in. Reference: G.E. Drawing No. 47C149130
L_8, Collimating Element for ILC Source Lamp	Collimates radiation to illuminate diffusing plate	τ=0.92	Clear Aperture: 1.875 in. Focal Length: 3.5 in. Type: Bi Convex Thickness: 0.42 in. Reference: G. E. Drawing No. 47C149130
M_7, M_8 Folding Mirrors	Beam steering devices	ρ=0.78	Surface: Front Aluminized Reference: Appendix C

*ρ = reflectance in ultraviolet
τ = transmittance in ultraviolet

We neglect the implicit wavelength dependence and separate T into component parts, t_p and t_d, corresponding to the separate transmissions of the projector and display optics, respectively. Then we can later decompose t_p and t_d into component losses. From Equation (6-1),

$$N_i = (t_p t_d) N_s \ . \qquad (6\text{-}2)$$

We can also break down t_p into the radiance transfer of the target subprojector, and the background subprojector. Although we must know the transfer of the display optics, t_d, we are not free to change any component there in an attempt to improve the total system transfer factor.

In the following sections, separate transfer functions are derived for the UV and visible spectral regions (in the Barnes radiometer pass bands) for both the target and background projectors. The projector transfers are characterized down to the component level using the data of Sections 5 and 6, and Appendices B and C. The predicted radiances are compared to measured values in Table 6-6 and the derivations shown in Tables 6-2 through 6-5.

The source radiance value for the UV background projector, shown in the single entry of the right-most column of Table 6-2, is measured; the radiance value for the target source in the UV spectrum (Table 6-3) is scaled from the curve of Figure 5-5, since the source radiance was

TABLE 6-2. RADIANCE THROUGHPUT FOR UV BACKGROUND PROJECTOR, UV BAND

SUBSYSTEM	COMPONENT/ TYPE NAME	COMPONENTS	LOSS TERMS: PER ELEMENT (SOURCE)	LOSS TERMS: TOTAL FOR COMPONENT TYPE	LOSS TERMS: TOTAL FOR SUBSYSTEM	LOSS TERMS: TOTAL SYSTEM	RADIANCE (W/cm^2-sr)
PROJECTOR	LAMP	500 W LAMP	-	-	-	-	17.6
	MIRRORS	M_1 M_2	.78 .78 (APPENDIX C)				(TABLE 5-10)
				.60			
	LENSES	COLLIMATOR (2) L_1 L_2 CLOUD WHEEL LENS L_3 RELAY L_4 FIELD (2 PASSES) PROJECTION L_6	.92 .92 .92 .92 .92 (SECTION 6.)				
				.56			
	VANES	-	.011 (APPENDIX B)	.011			
	BEAM SPT.	-	.23 (SECTION 5.5.2)	.23			
	CLOUD WHL.	-	.77 (SECTION 5.5.1)	.77			
					.00065		
DISPLAY OPTICS	MIRRORS	9 MIRRORS, INCLUDING DIMPLED MIRROR	$(.78)^9$ (APPENDIX C)	.107			
	MIRROR (DIMPLED)	PUPIL EXPANSION (REFLECTANCE INCLUDED IN ABOVE)	.00738 (SECTION 5.4)	.00738			
					.00079		
TOTAL SYSTEM TRANSFER						5.1×10^{-7}	

TABLE 6-3. RADIANCE THROUGHPUT FOR TARGET PROJECTOR, UV BAND

SUBSYSTEM	COMPONENT/ TYPE NAME	COMPONENTS	LOSS TERMS: PER ELEMENT (SOURCE)	LOSS TERMS: TOTAL FOR COMPONENT TYPE	LOSS TERMS: TOTAL FOR SUBSYSTEM	LOSS TERMS: TOTAL SYSTEM	RADIANCE (W/cm^2-sr)
PROJECTOR	LAMP	300 W LAMP	-	-	-	-	8.1*
	MIRRORS	M_3 M_4	.78 (APPENDIX C) .78				*Estimated from Figure 5-4
				.60			
	LENSES	COLLIMATOR (2) L_7L_8 FIELD L_5 PROJECTION L_6	$.92^2$ .92 (SECTION 6.) .92				
				.72			
	DIFFUSER	-	.011 (APPENDIX B)	.011			
	BEAM SPT.	-	.42 (SECTION 5.) (TABLE 5-3)	.42			
	CLOUD WHL.	none	-	-			
					t_p = .0020		
DISPLAY OPTICS	MIRRORS	9 MIRRORS, INCLUDING DIMPLED MIRROR	$(.78)^9$ (APPENDIX C)	.106			
	MIRROR (DIMPLED)	PUPIL EXPANSION (REFLECTANCE INCLUDED IN ABOVE)	(SECTION 5.)	.00738			
					t_D = .00079		
TOTAL SYSTEM TRANSFER						T = 1.6×10^{-6}	

TABLE 6-4. RADIANCE THROUGHPUT FOR BACKGROUND PROJECTOR, VISIBLE BAND

SUBSYSTEM	COMPONENT/ TYPE NAME	COMPONENTS	LOSS TERMS: PER ELEMENT (SOURCE)	LOSS TERMS: TOTAL FOR COMPONENT TYPE	LOSS TERMS: TOTAL FOR SUBSYSTEM	LOSS TERMS: TOTAL SYSTEM	RADIANCE (W/cm^2-sr)
PROJECTOR	LAMP	500 W LAMP	-	-	-	-	213
	MIRRORS	M_1 M_2	.82 .82 (APPENDIX C)				
				.67			
	LENSES	COLLIMATOR (2) L_1 L_2 CLOUD WHEEL LENS L_3 RELAY L_4 FIELD (2 PASSES) L_5 PROJECTION L_6	$.93^2$ .93 .93 $.93^2$ .93 (SECTION 6.)				
				.60			
	VANES	-	.016 (APPENDIX B)	.016			
	BEAM SPT.	-	.23 (SECTION 5.5.2)	.23			
	CLOUD WHL.	-	.77 (SECTION 5.5.1)	.77			
					.00113		
DISPLAY OPTICS	MIRRORS	9 MIRRORS, INCLUDING DIMPLED MIRROR	$(.82)^9$ (APPENDIX C)	.168			
	MIRROR (DIMPLED)	PUPIL EXPANSION (REFLECTANCE INCLUDED IN ABOVE)	.00738 (SECTION 5.4)	.00738			
					.00123		
TOTAL SYSTEM TRANSFER						1.4×10^{-6}	

TABLE 6-5. RADIANCE THROUGHPUT FOR TARGET PROJECTOR, VISIBLE BAND

SUBSYSTEM	COMPONENT/ TYPE NAME	COMPONENTS	LOSS TERMS: PER ELEMENT (SOURCE)	LOSS TERMS: TOTAL FOR COMPONENT TYPE	LOSS TERMS: TOTAL FOR SUBSYSTEM	LOSS TERMS: TOTAL SYSTEM	RADIANCE (W/cm^2-sr)
PROJECTOR	LAMP	300 W LAMP	-	-	-	-	106
	MIRRORS	M_3 M_4	.82 .82 (APPENDIX C)				
				.67			
	LENSES	COLLIMATOR (2) L_7L_8	$.93^2$				
		FIELD L_5	.93 SECTION 6.				
		PROJECTION L_6	.93				
				.75			
	VANES	-	.016 (APPENDIX B)	.016			
	BEAM SPT.	-	.42 (SECTION 5.5.2)	.42			
	CLOUD WHL.	none					
					.0034		
DISPLAY OPTICS	MIRRORS	9 MIRRORS, INCLUDING DIMPLED MIRROR	$(.82)^9$ (APPENDIX C)	.168			
	MIRROR (DIMPLED)	PUPIL EXPANSION (REFLECTANCE INCLUDED IN ABOVE)	(.00738) (SECTION 5.4)	.00738			
					.00123		
TOTAL SYSTEM TRANSFER						4.2×10^{-6}	

TABLE 6-6. MODEL COMPARISON AND PREDICTED ULTRAVIOLET RADIANCE

.29 - .37 μmeters (measurement band)					.35 - .40 μ meters (corrections)			
PARAMETER / SYSTEM	LAMP POWER (W)	RADIANCE THROUGH-PUT, T	ESTIMATED IMAGE RADIANCE N_i ($\mu W/cm^2$-sr)	MEASURED IMAGE RADIANCE N_i ($\mu W/cm$-sr) TABLE 5-2	RADIOMETER WEIGHTING FUNCTION (APPENDIX "A")	SOURCE EXTRAP-OLATION SEC. 5-3	INCREASE IN RADIANCE THROUGHPUT*	ESTIMATED RADIANCE IN BAND $\mu W/cm^2$-sr
BACKGROUND UV	500	$.51 \times 10^{-6}$ (TABLE 6-2)	8.8	10.6	1.82	1.32	1.15	24.3
TARGET UV	300	1.6×10^{-6} (TABLE 6-3)	12.8	18.8	1.86	1.32	1.15	36.1
BACKGROUND VIS	500	1.4×10^{-6} (TABLE 6-4)	298	168	—	—	—	—
TARGET VIS	300	4.2×10^{-6} (TABLE 6-5)	352	not measured	—	—	—	—

*ASSUMES A ONE PERCENT INCREASE IN REFLECTANCE OVER ALL ELEVEN MIRRORS FROM .28 - .37 TO .35 - .40 μm

not measured directly. It is clear from a comparison of Tables 6-2 and 6-3 that the radiance throughput of the target projector is approximately twice that of the background projector. The radiance throughput for the visible is estimated to be about 2.5 times that of the UV in the background projector, as is evident from a comparison of Tables 6-2 and 6-4.

The results of the radiance throughput estimates of Tables 6-2 through 6-5 are summarized in Table 6-6, where they favorably compare with measured values in the UV, and less so in the visible. The right columns include correction factors used to scale the apparent radiance in the 0.27 μm to 0.38 μm band to the actual radiation in the 0.35 μm to 0.40 μm band. The figures in the right column are used as base values which must be increased to achieve the required radiance.

7. PERFORMANCE OF SELECTED CONCEPT

7.1 REVIEW OF DESIGN OPTIONS

In order to increase the radiance output of the projector without modifying the exterior optics, the radiance throughput may be increased by reducing transmission and reflection loses, increasing the source lamp radiance, or both. A larger lamp can always be chosen that increases the radiation solid angle or has a higher radiance. Unfortunately, the gains achievable *solely* through this mechanism do not meet the requirements of Section 4. Part of the problem in using a different lamp is the inability of conventional optics to utilize much of the emitted radiation, and to uniformly illuminate the required (vane) area. Thus, if a stronger source is chosen, the radiance losses must also be reduced inside the projector itself to meet the requirements. It is important to point out that although the pupil expansion factor explained in previous sections is assigned to the display optics, it is really an interface loss since the pupil expansion is directly proportional to the area of the source as imaged from the vane blades into the projection lens. In other words, if a two inch projector lens were used and the remainder of the projector modified such that this lens was completely filled, the pupil expansion (loss) factor would go down by a factor of approximately four. This probability was ruled out because the great amount of redesign required in the projectors and the pupil size at the exit of the projector.

7.2 RECOMMENDED DESIGN CHANGES

7.2.1 Background Projector

In examination of Table 6-2, we see where improvements are possible in the background projector. Clearly, it is not advantageous to modify (increase) the radiance throughput of the display subsystem. Thus, only the projector loss terms can be modified. As is evident from the table, the term that creates most of the loss in the projector itself are the vanes; The implication of raising the present loss value to close to unity is investigated then the impact of other modifications, which, for this projector, involve component changes only is examined: the new vane mechanism, high reflectivity mirrors, a more powerful lamp, and a recoated cloud wheel.

7.2.1.1 Vane Redesign

The required vane characteristics need to be restated, since they involve a compromise between two competing objectives: imaging of the cloud wheel and obtaining the maximum background radiance at the display mirror. Thus, the vanes should be of a highly reflecting material capable of (1) providing, in concert with the field lens, a uniform background radiance that does not change as the vane mechanism is opened and closed, and (2) creating an image of the cloud wheel that can be projected into the first spherical mirror of the collimating display optics.

If results of Equation (B-18) Appendix B, are recalled, it can be seen that an increase in the radiance transfer can be realized by decreasing

the angular spread $\Delta\theta$ of the reflected radiation, and by increasing μ, the reflecting efficiency. The transfer could be made almost arbitrarily large by decreasing $\Delta\theta$ to much less than one degree, i.e., by making the vanes almost perfect specular reflectors. However, some degree of diffuseness is required in order to image the cloud wheel.

This amount of diffuseness required to image the cloud wheel is not derivable by conventional methods, and a test program must be implemented to determine this value. (See Section 8., *Recommendations).* Furthermore, it is important to recollect that the result of Equation (B-18) defines only the *maximum* of the reflectance distribution, and the radiance transfer term, Equation (B-28), is strictly applicable to collimated light and is achievable only in an aberration-free system with an infinitesimally small source. Therefore, the derivations here and in Appendix B are limited to first-order effects and designate desirable design trends but do not totally define all the specifications of each parameter. Again, these variances are best investigated with hardware testing.

It should be remembered at this point that the illumination at any small area on the vanes is due to a radiance from all parts of the source, as imaged in the relay lens, and collimated (approximately) by the field lens. An important inference from this is that the finite size of the source, which causes the beam exiting the field lens and impinging on the vanes to be slightly diverging, allows each small area to fully illuminate the projector system exit pupil in the projection lens, even if the mirror is purely specular.

(Of course, for a true point source, and an ideal, specular mirror, this would not be the case.)

In spite of these reservations, however, a baseline vane design concept can be selected which could serve as a starting point for further analysis and testing. An aluminim-coated ground glass vane material of an rms roughness of approximately 0.07 microns was selected. According to Figure B-3, this denotes a surface roughness parameter (SRP) of 0.18 at .3750 μm, with a beamspread of 6 degrees. Aluminum coated vanes with a dielectric protective layer, such as SiO_2, can have a reflectance (efficiency) of near 0.84.

Thus, by applying Equation (B-20) to the present case,

$$\rho'_{max} = \frac{(39.4)(.84)}{6} \tag{7-1}$$

$$\rho'_{max} = 5.5 \quad sr^{-1} \tag{7-2}$$

Since in the preferred design, the solid angle of the source remains the same as in the present projector, Equation (B-28), then:

$$t'_v = .226 \qquad (7\text{-}3)$$

where the prime denotes the modified vane radiance factor. Recalling Equation (B-28), it can be seen immediately that the increase in radiance transfer α_v, is:

$$\alpha_v = \frac{t'_v}{t_v} = \frac{.226}{.011} = 20.5 \qquad (7\text{-}4)$$

7.2.1.2 Source Lamp Replacement

It is clear from Equation (7-4) that the principle gain in radiance will occur through the use of semi-specular vanes; however, from the upper entry in the right-most column of Table 6-6, the new radiance value is only $\sim$ 500 $\mu W/cm^2$-sr, still not within requirements. Therefore, additional changes are required.

A convenient and inexpensive modification is to replace the present 500 W Varian lamp with an 800 W Varian lamp. The higher power lamp is the same size as the present 500 W lamp, and contains the same integral parabolic reflector (thus obviating a new condensor lens design configuration), and is therefore completely interchangable. A higher wattage power supply of course, will be required. The increase in radiance can be approximated from Figure 5-4.

$$\sigma_m = 2.15 \qquad (7\text{-}5)$$

A small additional increase in radiance may be achieved with use of a UV-enhanced rhodium reflector rather than the standard silver. Whether this improved performance is worth the cost is indeterminant at this point.

7.2.1.3 Mirror Replacement

Although the implementation of the two modifications discussed in the previous paragraphs would increase the background radiance to greater than 1.0 mW/cm^2-ster, and above the desirable requirement of Table 4-3, an additional increase in the radiance can be realized through replacement of the two mirrors m_1 and m_2. A dielectric mirror, or MLD (multiple-layer-dielectric) mirror can have reflectance of over 95 percent between .35μm - .40μm. Thus, the increase in radiance from the mirror is, since the old mirrors are presumed to be 78 percent reflecting,

$$\sigma_m = 1.48 \qquad (7\text{-}6)$$

7.2.1.4 Cloud Wheel Modification

The measured transmission of the cloud wheel was lower than expected, particularly if it is AR coated. Conceivably, if a cloud wheel of suitable material, i.e., quartz or fuzed silica , were AR coated, a 1 cm thick sample should have a transmission of greater than 92 percent. The small increase in transmission accrued from procurement of a new cloud wheel is not considered worth the cost, since the radiance achievable from the three modifications already presented already exceeds the optional requirement, as will be shown in the next subsection.

Rather, the modifications to the cloud wheel suggested are to achieve a reasonable "delta" radiance between the sky and clouds, and involve a recoating, with appropriate filter, of the semi-opaque (i.e., sky) portions of the wheel. The filter factor should be between three and four to match the results of Tables 4-1 and 4-2.

7.2.1.5 Predicted Background Radiance

The results from Table 6-6 can be combined where the estimated radiance in band for the UV background is

$$N_{.35-.40} = 24.3 \times 10^{-6} \text{ W/cm}^2\text{-sr} \tag{7-7}$$

with the transfer factors derived previously to compute the new radiances with primes denoting the new value.

$$N'_{.35-.40} = (24.3 \times 10^{-6})(20.5)(2.15)(1.48) \tag{7-8}$$

$$N'_{.35-.40} = 1.59 \text{ mW/cm}^2\text{-sr} \tag{7-9}$$

This value is above the requirement of Table 4-3.

7.2.2 Target Projector

The basic design modifications, as discussed in subsection 7.2.1 for the background projector, apply in general to the target projector. For example, the diffusing plate D of Figure 6-5 must be made less diffusing if system radiance transfer is to be made acceptable. However, the modifications in the target projector involve more than just component changes as was the case for the background projector. The reason for this is based on the fact that the present target projector operates in a "searchlight" mode and, at the diffuser distance and with the source/condenser configuration as currently installed, the capacity to achieve the required radiance with only a more specular diffusser is limited, depending to some extent, on the radiance uniformity of desired accross the total (open) vane area.

Analyses performed by Dynetics indicate that a new lamp, (the same as recommended for the background projector) a new 60 cm condenser mode configuration which includes deletion of the two translational mirrors, a new diffuser, and servo-controlled iris, will enable fulfillment of all of the requirements of Section 4. Also, insertion of a heat absorbing filter is suggested to reduce any potential thermal problem. The proposed design concept is illustrated in Figure 7-1.

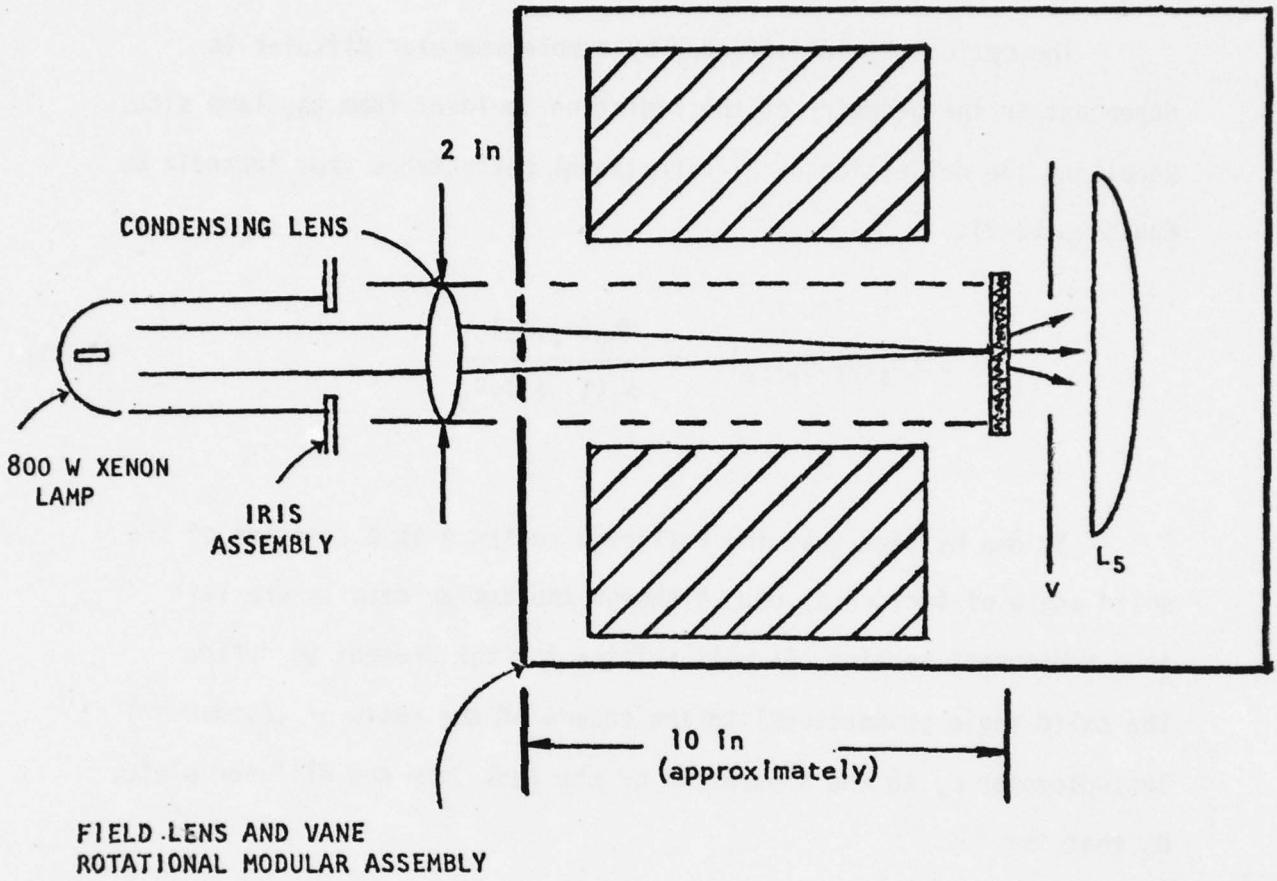

FIGURE 7-1. PROPOSED FUSELAGE TARGET PROJECTOR DESIGN MODIFICATIONS

7.2.2.1 Diffuser Modifications

The optical "gain" afforded by a more specular diffuser is dependent on the geometry of the radiation incident from the lamp side. Recalling the definition of bi-directional reflectance from Appendix B, Equation (B-2),

$$\rho'(\theta_i,\phi_i;\theta_r,\phi_r) = \frac{dN_r(\theta_r,\phi_r)}{N_i(\theta_i,\phi_i)d\Omega_i} \tag{7-10}$$

It can be seen that the reflected radiance is a function of the solid angle of incidence, $d\Omega$. Although the design details are left to a subsequent section, it will suffice for the present to define the solid angle proportional to the square of the ratio of (condenser) lens-diameter L, to the separation of the lens from the diffuser plate, D, that is

$$d\Omega_i \cong \left(\frac{L}{d}\right)^2 \text{ sr.} \tag{7-11}$$

For L = 2 inches, and d = 11 inches,

$$d\Omega_i = .10 \text{ sr} \tag{7-12}$$

Then, the radiance transfer as defined with respect to the bi-directional reflectance is, from Equation (7-10),

$$t = \rho' d\Omega_i \tag{7-13}$$

$$t = .10\rho' \tag{7-14}$$

Equation (7-10) is used with equation (B-29), of Appendix B: It can be seen that the radiance transfer with just the condensor change is,

$$t = .146 \tag{7-15}$$

or about thirteen times the old value. This would indicate an acceptable value; however, the image must be spread over an area of about one square inch, so the focus of lens must be beyond the diffuser, or about twenty inches. This reduces the solid angle by a factor of four to about 0.25 sr. If compensated for by increasing the reflectance to 4.64 sr^{-1}, the radiance increase is just

$$\rho_d = \frac{.146}{.011} = 13.2 \tag{7-16}$$

Use of the Varian lamp will afford (from Figure 5-4) an increase in radiance over the 300 W lamp of

$$P_L = 4.1 \tag{7-17}$$

By deleting the two mirrors, a gain is realized of

$$\rho_m = \frac{1}{(.78)^2} = 1.64$$

Since the current estimated radiance is 36.4 $\mu W/cm^2$-sr, and a heat absorbing factor of .76, the radiance available with the redesign is

$$N' = (36.4)(13.2)(4.1)(1.64)(.76)\ \mu W/cm^2\text{-sr}$$

$$N' = 2.461\ mW/cm^2\text{-sr}$$

but the iris factor is $\left(\frac{1.6}{2.0}\right)^2 = .64$

so

$$N' = 1.571\ mW/cm^2\text{-sr}$$

8. RECOMMENDATIONS

The analyses performed, and tests conducted during the course of this contract have led to identification of changes in the UV-visible projector system which, Dynetics, Inc. believes, would result in greatly enhanced system performance if implemented in the manner described. The rationale for these changes is based on the best available empirical and theoretical evidence since there is strong correlation between the projector model, upon which the design modifications are based, and the measured data. However, the validity of the model has not been verified against wide excursions in component performance parameters, and in particular, to the recommended use of semi-specular vanes. Also, a complete model for the target portion of the projector was not developed during the effort because of lack of performance data.

In addition to corroboration of the model for specular vane blades, and therefore, substantiation of this design change, it must be remembered that increasing the radiance transfer (with specular vanes) satisfies only one part of the total requirements of a successful design.

In addition, the cloud wheel must be imaged which, of course, cannot be done with a purely specular mirror (tests conducted at DYNETICS, demonstrated that an image could be formed on not only the matt inside of a piece of stock aluminum foil, but on the glossy side as well. For a

mirror, the only image visible was due to dust and other scattering from the mirror surface). From the results of Appendix B, it can be seen that there is clearly a tradeoff here: one would wnat a surface specular enough to give an adequate radiance transfer, but diffuse enough to image, and subsequently project the cloud wheel edge. These functions must be accomplished, of course, while maintaining a constant and uniform background radiance against changes in target aperture size.

DYNETICS, INC., recommends a four to five month *Design Validation Program*, in which the effects of differing vane/diffuser materials on the radiometric transfer of the target and background projectors may be systematically assessed and quantitatively evaluated through conduction of a coordinated test schedule.

This program will quantify components for alternate concepts that will enable requirements set forth in Section 4. to be realized. Dynetics believes this a cost effective, minimal risk effort to assist in meeting the present needs of the IRSS facility to test and evaluate state-of-the-art dual mode sensor systems.

APPENDICIES TABLE OF CONTENTS

AD-A070 898 DYNETICS INC HUNTSVILLE ALA F/G 17/5
DESIGN OF IRSS PROJECTORS.(U)
NOV 78 DAAK40-78-C-0070
UNCLASSIFIED MIRADCOM-78-0070-022 NL

2 OF 2
AD
A070898

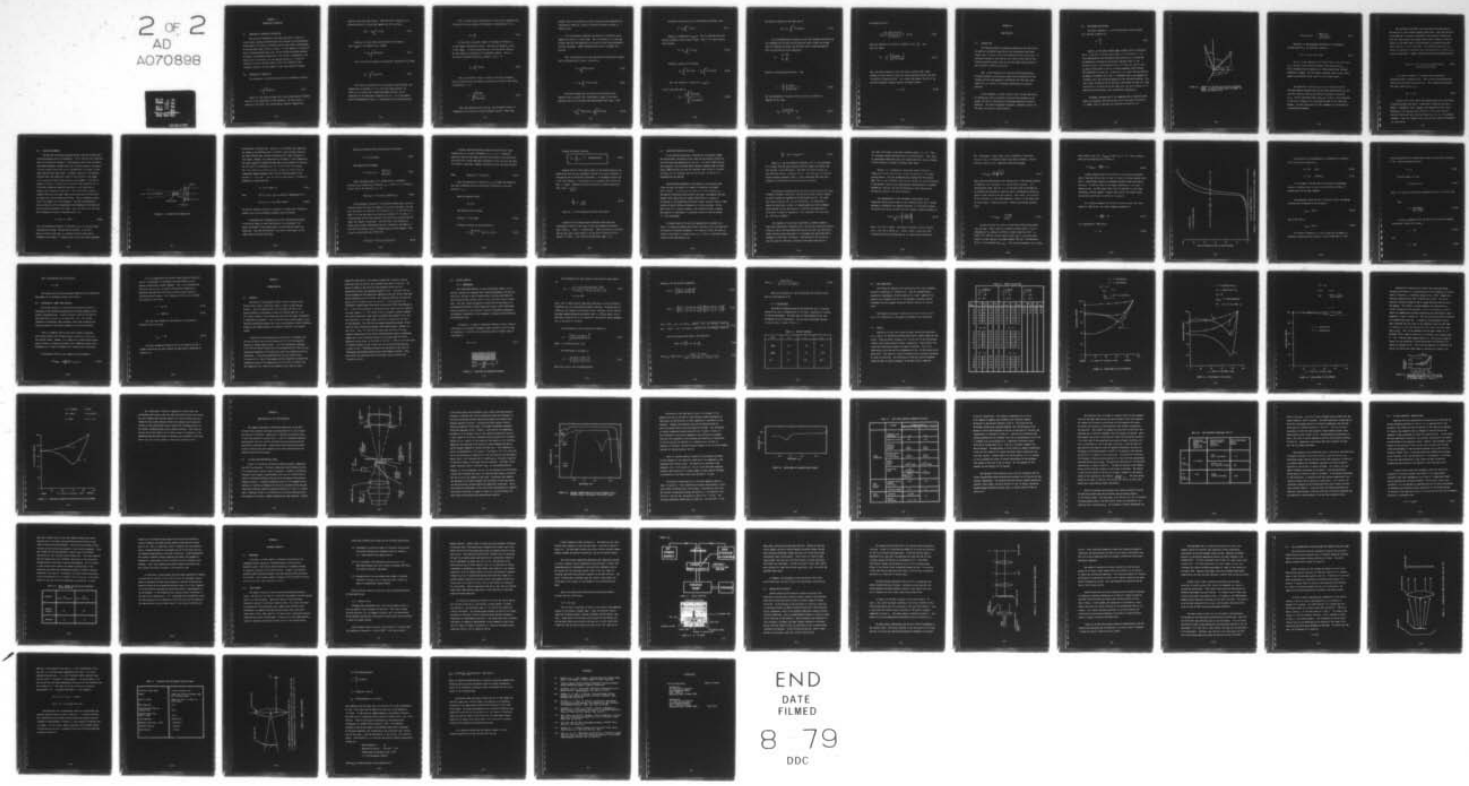

END
DATE
FILMED
8 79
DDC

APPENDIX A

RADIOMETER CALIBRATION

A.1 IMPORTANCE OF RADIOMETER CALIBRATION

The use of the radiometer in the tests described in Section 5. raised several questions concerning both the accuracy of the measurements, and the impact of different calibration sources upon proper interpretation of the data when using a xenon arc source. In this appendix, an analytical basis is presented which shows that, for the calibration method employed by Barnes, the radiometer manufacturer, the scaling is independent of the source used in calibration, and the apparent measured, or "effective" radiance is the true radiance times a scale factor defined by the radiometer response, and the integral of the source spectral radiance.

A.2 MATHEMATICAL FORMULATION

The radiometer is calibrated using the basic radiometric equation:

$$V = \int_{\lambda_1}^{\lambda_2} N(\lambda)R(\lambda)d\lambda \qquad \text{(A-1)}$$

where V is the output voltage, $N(\lambda)$ is the target spectral radiance, and $R(\lambda)$ is the responsivity of the radiometer; this last term is a function of the f/no, lens transmittances, detector responsivity,

amplifier gains and other factors. Often the actual responsivity is defined relative to a normalized responsivity $r(\lambda)$ such that

$$R(\lambda) = R_n \int_{\lambda_1}^{\lambda_2} r(\lambda) d\lambda \qquad \text{(A-2)}$$

where R_n is a scale factor and normalized to the peak of $r(\lambda) = r_{max}(\lambda)$. So, Equation (A-1) becomes

$$V = R_n \int_{\lambda_1}^{\lambda_2} N(\lambda) r(\lambda) d\lambda \qquad \text{(A-3)}$$

This is the form of equation used by Barnes, Reference [5-1], where

$$N_T = \int_{\lambda_1}^{\lambda_2} N(\lambda) r(\lambda) d\lambda \qquad \text{(A-4)}$$

This term R_n in Equation (A-3) is the scale factor relating the responsivity to the peak of $r(\lambda)$, and is the same as Barnes' K_s. Their K_s is a *constant* for a system wavelength inverval, and is *independent* of the magnitude of spectrum of $N(\lambda)$. It is the method used in determination of K_s (i.e., "calibration") that confusion arises.

Thus, a factor C may be defined which is the ratio of Equation (A-6) to Equation (A-4) and because of the manner of normalization $C \geq 1.0$.

$$K_s = \frac{V}{N_T} \tag{A-5}$$

For any other source, (for example a blackbody at different T, or neon lamp), a different N_T results. This does not change K_s, since V also changes. It must be noted that N_T is not the actual radiance, but the radiance as weighted by the radiometer response. That is, the actual integrated radiance N_a, between λ_1 and λ_2 is

$$N_a = \int_{\lambda_1}^{\lambda_2} N(\lambda)d\lambda \tag{A-6}$$

Thus, we may define a factor C, which is the ratio of Equation (A-6) to Equation (A-4) and because of the manner in which we have chosen to normalize, $C \geq 1.0$.

$$C = \frac{\int_{\lambda_1}^{\lambda_2} N(\lambda)d\lambda}{\int_{\lambda_1}^{\lambda_2} N(\lambda)r(\lambda)d\lambda} \tag{A-7}$$

Thus, the surprising result that K_s, the calibration factor, is independent of the source for a given waveband interval! After some

thought, this is not surprising, since a different source magnitude and spectrum will effect N_T, raising or lowering the output voltage, by Equation (A-5)

It is interesting to determine the effect of a different source. Suppose this source is a xenon lamp. The root question is, at the same voltage, what must the magnitude of the xenon be to be indistinguishable from the (presumed) $\sim$ 1300k° blackbody source used in original calibration?

Thus, from Equation (A-3), with unprimed and primed values represting the blackbody and Xe source, respectively:

$$V = K_S \int_{\lambda_1}^{\lambda_2} N(\lambda) r(\lambda) d\lambda \qquad \text{(A-8)}$$

$$V' = K_S \int_{\lambda_1}^{\lambda_2} N'(\lambda) r(\lambda) d\lambda \qquad \text{(A-9)}$$

The actual voltage (not the ratio) can be determined from Equation (A-8), since $N(\lambda)$ for a black-body is known, K_S has been measured, and $r(\lambda)$ is available from lamp manufacturer's data. Then:

$$K_S \int_{\lambda_1}^{\lambda_2} N(\lambda) r(\lambda) d\lambda = K_S \int_{\lambda_1}^{\lambda_2} N'(\lambda) r(\lambda) d\lambda \qquad \text{(A-10)}$$

Additional normalization can be introduced by defining a term

$$N = N_s \int_{\lambda_1}^{\lambda_2} n(\lambda) d\lambda \tag{A-11}$$

where N_s is normalized to $r_{max}(\lambda)$. This is important since the *relative* spectrum of the Xe lamp is known. Thus, N' for the Xe source can be written

$$N' = N'_s \int_{\lambda_1}^{\lambda_2} n'(\lambda) d \tag{A-12}$$

Therefore, Equation (A-10) becomes

$$N_s \int_{\lambda_1}^{\lambda_2} n(\lambda) r(\lambda) d\lambda = N'_s \int_{\lambda_1}^{\lambda_2} n'(\lambda) r(\lambda) d\lambda \tag{A-13}$$

Thus, the radiance at λ where $r(\lambda) = r_{max}(\lambda)$,

or N'_s of the xenon lamp is,

$$N'_s = \frac{N_s \int_{\lambda_1}^{\lambda_2} n(\lambda) r(\lambda) d\lambda}{\int_{\lambda_1}^{\lambda_2} n'(\lambda) r(\lambda) d\lambda} \tag{A-14}$$

The effective radiance of the xenon lamp is

$$N'_T = N'_s \int_{\lambda_1}^{\lambda_2} n'(\lambda) r(x) d\lambda \qquad \text{(A-15)}$$

It is the application of Equation (A-15) that produces the difficulty. The radiometer has not been recalibrated with xenon; rather the voltage term V is modified to reflect the different source, recalling Equation (A-7) and calling the actual radiance N_a

$$N_a = CN_T$$

or,

$$N_a = \frac{CV}{K_s}$$

where N_T is given by Equation (A-4). Then:

$$C = \frac{N'_s \int n'(\lambda) d\lambda}{N_s \int n(\lambda) r(\lambda) d\lambda} \qquad \text{(A-16)}$$

But the denominator of Equation (A-16) is just N_T as defined in Equation (A-14), then:

$$N_a = \frac{N_s \int n'(\lambda) d\lambda}{N_T} \cdot N_T \qquad \text{(A-17)}$$

From Equation (A-14):

$$N_a = \left[\frac{N_s \int n(\lambda) r(\lambda) d\lambda}{\int n'(\lambda) r(\lambda) d} \right] \int \quad n'(\lambda) d\lambda \qquad \text{(A-18)}$$

where the numerator of the term in brackets is just $\frac{V}{K_s}$. Thus, the final result:

$$N_a = \frac{V}{K_s} \left[\frac{\int n'(\lambda) d\lambda}{\int n'(\lambda) r(\lambda) d\lambda} \right] \qquad \text{(A-19)}$$

Thus, the actual radiance is just the ratio of voltage V(dB + meter reading) to scale factor K_s times the source weighting function, the term in brackets in Equation (A-19). For a xenon lamp between .28 and .37 μm, with the radiometer response function furnished by Barnes

$$C = 1.82 \qquad \text{(A-20)}$$

APPENDIX B

VANE ANALYSIS

B.1 INTRODUCTION

The fuselage projector transparency mechanism, and specifically, the physical and optical properties of the transparency vanes themselves, exert a critical role in the operation of the UV projector. As outlined in Section 5, the vanes act as a central field stop for the primary projection system, and also form the image (edge contrast) of the cloud wheel radiance distribution.

Thus, a clear formulation of the vane reflecting properties (including changes in polarization state) and the interaction of the incident and exit beam geometry as defined by the field lens, (see Figure 6-3) is critical to a thorough understanding of projector operation.

In this appendix, a review is given, first, on some definitions of reflectances, then an analysis of the collection geometry of the system, and third, a discussion of reflecting properties of typical materials. This data is employed to develop a radiometric factor for the vanes, to be used in other sections.

B.2 REFLECTANCE DEFINITIONS

The total reflectance ρ, of an infinitesimal surface element dA is defined in general by :

$$\rho = \frac{P_r}{P_i} \tag{B-1}$$

where P_i is the total radiant power incident from all directions, and P_r is the total reflected radiant power in all directions. To a first approximation, the reflectance characteristics of a surface may be separated by considering the specular component (that is, the reflection from an infinitesimally small solid angle $d\omega_i$ into an angle $d\omega_r$ which follows Snell's law) or a diffuse component, which follows the Lambertian or cosine law. In any case, it is clear from the defining parameters of Equation (B-1) that ρ is dependent both on the geometry of incidence and on the collection geometry of the reflected radiation. This fact creates the possibility of defining a reflectance for each of a large combination of incidence-collection geometries, and the literature is indeed filled with confusing, even contradictory nomenclature.

Nicodemus, Reference [B-1], has suggested with a relatively wide degree of acceptance, the term *bi-directional reflectance distribution*, ρ', (BDRD), which is defined, with reference to Figure B-1, as

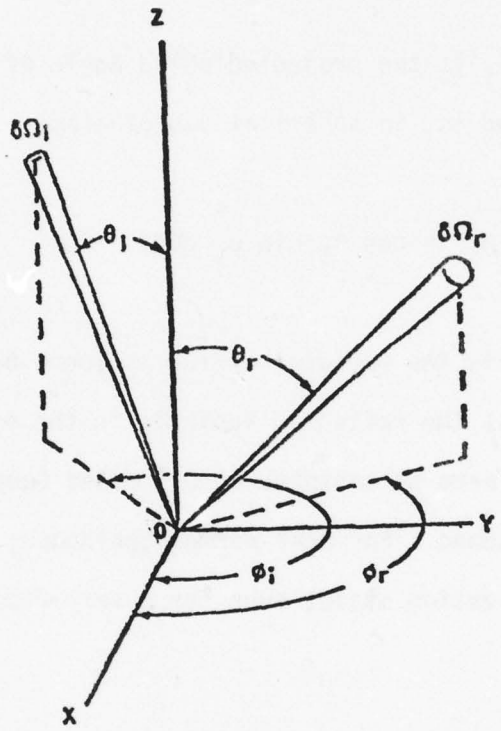

FIGURE B-1. GEOMETRY OF INCIDENT AND REFLECTED ELEMENTARY BEAMS (Z AXIS IS CHOSEN ALONG THE NORMAL TO SURFACE dA ELEMENT AT O)

$$\rho'(\theta_i,\phi_i;\theta_r,\phi_r) = \frac{dN_r(\theta_r,\phi_r)}{N_i(\theta_i,\phi_i)d\Omega'_i} \qquad \text{(B-2)}$$

where $d\Omega'_i$ is the projected solid angle of the elementary incident beam and is, in spherical coordinates:

$$d\Omega_i' = \cos\theta_i \sin\theta_i \, d\theta d\phi \qquad \text{(B-3)}$$

Also, N_i is the radiance of the incident beam in the directions, θ_i,ϕ_i, and dN_r is the reflected radiance in the direction θ_r,ϕ_r, from a selected area dA centered at 0. Mixed (unpolarized) incident radiation is assumed. For near-normal incidence, there is very little change in polarization state, even for a very rough surface.

The differential notation dN_r is used to indicate that the reflected radiance includes both the flux under consideration, N_i, and any other radiation which may be diffusely scattered in direction θ_r,ϕ_r. The net reflectance then, $N_r(\theta_r,\phi_r)$, of dA in a given direction is the sum or integral of all such beams incident on the reflecting element. The full implications of this statement will be brought out in subsequent paragraphs.

The advantage of the BDRD is that any other reflectance may be derived from it, with suitable geometry definitions. Note that the units of the BDRD are in reciprocal steradians, and a specular reflector may have very large values (much greater than unity); a perfect, diffuse reflector, on the other hand, is characterized by a constant (less than unity) value of ρ' in all directions. The reflected radiance N_r is a function of position for points on the reflecting surface, as well as for (θ_r,ϕ_r) at each point. However, Equation (B-2) may be extended to write:

$$N_r(\theta_r,\phi_r) = \int_{\text{collection solid angle}} \rho'\,(\theta_i,\phi_i,\theta_r;\phi_r)N_i(\theta_i,\phi_i)d\Omega'_i \qquad \text{(B-4)}$$

It is useful to define ρ' in terms of the "conventional" reflectance given in Equation (A-1). This is done by multiplying both sides by the collection solid angle $d\Omega_r'$. Thus, neglecting scattering from other angles not at θ_r,ϕ_r ,

$$d\rho = \rho'\, d\Omega_r' \qquad \text{(B-5)}$$

Equation (B-5) helps resolve the apparent physically unrealizable reflectance greater than unity. A good mirror (specular) may have a BDRD $\left[\rho = \rho(0;0)\right]$ over fifty. However, the integration of $d\Omega_r'$ over a hemisphere in the equation (B-5) results in a dirac delta function that has finite value only in the vicinity of $\theta_r = 0$, $\phi_i = 0$, and zero elsewhere. Thus, the integral of $d\Omega_r'$ will be only a few millisteradians for a good mirror.

B.3 REFLECTION GEOMETRY

Now that the reflectance has been defined, the vane incidence and collection geometry must be investigated. This is done by first recalling some of the results of Section 6. The projection lens of the subsidiary, cloud wheel projector, denoted *relay lens*, forms the image of the source. The focal length of the field lens is approximately 8.75 inches, as measured from the front nodal point. As shown in Section 6. the distance from the relay lens nodal point (close to the location of the imaged arc) is also 8.75 inches to the accuracy of measurement. This type of geometry is that of a (refractive) searchlight, whose operation to the first order, neglecting spherical aberration, can be described as follows, with reference to Figure B-2. This figure shows a source S (image of the arc in the relay lens) at the focal point of field lens L. The image (S') will be located at infinity. Since S subtends an angle α from L, the image S' will also subtend α. Now the illumination at a point on the axis will be determined by the brightness of the image and the solid angle subtended by the image. Thus, for points *near the lens*, the illumination is given, for perfect optics, by,

$$E = N_S \omega \; ; \; \omega = \pi \sin^2 \alpha \qquad \text{(B-6a)}$$

N_S is the brightness (radiance) of the object and ω is the solid angle subtended by the image. We have tacitly assumed ω to be small.
Now for a point at the lens, it is obvious that the solid angle ω subtended by the image S' is exactly equal to the solid angle subtended

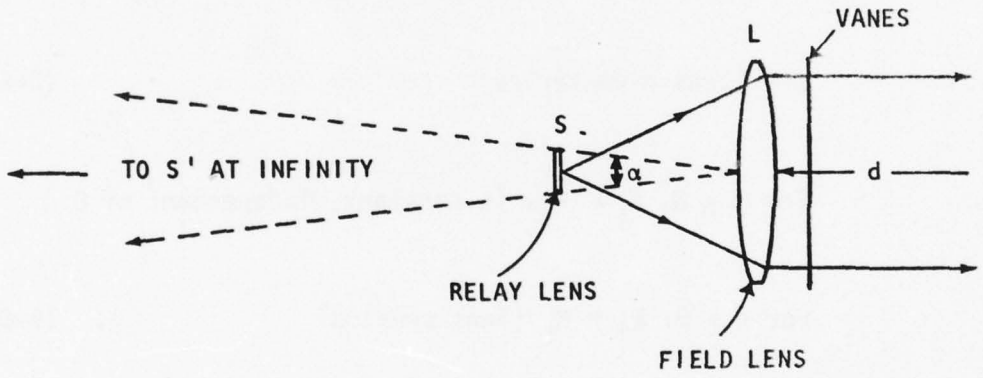

FIGURE B-2. THE OPTICS OF A SEARCHLIGHT

by the source S from the lens. Since S' is at infinity, this angle will not change as the reference point is shifted a short distance along the axis away from the lens, and the illumination will remain constant in this region. However, at a characteristic distance D = (lens diameter)/α, the source image will subtend the same angle as the diameter of the lens, and the source of illumination will be limited by the lens diameter. This solid angle will obviously be equal to (area of lens)/d^2 and the illumination beyond distance D will fall off with the square of the distance d to the lens. Thus, the equations governing the illumination produced by a searchlight are:

$$D = (\text{lens diameter})/\alpha \qquad \text{(B-6b)}$$

Then, For $d \leq D$, $E_i = N_s\omega$ (a constant, independent of D.)

$$\text{For } d \geq D\text{: } E_i = N_s\ (\text{lens area})/d^2 \qquad \text{(B-6c)}$$

The general technique used here is applicable to almost any illumination problem, and it can be restated in general terms as follows:

To determine the illumination at a point, the size and position of the source image, as seen from the point, are calculated. The pupils and windows of the system (again, as seen from the point) are determined. Then the illumination at the point is the product of the image radiance and the solid angle.

Returning to Equation (B-2) and defining an irradiance:

$$E_i = N_i\ (\theta_i,\phi_i)d\Omega_i \tag{B-7}$$

Then Equation (B-2) becomes:

$$\rho'(\theta_i,\phi_i;\theta_r,\phi_r) = \frac{dN_r(\theta_r,\phi_r)}{dE_i(\theta_i,\phi_i)} \tag{B-8}$$

Then, rearranging terms, it is evident that an incremental *irradiance* dE_i incident from a direction θ_i,ϕ_i, results in an incremental *radiance* dN_r in the direction θ_r,ϕ_r of:

$$dN_r(\theta_r,\phi_r) = \rho'(\theta_i,\phi_i;\theta_r,\phi_r)dE_i(\theta_i,\phi_i) \tag{B-9}$$

The differential notation of the reflected radiance dN_r, can be deleted by noting, following the comments of a previous paragraph, that the only contributor to radiation in the directions θ_r, ϕ_r is that due to dE_i. While it is true that some of the radiation reflected off the vanes is reflected again off the rear surface of the field lens, and back onto the vanes, this amount is very small. The field lens is AR (dielectric) coated, and a typical reflectance value for a dielectric film (MgF_2) is less than five percent, even at incidence angles of sixty degrees. Thus, it can be written with very little error,

$$N_r(\theta_r,\phi_r) = \rho(\theta_i,\phi_i;\theta_r,\phi_r)E_i(\theta_i,\phi_i) \tag{B-10}$$

A further simplification may be made by considering the input radiance flux, E_i, as well collimated, or $\theta_i = \phi_i = 0$. (Spherical aberration near the lens edges, and the finite extent of the source near the optical axis create some small divergences of the rays onto the vanes. This effect is very small, however, and does not alter the basic results).

Then: $$N_r(\theta_r,\phi_r) \cong \rho'(\theta_r,\phi_r)\, E_i \qquad \text{(B-11)}$$

Thus, the radiance in a direction θ_r, ϕ_r is simply the product of the input irradiance and the bi-directional reflectance in the same direction, θ_r, ϕ_r.

Recalling Equation (B-6a):

$$E_i = N_s\omega$$

Then Equation (B-11) becomes,

$$N_r(\theta_r,\phi_r) = \rho'(\theta_r,\phi_r)N_s\omega \qquad \text{(B-12)}$$

A radiance transfer can now be defined as

$$t_v = \frac{N_r\ (\theta_r,\phi_r)}{N_s} \cong [\rho'(\theta_r,\theta_r)]\omega \qquad \text{(B-13)}$$

Dropping the angular notation,

$$t_V = \frac{N_r}{N_S} \cong \rho'\omega \quad \text{(dimensionless)} \tag{B-14}$$

Equation (B-14) is the central result of the present analysis, and demonstrates that the vane radiometric transfer (in a given direction) is increased as the bi-directional reflectance ρ' is increased, and the size of the input image N_i, or the distance, are increased, both of which can make ω larger. Equation (B-14) may be written in a more conventional form, since $\rho' = \frac{\rho}{\int d\,\Omega_r'}$:

$$\frac{N_r}{N_S} \cong \frac{\rho\omega}{\int d\Omega_r'} \tag{B-15}$$

where $d\Omega_r'$ is the projected collection solid angle.

Equation (B-15) indicates those conditions under which the radiometeric transfer of the vanes is just the standard reflectance ρ: when $\omega \cong \int d\Omega'_r$. Since ω is quite small, $\int d\Omega'_r$ must also be very small. The only way $\int d\Omega'_r$ can be small is for the mirror (reflector) to be specular in nature. (For a perfect diffuse object $\int d\omega'_r = \pi$).

B.4 REFLECTING PROPERTIES OF METALS

In the previous subsection, a theoretical relationship between the bidirectional reflectance of the vanes and the radiance transfer of the field lens-vane combination was derived. In order to model the present projector, and to indicate where radiance increases might be forthcoming, BDRD functions for both the stainless steel blades as currently installed, and for candidate material and surfaces considered as replacements must be derived.

The reflecting properties of both metallic and dielectric materials has been the subject of a number of theoretical and experimental studies. In particular, the effects of surface roughness on the spectral reflecting characteristics have been investigated, with the general result being that the rougher (mechanically) a surface is (as defined in the appropriate statistical sense), the more likely is that surface to exhibit diffuse reflectance at a given wavelenth. On the other hand, for a constant roughness, the reflectance tends to become more specular as wavelength is increased, and more diffuse at shorter (i.e. UV) wavelengths.

A formula found to fit well with measured data at normal incidence is presented by Bennett and Porteous, Reference [B-2], and quantifies the specular reflectance phenomenon. This equation defines the ratio of specular reflectance of a rough surface, R_s, to that of a perfectly smooth surface of the same material, R_0:

$$\frac{R_s}{R_0} = \exp\left[-(4\pi\sigma_m)^2/\lambda^2\right] \qquad \text{(B-16)}$$

Where σ_m is the rms mechanical roughness, and λ is the wavelength. It is evident from the above equation that the rougher the surface, the less specular is the reflectance. The higher the ratio of R_s/R_0, the more perfectly specular a material will be. The ratio σ_m/λ is called the *surface roughness parameter (SRP)*, κ, and a value much less than unity indicates a surface more likely to be specular in nature.

The authors of Reference [B-2] used disks of AISI Type O1 tool steel hardened to Rockwell 58-60 and a fine surface grinder to obtain samples of various degrees of roughness to verify Equation (B-13). The roughness values used were .82, .21, and .06 microns. For comparison, a typical polished steel, nickel, or aluminum sample will have roughness values between .02 and .005 microns; an optically polished piece of flint glass, as might be employed as a lens component, will have about an .002 micron roughness.

The roughness of the present vane blades is unknown; however, from visual observations, Reference [B-3], and from the strong polarization effects of one of the vane blades noted during the tests and evaluations, (which indicate course machining) it is estimated that the blades have a roughness no finer than .20 microns. From Equation (B-16) we can see that the specular reflectance (related to the energy collected in a

very small solid angle at the Snell reflection angle) is $< 10^{-5}$ that of a perfectly smooth polished mirror of the same material. Thus, there is considerable theoretical basis for assuming that the vanes are largely diffuse reflectors at angles of incidence near normal.

However, it is necessary to expand this somewhat intuitive formulation into one that includes an explicit definition of the BDRD defined earlier. This was accomplished by assuming that the *relative* BDRD, that is, the reflectance that does not include the optical properties of the material itself, can be approximately characterized by a standard mathematical function, and that the properties of real metals may be included by insertion of a simple multiplier.

This approximation is that the BDRD is described by a one dimensional Gaussian with a mean at zero reflection angle, and a "spread" parameter $\Delta\psi$ defined by the standard deviation, or a multiplier thereof. The equation for normal incidence and with azimuthal symmetry assumed, is:

$$\rho'(\theta_r) \propto \frac{1}{\sqrt{2\pi}} \exp\left[-\frac{1}{2}\left(\frac{\theta_r^2}{\Delta\psi^2}\right)\right]. \qquad \text{(B-17)}$$

where $\Delta\psi$ is the 1σ spread. The integral of Equation (B-17) is unity over θ_r from -90 to +90 degrees. Clearly, there is some error with a Gaussian function introduced when $\Delta\theta$ is a considerable fraction of

80°. Fortunately, in most cases, we are interested in the maximum value of $\rho'(\theta_r)$, at reflection angles near normal incidence. Then we can write, with $\Delta\theta = 2\Delta\psi$ = FWHM (Full Width Half Maximum).

$$\rho'(\theta_r)_{max} = \frac{2K\eta}{\Delta\theta}\sqrt{\frac{Ln\ 2}{\pi}} \qquad \text{(B-18)}$$

where the unity normalization still applies and η is the constant denoting an imperfect, real reflector; K is a normalization constant. This representation shows, that for $\eta = 1.0$, the peak value of the BDRD can be increased by narrowing $\Delta\theta$, which of course, corresponds to making the material under consideration more specular. Note however, that Equation (B-8) as written is in the wrong dimensions, since $\Delta\theta$ is the square root of a solid angle. Normalizing over 2π radians and reducing constants gives:

$$\rho'\ (\theta_r)_{max} = \frac{K\eta(.939)}{(2\pi)\Delta\theta} \qquad \text{(B-19)}$$

We must now solve for K with a surface whose reflectivity properties are known. Recall that for a perfectly diffuse object, $\rho'(\theta_r)$ is independent of θ_r, making it difficult to apply Equation (B-18). Instead a real material, pressed (fused ceramic) M_gO is used, which does exhibit a slight peaking in the BDRD response function. From Reference [B-4], it can be deduced that $\rho'_{max} = .325$, and the divergence, $\Delta\theta$, to those

points where $\rho'(\theta_r) = \frac{1}{2} \rho' (\theta_r)_{max}$ is 120°, and $\eta \simeq 1.0$. These parameters when used with Equation (B-17) results in

$$\rho'(\theta_r)_{max} = \frac{39.4\ \eta}{\Delta\theta}\ sr^{-1} \qquad \text{(B-20)}$$

Surface roughness must now be related to $\Delta\theta$ by using the measured data of Reference [B-5], which is shown in Figure B-3 plotted parametrically with κ. Ground glass coated with aluminum and ground nickel were used in the tests. At SRP less than 0.1 the angular beamspread is very small - a degree or less. For SRP greater than 0.25 the beamspread is very large indicating a diffuse subject. Between these values, the subject cannot be described specifically as diffuse or as specular.

For a surface roughness of 0.20 micron (noted earlier) and a wavelength of .3250 micron, the surface roughness parameter is:

$$\kappa = \frac{.20}{.3250} = .62 \qquad \text{(B-21)}$$

at a wavelength of .5500 micron,

$$\kappa = .36 \qquad \text{(B-22)}$$

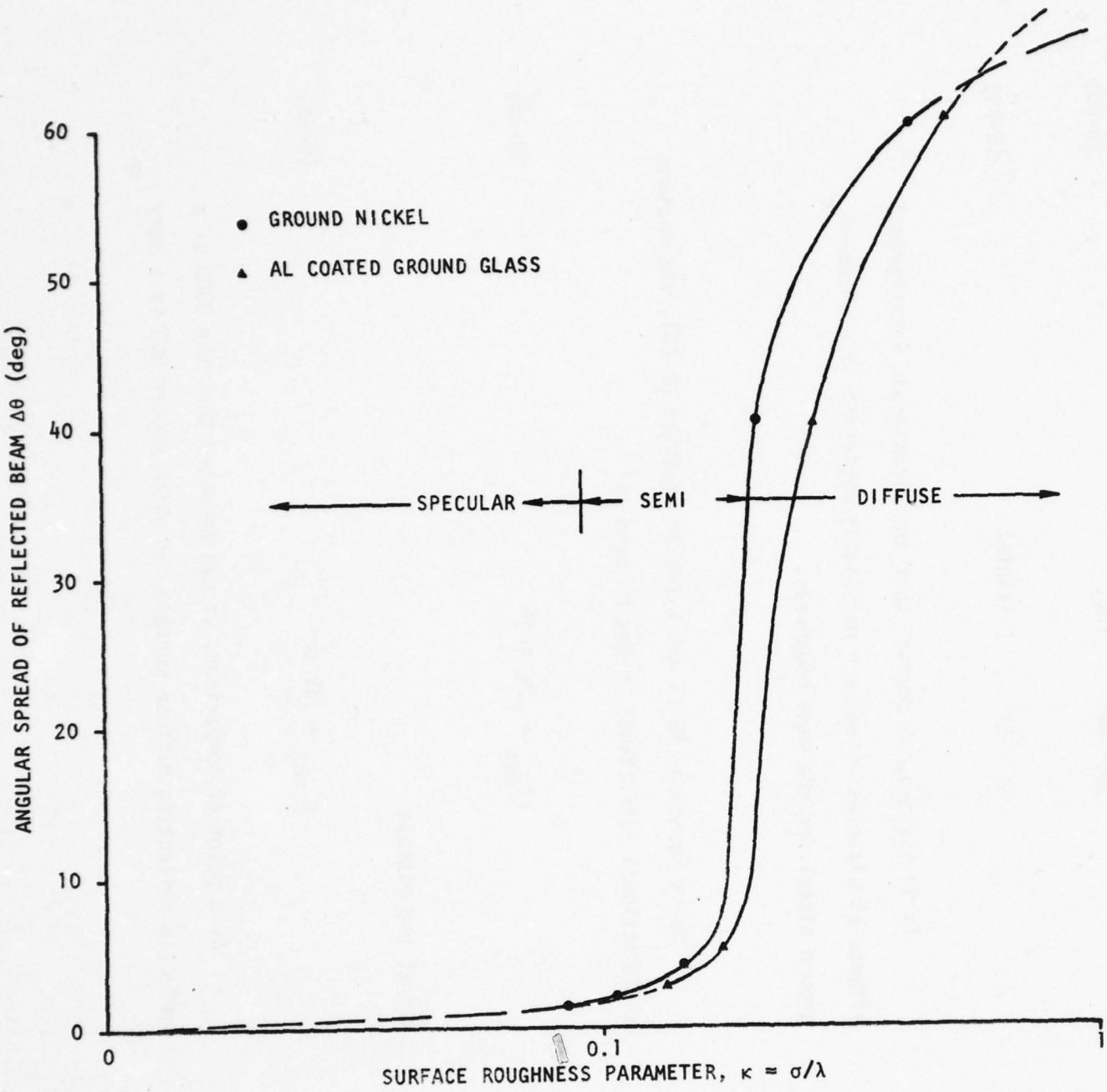

FIGURE B-3. VARIATIONS OF REFLECTING PROPERTIES WITH SURFACE ROUGHNESS

From Figure B-3, the beamspreads $\Delta\theta$ corresponding to Equations (B-21 and B-22) are respectively,

$$\Delta\theta = 62° \quad \text{(UV)} \tag{B-23}$$

$$\Delta\theta = 57° \quad \text{(visible)} \tag{B-24}$$

It is assumed, of course, that the microscopic (scattering) effects of stainless steel are not vastly different from those of ground nickel for the same roughness.

Using Equations (B-23 and B-24) in Equation (B-20), the maximum bi-directional reflectance in the UV band is:

$$\rho'_{max} = .26 \text{ sr}^{-1} \tag{B-25}$$

and at the visible.

$$\rho'_{max} = .39 \text{ sr}^{-1} \tag{B-26}$$

As a point of comparison, it can be noted that the BDRD of a perfectly reflecting diffuse surface, to which smoked MgO is a very

close approximation has a maximum and constant bi-directional reflectance of $1/\pi$. Recalling Equations (B-14)

$$t = \rho'\omega \tag{B-14}$$

The solid angle ω is just

$$\omega = \pi(\sin^2\theta) \approx \pi\theta^2 \tag{B-27}$$

where θ is the total plane angle subtended by the arc in the relay lens.

Thus,

$$\theta \approx \frac{\text{arc length}}{\text{focal length}} \tag{B-28}$$

If the arc completely fills the relay lens of one inch diameter, and the focal length is 8.7 inches,

$$\theta \approx .114 \tag{B-29}$$

and

$$\omega \cong .041 \tag{B-30}$$

Thus, from Equations (B-14) and (B-25)

$$t = .011$$

This result will be used in projector modeling, and in predicting performance of the proposed projector modifications.

B.5 DISCUSSION OF TARGET VANE DIFFUSER

The primary emphasis of the foregoing discussion has been an evaluation of the reflecting properties and radiation geometry of the metallic background vanes. A similar analysis could also be made for the ground glass diffuser in the target side. Here, the incident radiation is transmitted, then scattered, rather than reflected, but the gross effects of the surface roughness are certainly analogous.

There is incomplete data on the target condensor subsystem, which largely defines the incident radiation geometry, as well as on the diffuser itself. However, it is known that a single typical ground quartz diffuser, as might be available from a commercial source, has a beamspread, $\Delta\theta$, of about 20 degrees and a transmission of 75 percent.

From Equation (B-20), we can compute the maximum BDRD as

$$\rho'(\theta_r)_{max} = \frac{(39.)(.75)}{20} = 1.46 \text{ sr}^{-1} \qquad \text{(B-31)}$$

If it is supposed that the current target condensor system acts only as a "searchlight" to illuminate the vane diffuser, we can compute an approximate incident geometry. That is, by assuming that the source size is such, to create a characteristic dimension D, (Equation B-6b) that will just allow an inverse square falloff in illumination with distance. For a distance of 40 cm, and a condensor lens diameter of two inches

$$\sigma = .05 \text{ rad} \tag{B-32}$$

$$\omega \cong .00785 \text{ sr} \tag{B-33}$$

Thus, the vane transfer for the diffuser is the product of Equations (B-31) and (B-33)

$$t_{dif} = .011 \tag{B-34}$$

The exact agreement of Equation (B-34) with Equation (B-30) is probably fortuitous, but does indicate the same order of magnitude in radiance loss.

APPENDIX C

MIRROR ANALYSIS

C.1 OVERVIEW

The mirrors in the projector system, as well as those in the display opitcs, have a significant impact on total system radiance transfer: there are eleven mirrors in the system, and only a ten percent decrease in reflectance of each one from the ideal (R = 1.0) will create a factor of four system loss because of the power relationship of compounded reflectances. Thus, the mirrors were a prime suspect in any otherwise unexplained radiance loss, and a good estimate of their reflecting properties was deemed essential in systematic modeling of the present system.

According to the referenced data available (G.E. drawings), the mirrors are pyrex front surface aluminum with SiO (silicon monoxide) overcoat of unknown specifications. It is well documented, Reference [C-1], that the optical properties of vacuum-deposited SiO films can vary appreciably depending on the evaporation conditions imposed during film preparation. It has been established that the gas evolving from a mixture of Si + SiO_2 or from prepared silicon monoxide, at evaporation temperatures used for the deposition of films (1150°C to 1250°C), has the composition SiO. Most of the condensed films, however, show a

composition with more or less excess of oxygen and, therefore, optical properties which are more or less different from those of true SiO. The excess of oxygen is the result of both oxidation during the film condensation process and subsequent exposure to air. True SiO films can only be prepared by fast deposition (deposition rate $\geq 10^6$ Å/sec) under good vacuum conditions ($p \leq 1 \times 10^{-5}$ mm Hg). The foregoing conditions minimize the opportunity for oxidation while the material is being condensed and, furthermore, produce dense films which oxidize very little when exposed to air. If the silicon monoxide is deposited slowly (deposition rate ≤ 3Å/sec) in a poor vacuum ($p \sim 1 \times 10^{-4}$ mm Hg of air) a strongly oxidized incompact film results which has a high rate of oxidation when exposed to air, and more importantly, has a much higher ultraviolet transmission than pure silicon monoxide. This film has an average transmission between .30 and .40 μm of only 15 percent but greater than seventy percent between .40 and .70 μm. Thus, if a true SiO film were used, the ratio of system radiance transmission in the visible should have been orders of magnitude higher than in the ultraviolet because of the large number of mirrors. Additional system tests, as described in Section 5., indicated that the ratio of radiance transfer of the visible over the ultraviolet band was only a factor of two, a difference certainly not ascribable to the lower UV reflectances postulated considering the large number of mirrors. Thus, more subtle loss mechanisms were investigated, both by analysis and literature searches.

C.2 OPTICAL ANALYSIS

C.2.1 Formulation

The interference effects, or anti-interference effects, of dielectric coatings are reasonably well understood phenomena, and form the basis for a variety of optical applications, including the dielectric anti-reflecting (AR) coatings applied to many refractive optical components. This fact raised the question of what would be the effect of a non-absorbing dielectric coating deposited on metal: could interference effects account for a loss that was relatively wavelength independent? An analytical formulation of this phenomena is based on that of Born and Wolf Reference [C-2].

In Figure C-1 is shown a transparent dielectric film of index of refraction n_2 and thickness h between another dielectric (air) of index of refraction n_1 ($n_1 \tilde{\sim} 1.0$), and an absorbing metal of complex index of refraction $\hat{n}_3$:

$$\hat{n}_3 = n_3 - i\kappa_3 \qquad \text{(C-1)}$$

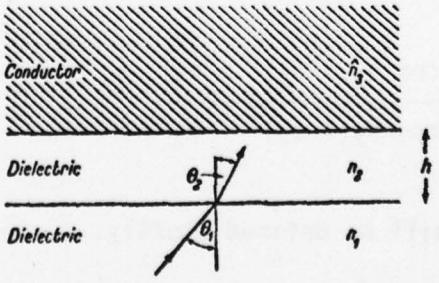

FIGURE C-1. DIELECTRIC ON ABSORBING SUBSTRATE

The reflectance R of this system for each plane of polarization is:

$$R_{11} = \frac{r_{12}^2 + \rho_{23}^2 + 2r_{12}\rho_{23}\cos(\phi_{23} + 2\beta)}{1 + r_{12}^2\rho_{23}^2 + 2r_{12}\rho_{23}\cos(\phi_{23} + 2\beta)} \qquad (C\text{-}2)$$

$$(\rho = \phi_{23} + 2\beta)$$

where the r's denote Fresnel amplitude reflectance at the air-dielectric interface, the ρ's at the dielectric-metal interface. The phase term includes ϕ_{23}, the change at the dielectric-metal interface, and 2β, the two-way phase change through the dielectric layer ($\beta = \frac{2\pi}{\lambda} n_2 h \cos\theta_2$). First the terms of Equation (C-2) are examined for the electric vector perpendicular to the plane of incidence.

The reflectance at the air-dielectric interface is

$$r_{12}^2 = \left[\frac{\cos\theta_1 - n_2\cos\theta_2}{\cos\theta_1 + n_2\cos\theta_2}\right]^2 \qquad (C\text{-}3)$$

where θ_2 is given by Snell's law.

The reflectance at the metal is

$$\rho_{23}^2 = \frac{(n_2\cos\theta_2 - u_3)^2 + v_3^2}{(n_2\cos\theta_2 + u_3)^2 + v_3^2} \qquad (C\text{-}4)$$

where the u_3 and v_3 will be defined shortly.

Similarly, for the parallel components:

$$r_{12}{}_{||}^{2} = \left[\frac{\cos\theta_2 - n_2\cos\theta_1}{\cos\theta_2 + n_2\cos\theta_1}\right]^2 \tag{C-5}$$

$$\rho_{23}{}_{||}^{2} = \frac{\left[n_3^2(1-\kappa_3^2)\cos\theta_2 + n_2u_3\right]^2 + \left[2n_3^2\kappa_3\cos\theta_2 - n_2v_3\right]^2}{\left[n_3^2(1-\kappa_3^2)\cos\theta_2 + n_2u_3\right]^2 + \left[2n_3^2\kappa_3\cos\theta_2 + n_2v_3\right]^2} \tag{C-6}$$

$$\left.\begin{aligned} 2u_3^2 &= n_3^2(1-\kappa_3^2) - n_2^2\sin^2\theta_2 + \sqrt{\left[n_3^2(1-\kappa_3^2) - n_2^2\sin^2\theta_2\right]^2 + 4n_3^4\kappa_3^2}, \\ 2v_3^2 &= -\left[n_3^2(1-\kappa_3^2) - n_2^2\sin^2\theta_2 + \sqrt{\left[n_3^2(1-\kappa_3^2) - n_2^2\sin^2\theta_2\right]^2 + 4n_3^4\kappa_3^2}\right] \end{aligned}\right\} \tag{C-7}$$

and for the phase shift terms at the dielectric:

$$\cos\beta = \text{arc}\left(\frac{2\pi}{\lambda}\, n_2\lambda\cos\theta_2\right) \tag{C-8}$$

$$\tan\phi_{23}{}_{||} = 2n_2n_3^2\cos\theta_2\,\frac{2\kappa_3u_3 - (1-\kappa_3^2)v_3}{n_3^4(1+\kappa_3^2)^2\cos^2\theta_2 - n_2^2(u_3^2+v_3^2)} \tag{C-9}$$

$$\tan \phi_{23} = \frac{2v_3 n_2 \cos \theta_2}{u_3^2 + v_3^2 - n_1^2 \cos^2 \theta_2} \qquad \text{(C-10)}$$

These last equations will next be employed with suitable optical data to solve Equation (C-2).

C.2.2 Optical Data

The index of refraction used for the dielectric (n_2) is from Reference [C-2], and is representative of SiO layers, exhibiting an increase at shorter wavelengths. The metal data is from Reference [C-3], with extrapolations of UV wavelengths. For the three wavelengths examined, the optical data is shown in Table C-1.

TABLE C-1. OPTICAL CONSTANTS

$\lambda(\mu m)$	n_2	n_3	κ_3
.3250	1.9	.28	3.3
.5500	1.7	.78	5.32
4.0	1.7	3.97	30.3

C.3 DATA COMPILATION

The solution of Equation (C-2) involves the prior, but systematic, solution of Equations (C-1 through C-10). This was accomplished by sequentially programming a SR-52 calculator for a small segment of the program, e.g., [Equation set (C-1)., for example], recording results, programming the next segment using data from the previous set, and so forth.

Some examples are shown in Table C-2, for the u's and v's, and ρ_{23}'s, as a function of θ_2, the angle of incidence *in the dielectric*.

C.4 RESULTS

Equation (C-2) was first solved by simply letting the phase term, cos γ, take on its maximum and minimum phase shifts, without regard for the origin. These are shown in Figures C-2, C-3 and C-4, for the ultraviolet, visible, and infrared spectral regions, respectively. These figures illustrate that interference effects do impact reflectance. Also, it is interesting to note the relative independence of the IR reflectance on the phase shift. This implies a relative insensitivity to dielectric thickness or index of refraction. The reflectance of each polarization component should be equal at normal incidence, if the phase term is adjusted.

TABLE C-2. SAMPLE CALCULATIONS

	λ = 3.250 μm n_2 = 1.9 n_3 = .28 κ_3 = 3.3				λ = .55 μm n_2 = 1.7 n_3 = .78 κ_3 = 5.32				λ = 4 μm n_2^2 = 1.7 n_3 = 3.97 κ_3 30.3			
θ_2 (deg)	u	$\rho_{23\|\|}$	v	ρ_{23}	u	ρ_{23}	v	$\rho_{23\perp}{}^2$	u	$\rho_{23\|\|}$	v	$\rho_{23\|\|}$
0	.28	.62	.924	.86	.78	.77	4.15	.72	3.97	.99	120	.99
20	.23	.59	1.11	.88	.77	.76	4.18	.72	3.96	.99	120	.99
30	.197	.60	1.31	.90	.76	.74	4.23	.72	3.97	.99	120	.99
45	.160	.68	1.61	.92	.75	.70	4.31	.73				
60	.138	.78	1.87	.93	.74	.66	4.40	.74				
75	.126	.88	2.03	.94	.73	.69	4.45	.74				
90	.123	1.00	2.09	.94	.72	1.0	4.47	.74				
	n_2= 2.5					n_2 = 2.1						
0	.28	.67	.924	.89	.78	.74	4.15	.74				
20	.20	.65	1.24	.92	.77	.73	4.20	.75				
30	.17	.69	1.53	.94	.76	.71	4.28	.75				
45	.13	.77	1.97	.95	.74	.67	4.4	.76				
60	.11	.85	2.34	.96	.72	.65	4.52	.77				
75	.10	.92	2.57	.96	.70	.71	4.60	.77				
90	.09	1.0	2.65	.96	.69	1.0	4.64	.78				
	n_2 = 1.5					n_2 = 1.3						
0	.28	.58	.924	.83	.78	.81	4.15	.69				
30	.22	.55	1.17	.87	.77	.79	4.20	.70				
45	.19	.60	1.37	.89	.76	.75	4.25	.70				
80	.16	.70	1.57	.90	.75	.70	4.29	.71				
90	.15	1.0	1.75	.91	.75	1.0	4.34	.71				

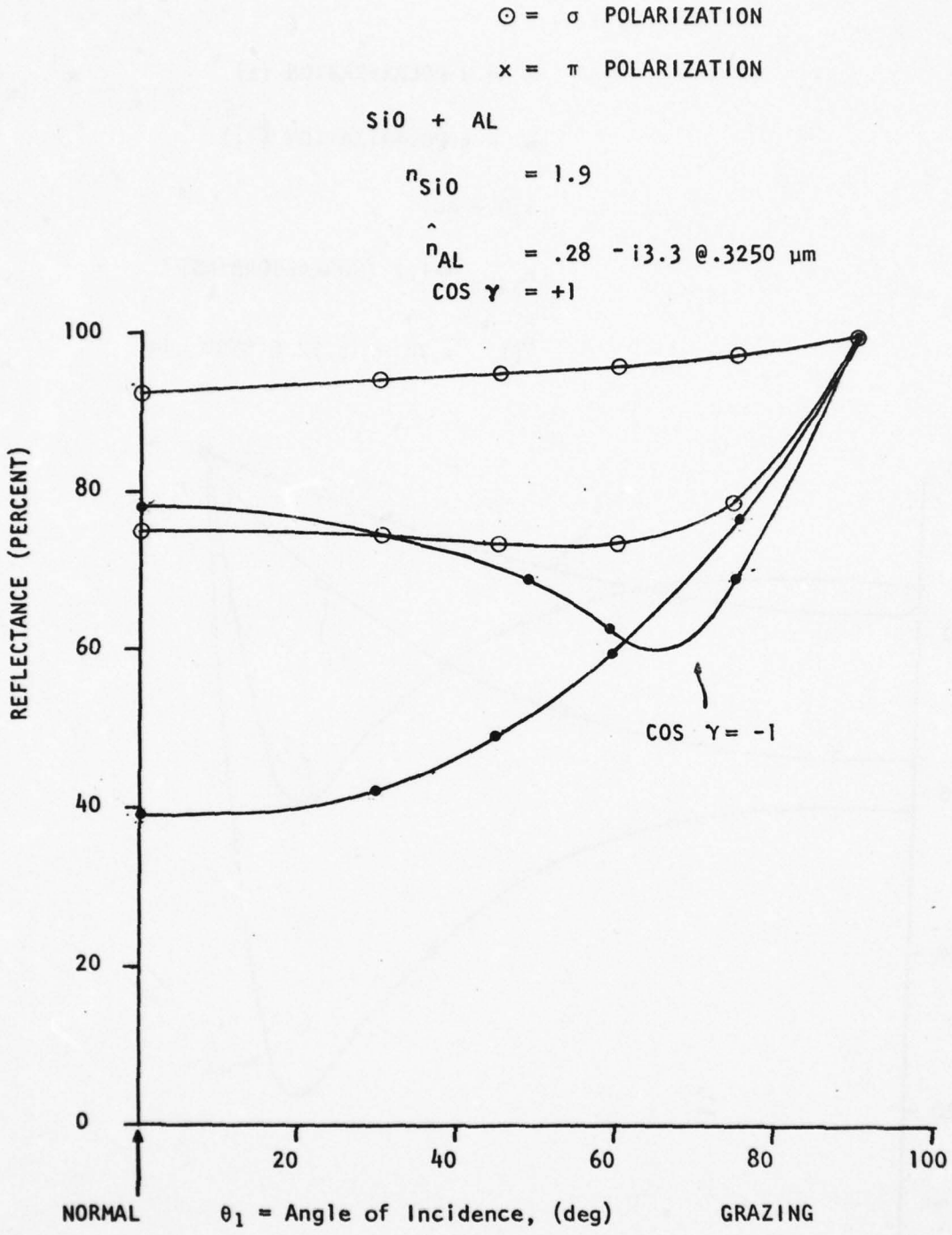

FIGURE C-2. REFLECTANCE IN THE ULTRAVIOLET

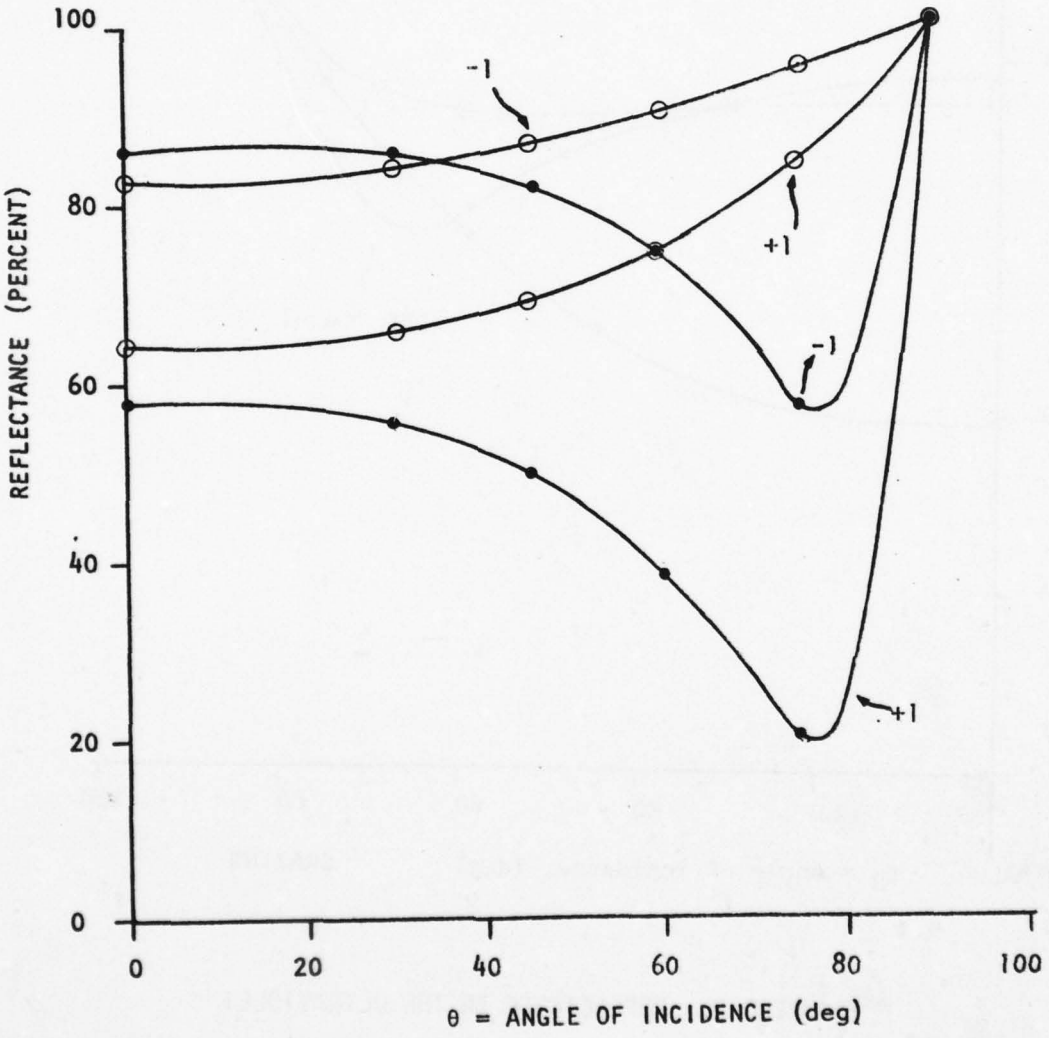

FIGURE C-3. REFLECTANCE IN THE VISIBLE

SiO + AL

n_{SiO} = 1.71

$\hat{n}_{AL}$ = 5.97 - i 30.3
(From SCHULTZ)

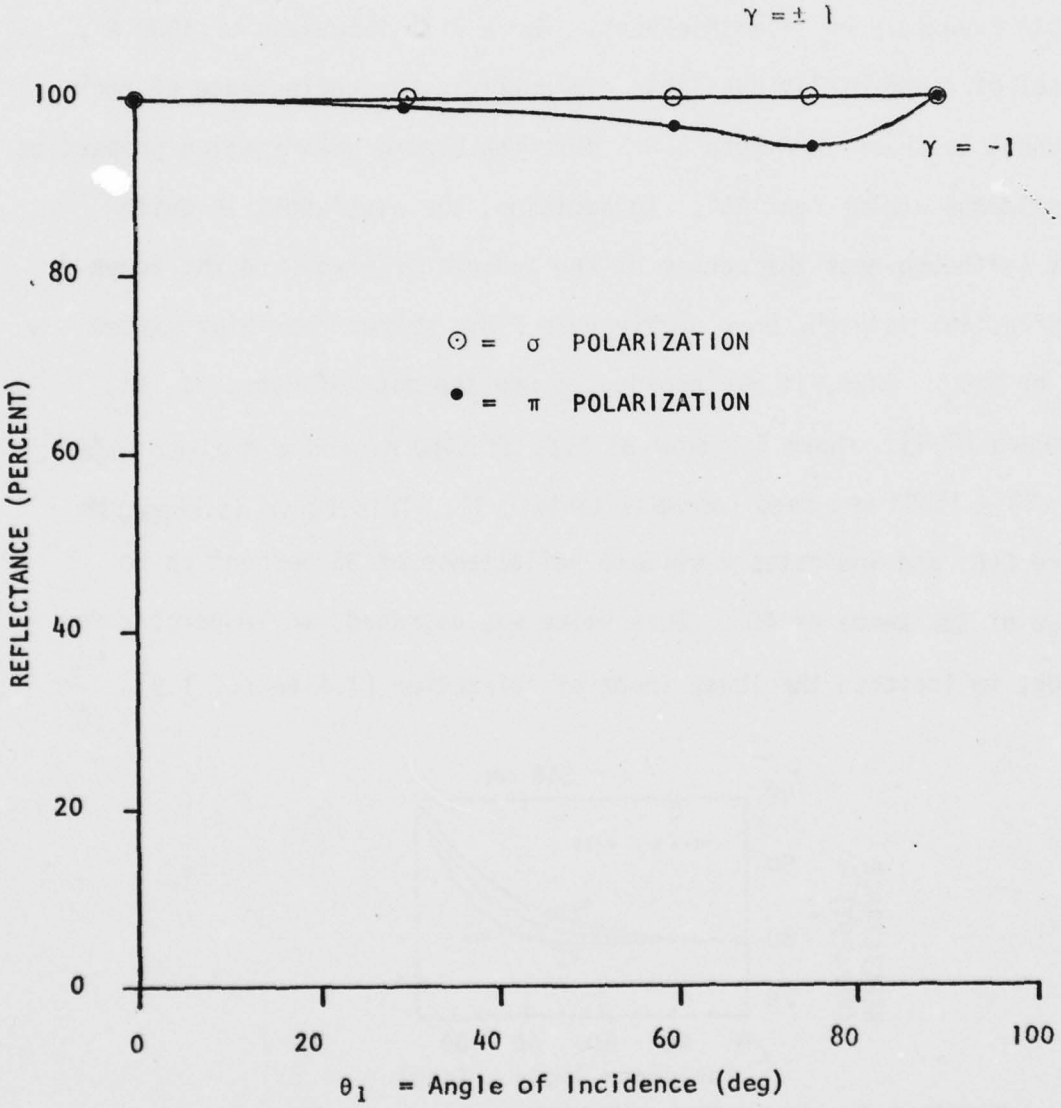

FIGURE C-4. REFLECTANCE IN THE INFRARED

Examination of Equation (C-8) reveals that the phase change through the dielectric is a strong function of film thickness at a given index of refraction. A thickness change of only $\sim$ 800 Å changes the dielectric phase shift by 180°, in the UV and visible. For the IR spectrum, thickness changes of 500 Å change the phase shift by only a few degrees. This implies a strong dependence of reflectance at a visible frequency on film thickness. For a film thickness of 1500 Å, typical of commercially available dielectrics, the reflectance of each component is shown in Figure C-5. Note the strong polarization properties at incidence angles near 45°. In addition, the wavelength is quite short (although near the center of the radiometer band) and the index of refraction is high, more nearly pure SiO), rather than high oxygen SiO_2 or SiO_x. Thus, it was decided to use the data of Haas, et. al. Reference [C-4], where an index of 1.6, at 5460 Å, and a complex index $\hat{n}$ = .83 - i5.99 was used (compare Table C-1). This curve is shown in Figure C-6, and indicates a visible reflectance of 83 percent up to angles of incidence of 45°. This value was degraded, to 78 percent for the UV, to indicate the lower index of refraction (1.6 versus 1.9).

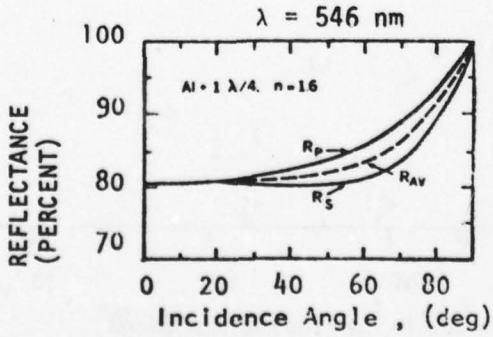

FIGURE C-6. CALCULATED REFLECTANCE OF Al AND TYPICAL NONABSORBING SURFACE FILMS AS A FUNCTION OF INCIDENCE ANGLE AT λ = 546 nm

SiO THICKNESS = 1500 Å

SiO INDEX = 1.9 @ 3200 Å

AL INDEX = .28 - i 3.3

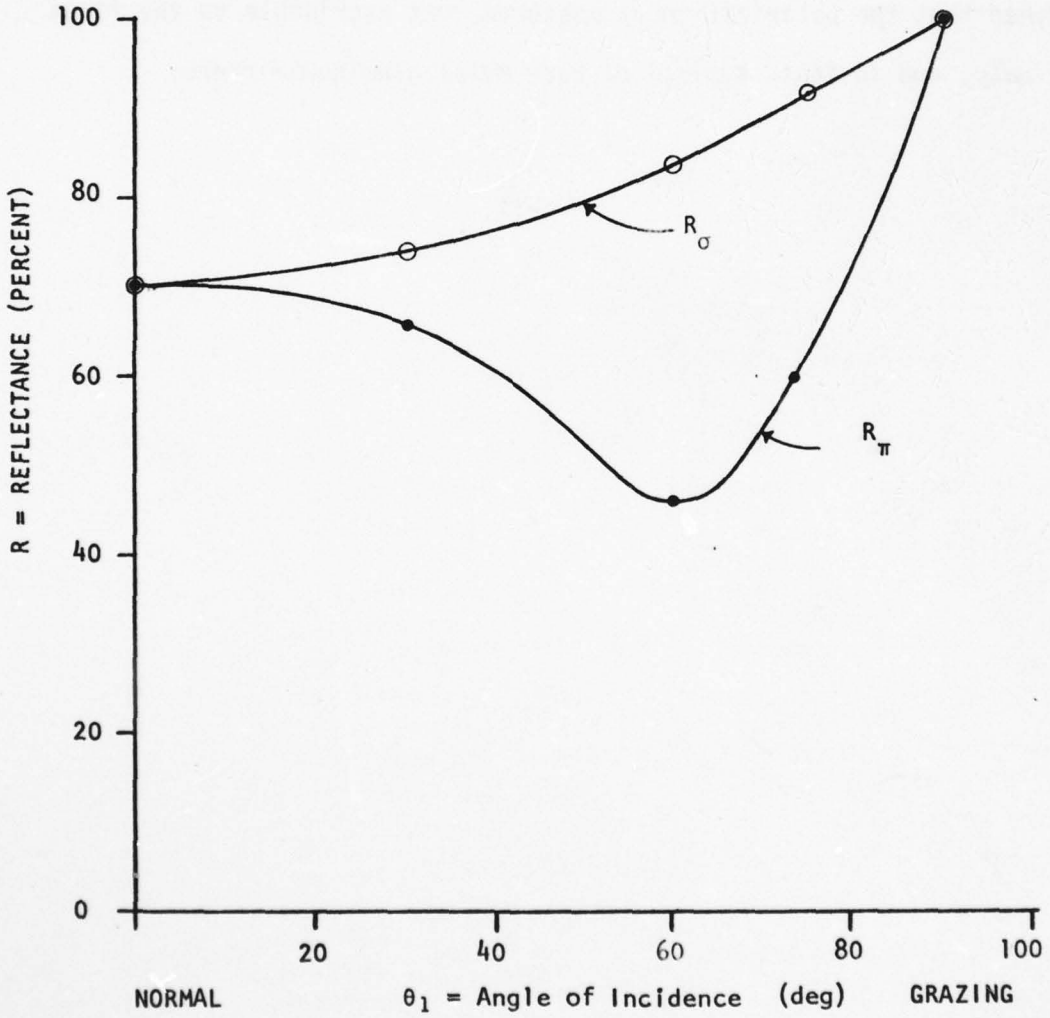

FIGURE C-5. CALCULATED ULTRAVIOLET REFLECTANCE FOR Al-S_iO MIRROR

This trend shown in Figure C-5 appeared to closely match the polarization test results, when the light reflected from the first mirror was very strongly polarized (see Figure 5-13), and an analysis was performed on total system radiance transfer by separately calculating the transfer of each polarization state, assuming all 45 degree mirrors in the system, including display optics, behave similarly. After some discussion with mirror vendors, and a further survey of literature, it was determined that the polarization as measured, was ascribable to the first mirror *only*, and in fact, typical of base metal aluminum mirrors.

APPENDIX D

MODIFICATION OF THE FLARE PROJECTOR

This appendix describes a preliminary examination of the IRSS infrared flare projector undertaken to extend operation of the projector into the near ultraviolet. Subsection D.1 describes the present status of the flare projector's optical train. A lack of information regarding the projection lens and its anti-reflection coatings prevents detailed calculations from being made. Subsection D.2 describes possible modifications to the present flare projector optics which should provide the required near-ultraviolet output.

D.1 IR FLARE PROJECTOR-PRESENT STATUS

Figure D-1 illustrates the optical elements presently comprising the IRSS flare projector. The Varian 500W xenon lamp (VIX-500) consists of a high-pressure, short-arc xenon illuminator, a parabolic collimating reflector, and a sapphire output window, and serves as a high-intensity source of broad-band radiation from the UV to IR regions of the electromagnetic spectrum. A sapphire condensing lens 5.7 cm in diameter (clear aperture 5.1 cm) with a thickness of 0.53 cm on the optical axis has both sides anti-reflection coated to optimize transmission in the 1.5 μ region. Next, a high-pass filter (> 1μ) reflects UV and visible radiation onto a CdS photocell to provide a feedback mechanism for lamp stability. Details

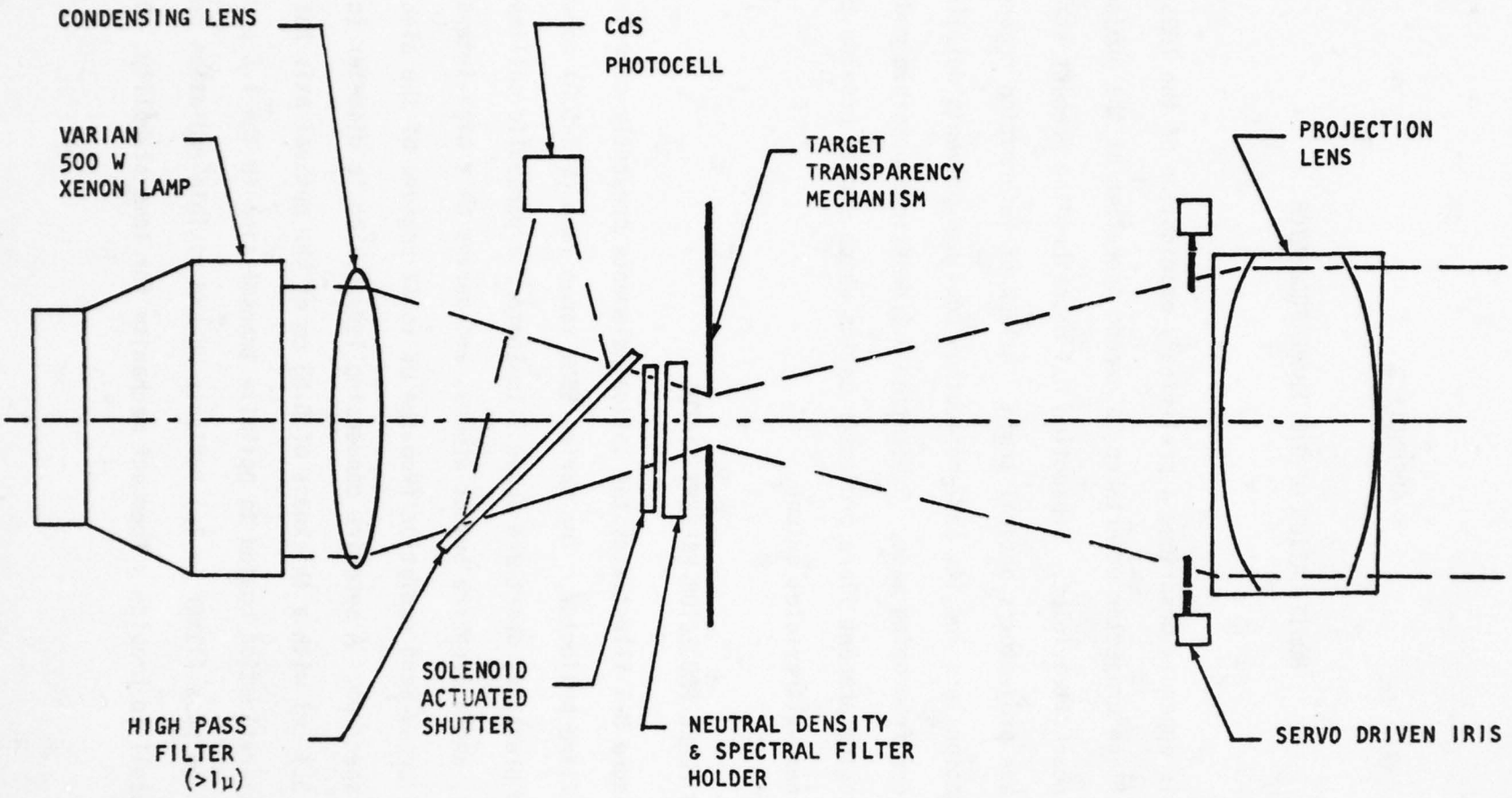

FIGURE D-1. TAILPIPE/FLARE PROJECTOR

of the filter design are unavailable, but a report by Broomer Research Corporation indicates that filter transmission below one micrometer is less than one percent and that above one micrometer the average transmittance exceeds 70 percent. A solenoid-activated shutter, neutral-density and spectral filter holder, and target-transparency mechanism follow the high-pass filter. Finally, a servo-driven iris immediately precedes a 6.3 cm diameter (4.6 cm clear aperture) projection lens with a focal length of 19 cm and a thickness along the optical axis of approximately 2.5 cm. Details of the projection lens design are not available. Apparently the projection lens consists of three elements with the exterior elements composed of calcium fluoride, CaF_2. This assumption is based on recommendations of the Phase 1 Final Report, July 1971, Reference [3-1], and the warning on page 26-19 of the IRSS Operation and Maintenance Manual, April, 1973, Reference [D-1]. Unfortunately, the optical material in the third element is not known with any certainty. The Phase 1 Final Report indicates arsenic trisulfide, As_2S_3, as the proposed material. However, Mr. Harry Vandermeer, one of the lens designers with Diffraction Limited (which produced the lens), has indicated that arsenic trisulfide was not in use by the company at that time. He believes that sapphire was employed in the central element, but the details of the lens design and anti-reflection coatings applied are apparently unavailable. Due to the significant differences in the ultra-violet transmittances of sapphire and arsenic trisulfide, as shown in Figure D-2, this uncertainty will have significant bearing on the modifications required.

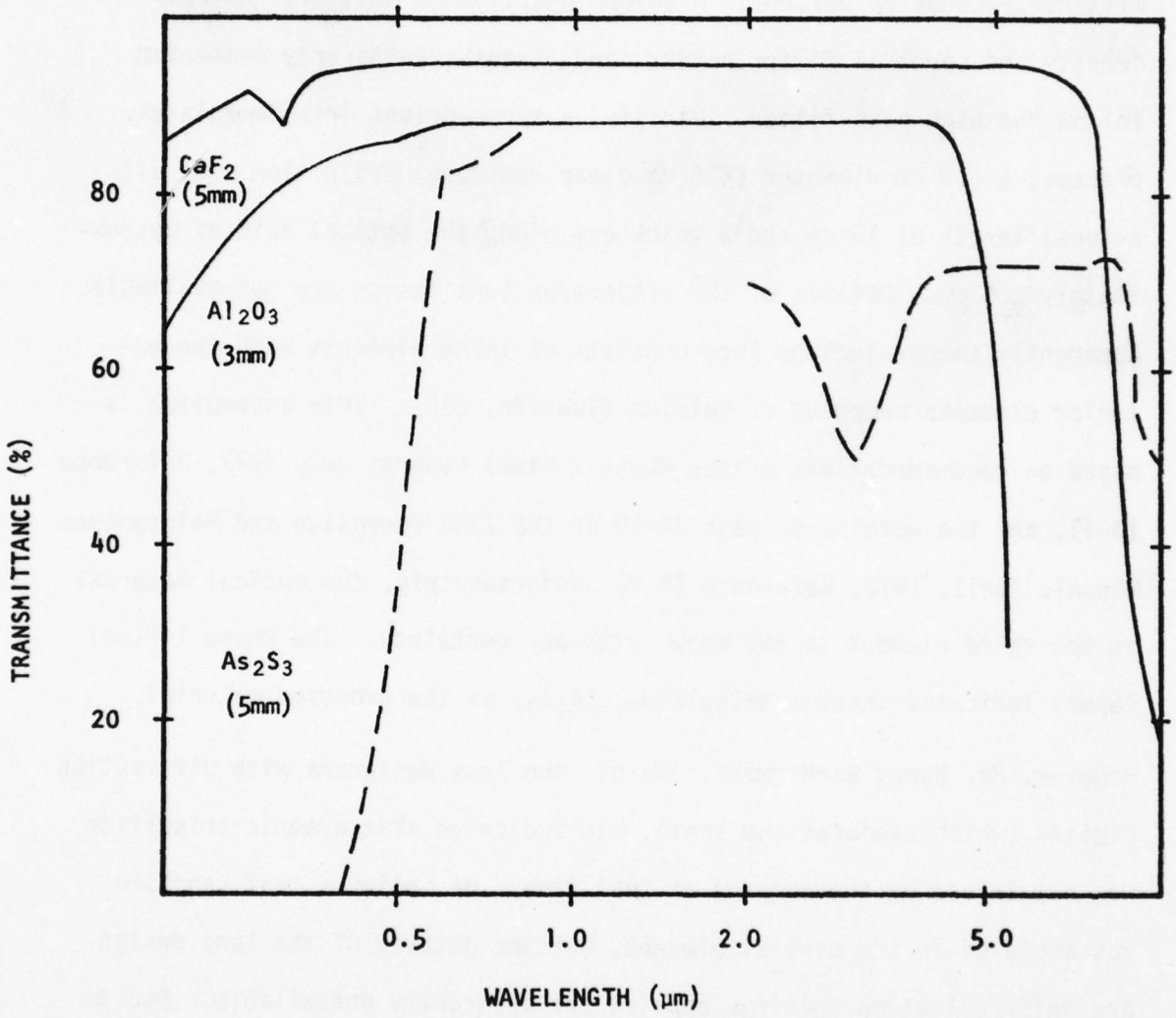

FIGURE D-2. EXTERNAL TRANSMITTANCES OF CALCIUM FLUORIDE (CaF_2), SAPPHIRE (Al_2O_3), AND ARSENIC TRISULFIDE (As_2S_3)

The balance of the IRSS optical train is of interest in this appendix only due to the need to relate display window requirements to lamp output (no modifications to these components is considered in this appendix). Between the projection lens and the display window are nine (9) aluminum mirrors with SiO protective coatings. The reflectance of freshly evaporated aluminum-coated mirrors is shown in Figure D-3. The reflectance of the mirrors employed in the IRSS may vary somewhat from this curve depending on the thickness and conditions of preparation of the SiO coating (See appendix C). A dimpled mirror provides an expansion of the pupil from the projector diameter of 4.6 cm to the diameter required for display purposes, 29.6 cm.

Table D-1 provides opacity (inverse of transmittance) estimates of each component in the projector system and of the components in the subsequent IRSS optical system. The opacities are provided in two wavebands, 0.35 - 0.40 μm and 3.8 - 4.6 μm. Since decisions regarding projector modifications will strongly depend on these opacity estimates, an explanation of how these values were obtained is in order.

The external transmittance of a 3 mm thick sapphire crystal is shown in Figure D-2. This transmittance includes approximately a 10 percent Fresnel reflection loss at the surface. Correcting for this loss, the internal transmittance through the material is $\sim$ 94 percent in the UV (0.35 - 0.40 μm) and $\sim$ 96 percent in the IR (3.8 - 4.6 μm). This indicates absorption coefficients of 0.206 cm^{-1} and 0.136 cm^{-1} in the

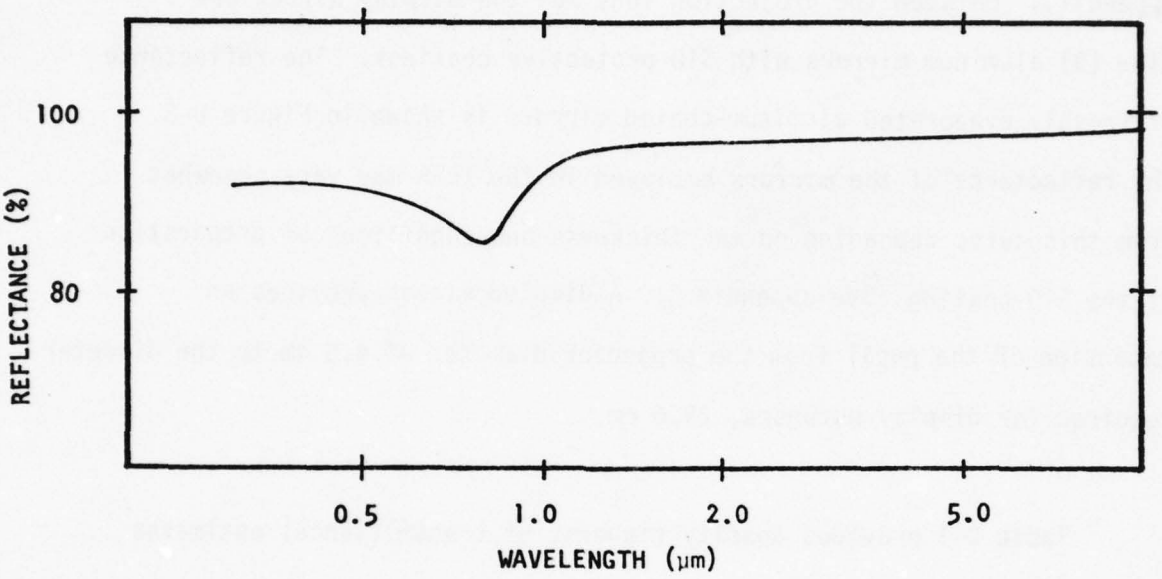

FIGURE D-3. REFLECTANCE OF ALUMINUM COATED MIRROR

TABLE D-1. IRSS FLARE PROJECTOR COMPONENT OPACITIES

	ELEMENT	ELEMENT OPACITY	
		(UV (0.35 -.40 μm)	IR (3.8 - 4.6 μm)
FLARE PROJECTOR	CONDENSER LENS (UNCOATED)	1.25	1.20
	HIGH-PASS FILTER	100	1.43
	SOLENOID ACTUATED SHUTTER	1.0 (OPEN)	1.0 (OPEN)
	NEUTRAL DENSITY 8 SPECTRAL FILTER HOLDER	1.0 (EMPTY)	1.0 (EMPTY)
	SERVO DRIVEN IRIS	1.0 (FULLY OPEN)	1.0 (FULLY OPEN)
	PROJECTION LENS	1.46 (SAPPHIRE)	120 (MEASURED)
		100 + (ARSENIC TRI-SULFIDE)	
IRSS DISPLAY OPTICS	ALUMINUM COATED MIRRORS (9 in all)	9.38	1.32
	DIMPLED MIRROR	41	41
TOTAL OPACITY	SAPPHIRE	71,000	112
	ARSENIC TRISULFIDE	4.9×10^6	

UV and IR, respectively. The internal transmittance of a 0.53 cm thick segment of sapphire (the condenser lens thickness) becomes 90 percent in the UV and 93 percent in the IR. Correcting for the reflectance losses gives uncoated condenser lens transmittances of 80 percent in the UV and 83 percent in the IR, or opacities of 1.25 and 1.20, respectively, as indicated in Table D-1. With the anti-reflection (AR) coating specified for the condenser lens, the IR transmittance (3.8-4.6 μm) is probably close to 93 percent (i.e., negligible reflection losses) while the UV transmittance (0.35 - 0.40 μm) is probably somewhat less than 80 percent. The application of an AR coating to improve transmission in one spectral interval will almost invariably impair transmission outside that interval. Without details of the AR coating, it is ill-advised to try to estimate its effect on the UV transmittance of the condenser lens except to note that it may be severe. For the purposes of this appendix the AR coatings will be ignored.

The high-pass filter opacities result from the assumption that the filter transmittances above and below one micrometer are 70 percent and one percent, respectively. The solenoid activated shutter, neutral-density and spectral filter holder, and servo driven iris are, in effect, ignored by assuming benign conditions (shutter open, no neutral density filter in place, etc.)

The projection lens is treated in a manner similar to the condenser lens with the added complication that the thickness of the three elements are unknown and alternative calculations for both sapphire and arsenic trisulfide are necessary in the ultraviolet (the infrared transmittance was measured). Each element is assumed to be one third of the total lens thickness and, as with the condenser lens, AR coatings are ignored. While both sapphire and arsenic trisulfide are viable infrared optical materials, it is clear that if the projection lens contains arsenic trisulfide, the lens is unsuitable for use in the near ultraviolet. Since the IRSS display optical train requires nine (9) separate reflections, the total reflectance of the display system is $(0.97)^9$ or 76 percent in the infrared and $(0.78)^9$ or 11 percent in the ultraviolet. An ultraviolet reflectance of 78 percent is chosen as being typical of a mirror which has experienced some deteriation due to aging. The equivalent opacities are 1.32 and 9.36, respectively, as shown in Table D-1. The opacity assigned to the dimpled mirror results from the increase in solid angle it provides. The opacity is given by the square of the ratio of the pupil diameter at the display window to that provided by the projector, $\left(\frac{29.6}{4.6}\right)^2 = 41.$ The total system opacities are shown in Table D-1 and indicate the factors by which lamp output must exceed display window requirements.

Table D-2 indicates the estimated lamp radiance available from the VIX 500 Varian Xenon lamp and the maximum required target radiance in the display window. The lamp output in the IR(3.8μ - 4.6 μm) is estimated from measurements made in the IRSS display window and subsequently, adjusted by the IR system opacity. Two estimates of target requirements are

TABLE D-2. IRSS ESTIMATED PERMISSABLE OPACITY

	APPROXIMATE OUTPUT VIX 500 VARIAN XENON LAMP ($Wcm^{-2}\ sr^{-1}$)	MAXIMUM REQUIRED TARGET DISPLAY RADIANCE ($Wcm^{-2}sr^{-1}$)	TOTAL PERMISSABLE SYSTEM OPACITY
IR (3.8 - 4.6 μm)	4.9 APPROX	1.63 (2000 K BLACKBODY)	3.0
		APPROX. 0.05 (10 TIMES ANY TARGET)	98
UV (0.35 - 0.40 μm)	24.0	0.0042 (2000 K BLACKBODY)	5700

shown in the table. The first is more stringent and stipulates that the target resemble a 2000 K blackbody. The total permissable system opacity, given this requirement would be 3.0-clearly incompatible with the IRSS system opacity estimates presented in Table D-1. The less stringent requirement is that the flare projector target radiance exceed other target radiances by a factor of ten. The permissable system opacity is then $\sim$ 100, which is nearly compatible with the system opacity estimates of Table D-1. Apparently, the present IRSS flare projector can meet this less stringent requirement.

Lamp radiance in the ultraviolet (0.35 - 0.40 μm) is calculated from information contained in the Varian brochure supplied with the lamp. Ultraviolet target radiance from the various IRSS projectors is difficult to estimate without more information regarding the various projector opacities in the UV than is readily available. As a result, only the 2000 K blackbody requirement is considered. A maximum permissable system opacity in the UV of 5700 is estimated. In considering lamp output in the ultraviolet, it should be noted that tailpipe temperatures from realistic targets may be expected to exceed 1800 K. As a result, the ultraviolet radiance of the tailpipe may differ only slightly from the flare radiance (2000 K). Since the flare and tailpipe projectors are identical, modifications to achieve sufficient ultraviolet throughput may be necessary for both projectors - not the flare projector alone.

D.2 IR FLARE PROJECTOR - MODIFICATIONS

Comparing the total permissable UV system opacity of 5700 with the various estimated opacities in Table D-1, it is apparent that if the projection lens contains arsenic trisulfide, it will have to be replaced. If, however, the projection lens is composed of calcium fluoride and sapphire, it may be possible to retain the projection lens. In this event, the only modification required of the projector system may be the removal or modification of the high-pass filter. Dynetics' best estimate is that removal of the high pass filter from the flare projector will provide sufficient throughput in the ultraviolet between 0.35 μm and 0.40 μm to simulate a 2000 K flare. If the lamp monitoring feedback loop provided by the high-pass filter and CdS photocell is indispensable, a multilayer filter with high reflectivity in the visible and near IR could be designed and substituted for the high-pass filter presently in use.

A second factor, other than throughput, which will affect the extension of the flare projector into the UV is the image quality obtainable from optics designed for use in the IR. Without more information regarding the refractive elements in the projector than is now available, it is not possible to undertake detailed ray trace calculations to determine the ultraviolet optical aberrations of the present system. An estimate of the image blur size, B, for the projection lens due to chromatic aberration is obtainable from

$$\beta \propto V^{-1} (f/no)^{-1} \qquad \text{(D-1)}$$

where the f-number (f/no) is the focal length divided by the clear aperture and V is the Abbe value obtained from the variation of the index of refraction with wavelength. Table D-3 gives the Abbe V value for both calcium fluoride and sapphire in the UV and IR wavebands. Since the f-number for the two wavebands is nearly equal, the chromatic aberration will vary inversely with the Abbe value. This would indicate that the angular blur due to chromatic aberration in the ultraviolet waveband would be less than in the infrared waveband. This is at best a crude estimate which ignores the element configurations of the projection lens which were undoubtedly designed to minimize chromatic aberration in the near IR. Furthermore, the other primary aberrations vary with wavelength and it is doubtful that a balancing of these aberrations in the near IR will be maintained in the near UV. A visual

TABLE D-3. ABBE V NUMBERS FOR TWO OPTICAL MATERIALS IN THE UV AND IR

MATERIAL	UV (0.35 - 0.40 μm)	IR (3.8 - 4.6 μm)
CALCIUM FLUORIDE	94	52
SAPPHIRE	72	17

inspection of the display window image with only the flare projector turned on suggests that image quality remains rather good to at least near 0.4 μm. This is reassuring in that it suggests that the projector optics, although designed for use between one and five microns, may provide adequate image quality in the near ultraviolet. Visual observations fall within a spectral interval beginning just above the proposed UV waveband in a region where arsenic trisulfide maintains adequate transmittance. Thus, visual checks alone cannot eliminate the possibility that arsenic trisulfide is present in the projection lens.

In conclusion, it would appear that the simple expedient of removing or replacing the high-pass filter should satisfy the throughput requirements for operating the IRSS flare projector in the near ultraviolet between 0.35 and 0.40 μm provided the projection lens is, in fact, composed of calcium fluoride and sapphire, and any AR coating is non-absorbing in the UV waveband. If the projection lens contains arsenic trisulfide, it will have to be replaced also. It is recommended that transmission curves for the projection lens be obtained in the visible and near UV regions of the spectrum prior to any further study of flare projector modification.

APPENDIX E

ALTERNATE CONCEPTS

E.1 BACKGROUND

In Section 7. of this report is included a description of the recommended design concept for the modification to the UV/visible projector system. That design, based principally on component changes, is expected to perform at all required levels. However, other designs assuming totally different concepts, have been pursued during the course of the study. One of these concepts is based on the principles of Fourier optics and utilizes high technology components.

E.2 LASER SOURCES

Two general classes of laser sources were evaluated during the study: the noble gas ion laser for ultraviolet wavelengths, and the chemical laser at mid-IR wavelengths. Many other types of lasers have been designed to operate in both these frequency bands, but we have restricted our evaluation to CW (continuous wave), commercially available units. Furthermore, the emphasis has been placed on these lasers with total output power in the TEM_{00} mode of $\geq$ 1.0 watt, since a preliminary analysis indicated that lasers of lower power, irrespective of their beam patterns, would be inadequate considering the high losses in the display optics.

Lasers were evaluated with respect to the following applications:

(1) replacement of current UV and/or IR incoherent xenon sources with system configuration unchanged except for adapting, (i.e., beam expansion and shaping) optics.

(2) Use in advanced, high technology system concepts to be described presently, but still limited to systems fulfilling the present functional requirements.

(3) Conceptual basis for new systems that attempt to simulate additional functions, such as modulated jammer IR/CM, but based on "conventional" optical design.

Each of the two classes of lasers will now be discussed relative to these applications.

E.2.1 Chemical Laser

Although there undoubtedly exist other working models, there is only one chemical laser available off-the-shelf. This laser is manufactured by Helios, Inc. of Longmont, Colorado, and is an electrically driven Hydrogen Fluoride (HF) and Deuterium Fluoride (DF) device available in three size (power) ranges.

HF/DF chemical lasers are based on the reaction of fluorine atoms with hydrogen or deuterium, $F + H_2/D_2 \rightarrow HF^*/DF^* + H/D$, the so-called

pumping reaction. Several types of lasers have been developed, differing in principle only in the means used to generate the F-atoms, and in the details of the fluid flow system which fuels the pumping reaction in the laser cavity. The electrically-driven HF/DF chemical laser is preferred for most low to medium power applications due to operational simplicity and no requirement for gases such as F_2 or NF_3. The operation of an electrically-driven cw HF/DF chemical laser can be described as follows: a discharge is sustained by a high voltage power supply in a gas mixture containing a fluorine compound which is partially dissociated to produce F-atoms; H_2 or D_2 is injected and rapidly mixed with the F-atoms in a suitable channel coupled to an optical cavity; the pumping reaction and lasing occur in the optical cavity, and the spent gasses are exhausted by a vacuum pump. Being an open-cycle flow device, the laser will deliver output power approximately proportional to the capacities of the power supply and vacuum pump used.

The laser will operate with either HF or DF as the lasing species and in either multiline or, with optional grating coupler, in single line operation. The wavelength range is from 2.58 to 3.05 μm(HF) and 3.58 to 4.05 μm(DF). The available power between 3.8 and 4.6 μm is about two-thirds of the total (3.58 to 4.05) with about thirteen rotational transitions in simultaneous oscillation. The medium power laser available from Helios is capable of approximately 2 watts between 3.8 and 4.6 μm over all lines; if single line operation is required, the highest-power transition $P_2(3)_{10}$ line is capable of 300 mW.

A basic diagram is shown in Figure E-1. Not shown are the water cooling lines necessary to cool the laser head. A picture is shown in Figure E-2. The laser head includes the cavity, mirrors and their mounts, Brewster windows and optional accessories, such as the grating coupler.

This laser offers significant advantages over competitive sources in certain respects, such as adaptability and efficiency. However, the cumbersome physical relationship of the auxilliary equipment, such as the vacuum, gas, HV, and water coolant lines to the laser head and discharge tube would make practical adoption to the IRSS difficult. The price, including head, discharge tube, gas control, power supply and vacuum pump of this system is over $25000 for the intermediate power model.

None of the applications mentioned previously would benefit directly from one of the lasers.

E.2.2 Ion Laser

The ion laser is typified, at least in its practical and commercial aspects, by the Argon or Krypton types. These are available from at least four different vendors: Coherent, Holobeam, Spectra Physics, and Lexel. These devices utilize high current electrical excitation, and off-the-shelf lasers are available with power up 2.0 watts with Kryton (.3564 and .3507 μm) and 2.5 watts with Argon (.3511 and .3638 μm) in

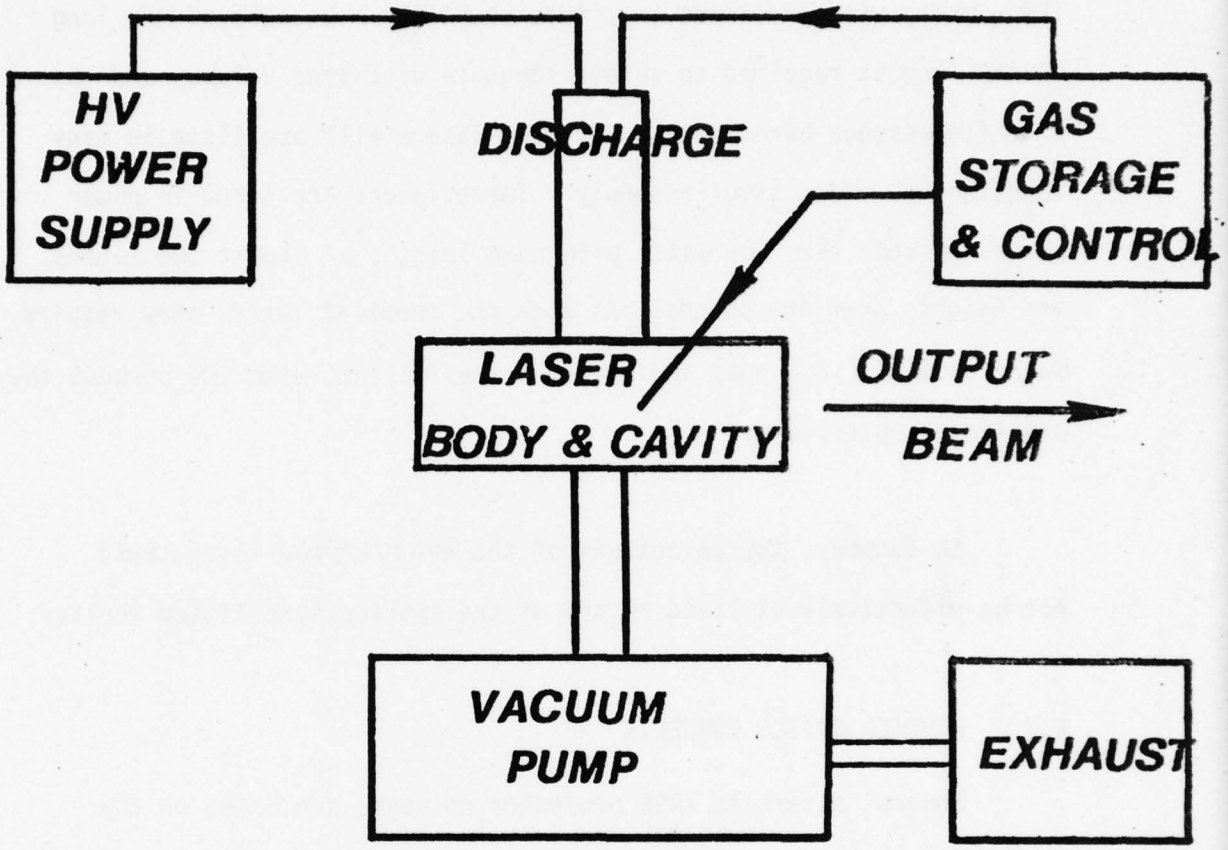

FIGURE E-1. DEVICE OPERATION

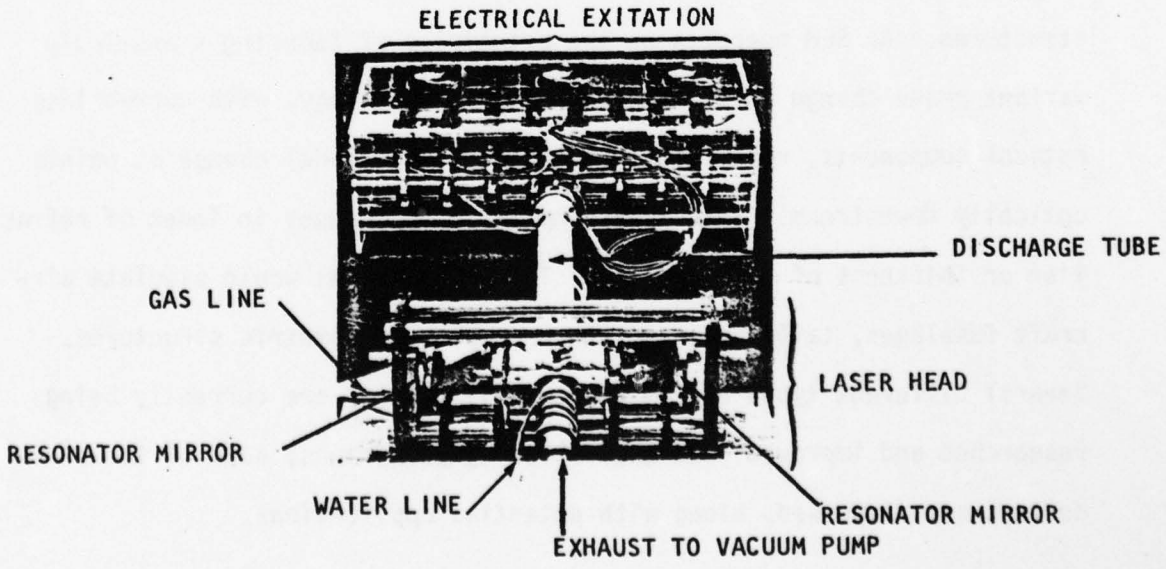

FIGURE E-2. HF - DF LASER

TEM_{00} mode, with excellent amplitude stability. Because of the long cavity lengths required to obtain adequate discharge volume, and the wide fluoresence bandwidth (5 GHz) the lasers will oscillate in many longitudinal modes simultaneously. These lasers are large in power ranges greater than one watt, with head lengths of almost two meters, and weights over 400 pounds. As with the chemical laser, they require water cooling ($\sim$3.5 gpm) and are very inefficient, with .01 percent the practical upper bound.

In summary, the advantages of the agron/kryton laser could not be effectively utilized in any of the applications listed earlier.

E.3 FOURIER OPTICS CONCEPTS

Several alternate IRSS projector concepts are based on the principles of Fourier optics and may include a spatial light modulator (SLM) and an associated optical system to produce images of complex structures. An SLM operates on the principles of inducing a *spatially* variant phase change in a beam of radiation which may, with appropriate optical components, result in an intensity (amplitude) change at points optically downstream. This is accomplished by changes in index of refraction or thickness of the material. These structures would simulate aircraft fuselages, tailpipes, and other complex radiometric structures. Several different types of SLM's are available and are currently being researched and improved. In the following paragraphs, some of these devices are discussed, along with potential applications.

One commercially available SLM is the electron beam on dielectric film type. Figure E-3 illustrates one method of utilizing the dielectric oil SLM in the fashion described above. A scanning electron beam is modulated by the input data (representing the image desired) to place a spatial charge distribution on the dielectric oil. This charge distribution changes the thickness of the oil film to produce phase delays in the incident light transmitted through the SLM. A resolution of over 500 units by 500 units across the oil film surface is currently available at a frame rate of 30 per second.

The phase pattern impressed on the oil film is erased when the spatial charge distribution decays. Limitations associated with this erase mechanism and other problems relating to this type of SLM, such as oil flatness, are still under study at the present time.

In Figure E-3, the SLM is placed in front focal plane P_1 of lens L_1, and, under the proper conditions, the Fourier transform of the field transmitted by the LSM is produced in the rear focal plane P_2. Lens L_2 then takes the inverse Fourier transform of the spatial frequency components of plane P_2 . The output image is produced in plane P_3 . The output in P_3 can be manipulated by performing spatial filtering in P_2.

The phase delays introduced by the SLM will diffract components of the incident light. The Fourier specturm of the SLM input will be formed off-axis in P_2 while the undiffracted background components are focused

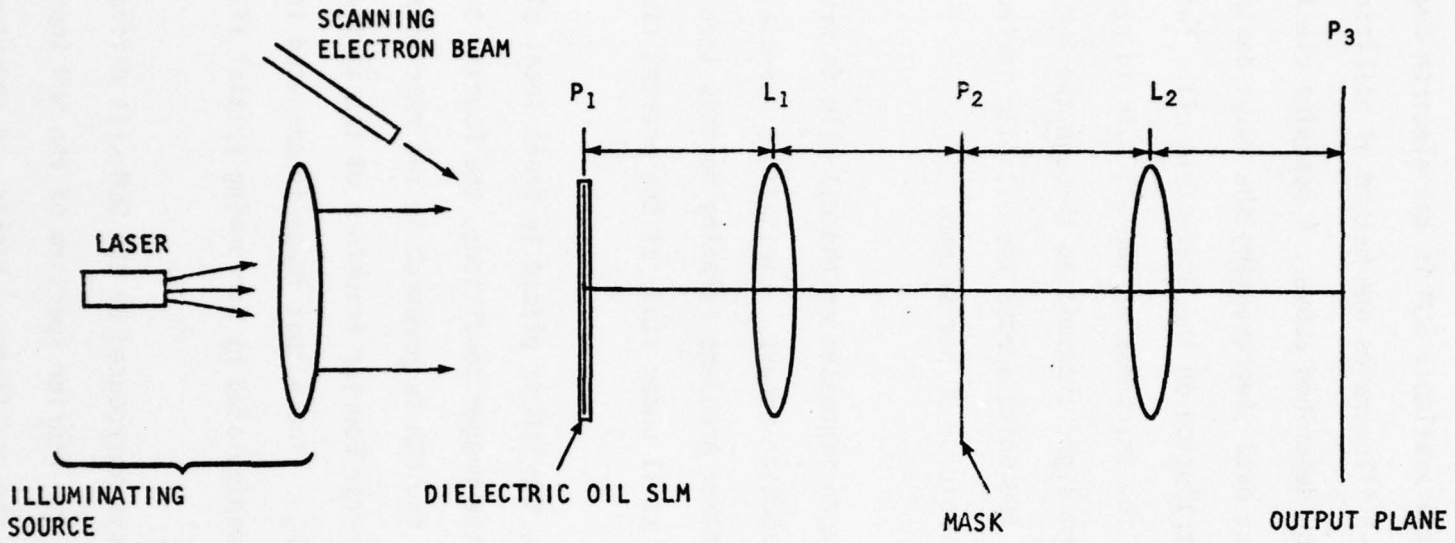

FIGURE E-3. SLM AND OPTICAL SYSTEM FOR IMAGE SYNTHESIS

on-axis. These diffracted components contain the information needed to reconstruct the desired object but they are not readily discernible since they are in phase quadrature with the stronger, undiffracted (zero-order) background components.

One method of viewing the structure contained in the SLM phase pattern is to insert a small opaque stop on the optical axis in plane P_2 to remove the undiffracted components. This technique produces an intensity distribution in output plane P_3 which is not linearly related to the phase delays introduced by the SLM. This may unnecessarily complicate the design of the SLM phase pattern.

Another method uses the Zernike phase-contrast microscope technique to produce an intensity distribution in P_3 which is linearly related to the phase shifts provided one assumes that the phase shifts are less than 1 radian. In this method, the opaque stop is replaced by a transparent stop which will retard the phase of the undiffracted light by $\pi/2$ radians. This removes the phase quadrature relationship between the diffracted and undiffracted components and produces an image intensity which is linearly related to the phase shift.

These are not the only possible solutions (combinations of the two methods described above may be necessary), and further study is necessary to judge the overall viability of this concept.

The deformable SLM's, of which the dielectric oil SLM is one example, consist of materials that experience surface deformations proportional to the data (change) stored on them. Membrane and thermoplastics (a low melting temperature plastic) are other examples of deformable SLM's. The most researched class of SLM's are those using liquid crystals (LC). The latest generation of LC SLM's appear to have long lifetimes, but require different wavelengths of light for the reading and writing of data. However, both Hughes and GE have produced these types commercially, and they have been employed in optical data processing systems.

Another class of SLM's (optically addressed) uses the photodichroism of certain crystals (KCl and NaF are examples) as a means of writing and reading data. These require read and write light sources of different wavelengths and polarizations. Yet another class of SLM's uses crystals that exhibit the Pockels effect. An example is the PROM (Pockels Readout Optical Modulator) available off the shelf from ITEK. This device, as do the most promising of this class, uses $Bi_{12}SiO_{20}$ (bismuth-silicon-oxide) or BSO and DKDP (potassium-dihydrogen-phosphate).

Two other classes of SLM's are the ferroelectric-photoconductor (FE-PC)type and the ferroelectric-photorefractive (FE-PR) type. The FE-PC and FE-PR SLM's have both been used to record helograms. It is not known the extent to which *current* SLM devices can effeciently operate at near UV wavelength; it is clear that in their present form they are not applicable to IR wavelengths. Therefore, the technical risks associated with their use in the present application made the SLM-based designs unfeasible.

E.4 SIDE ILLUMINATION OF DIFFUSING VANES WITH MERCURY CAPILLARY LAMPS

One modification that was considered to enhance the projection capabilities of the UV projector was to illuminate completely diffusing vanes with high pressure mercury capillary arc lamps. The general optical configuration is shown in Figure E-4.

Design rationale for this concept was based on the fact that high pressure mercury capillary arc lamps emit above 70 W of radiated power in the 0.35μm-0.40μm spectral interval. Illumination of the vanes would be provided via a cylindrical collimating lens system, or in essence, a "search light" to flood the vane mechanism with radiation. As a means of providing brighter and more even illumination, two lamps and collimating systems were included in the design concept.

In order to better understand the radiometrics of this design concept, a review of search light geometries as is presented in Appendix B is restated. For simplification it is assumed that the collimating lenses are circular rather than cylindrical. Figure E-4 shows a source, s, at the focal point of a lens, L. The image of the source, s', will be located at infinity. Since S subtends an angle α from L, s' will also subtend α. The irradiance at a point on the optical axis will be determined by the radiance of the image of the source and the solid angle subtended by the image. For points near the lens, the irradiance, H, is given by

$$H = N_s \tau \omega$$

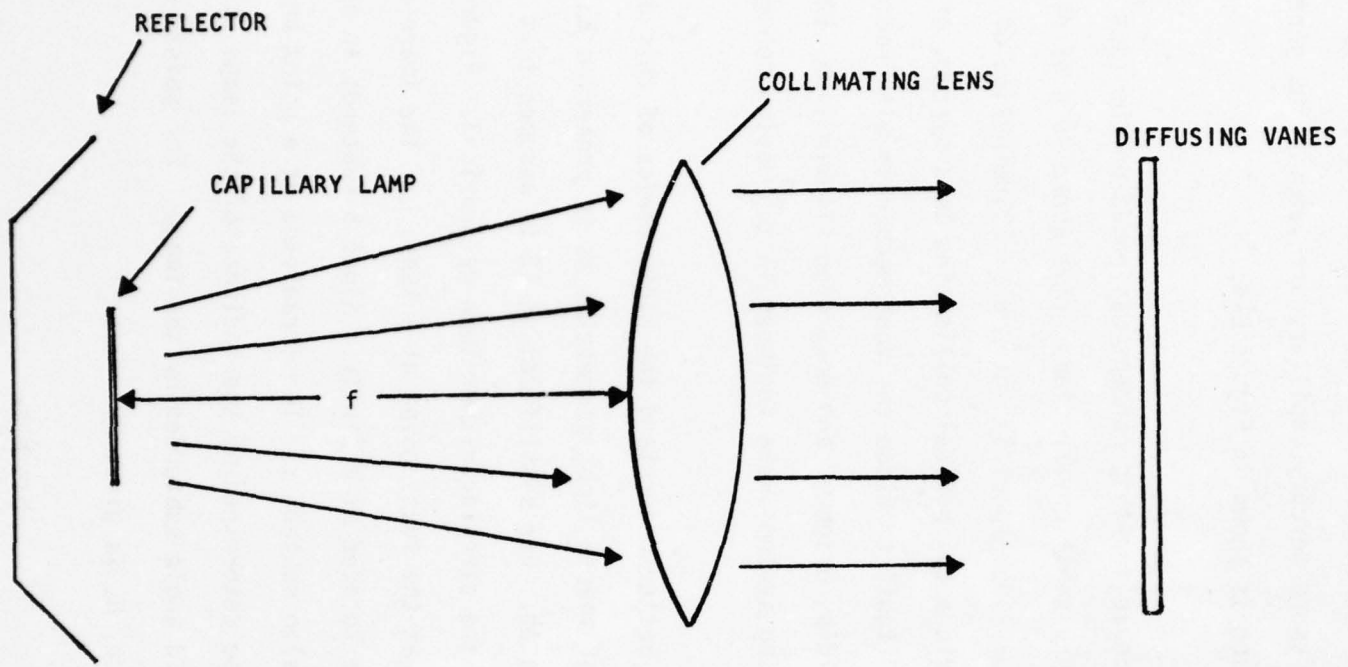

FIGURE E-4. ILLUMINATION OF VANES WITH MERCURY CAPILLARY LAMP

where N_s is the radiance of the source, τ is the transmittance of the lens and ω is the solid angle subtended by the image. For a short distance along the axis, $\omega = \alpha$, the irradiance remains constant along the axis until d = D where D = lens diameter/α. For points where d > D, the size of the solid angle subtended by the source will be limited by the lens diameter or ω = lens area/ d^2 and the irradiance is inversely proportional to d^2. In general then where D = lens diameter/α

$$\text{for } d \leq D: \quad H = N_s \tau \omega = \text{constant}$$

$$\text{for } d > D: \quad H = N_s \tau (\text{lens area} / d^2)$$

Specifications for a Illuminations Industries Incorporated high pressure capillary lamp are given in Table E-1. In order to optimize the illumination onto the vanes and to maintain the present vane size (diameter of approximately 3 inches), a 3 inch diameter collimating lens is assumed. A 1 inch lamp is taken as feasible, and a minimum lamp to lens distance of one foot is allowed for mounting and cooling apparatus as shown in Figure E-5.

TABLE E-1. TECHNICAL DATA FOR MERCURY CAPILLARY LAMP

Electrical Input Power	1 Kw per luminous inch
Length	Lamps vary from 0.5 luminous inch to 4 luminous inches
Overall Length	Lamps vary from 2.7 inches to 8.225 inches
Bore Dimension	2 mm
Total Radiated Power per liminous inch	464 W
Radiated Power from 0.25μ - 0.40μ	78 W
Total Radiance	290 W/cm^2-sr
Radiance from 0.35μ - 0.40μ	49 W/cm^2-sr
Internal Pressure	$\approx$ 80 atm
Water Cooling	$\approx$ 1 gpm

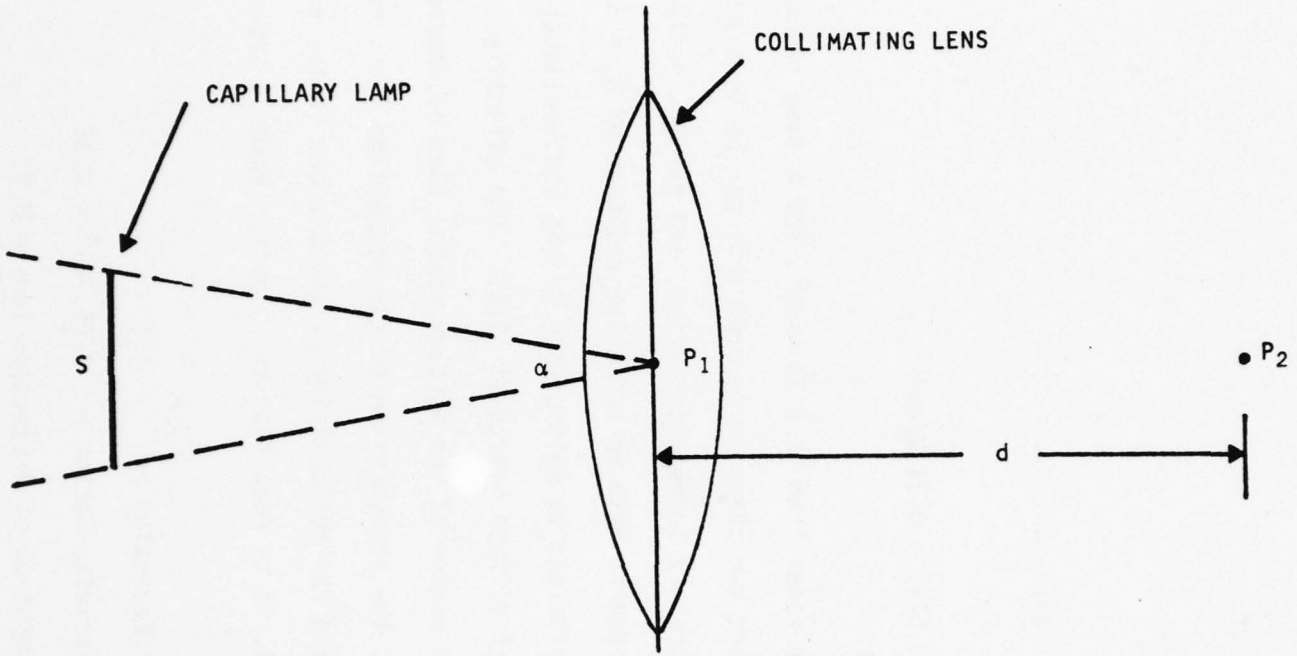

α = ANGLE SUBTENDED BY THE SOURCE AT THE COLLIMATING LENS

ω = SOLID ANGLE SUBTENDED BY THE IMAGE AT ANY POINT P AT DISTANCE d FROM THE LENS

ω = CONSTANT FOR SOME DISTANCE D, A SHORT DISTANCE FROM THE LENS SINCE S' IS AT ∞

FIGURE E-5. SEARCH LIGHT GEOMETRY

For this design geometry

$$\alpha = \frac{A_s}{x^2} = 0.016 \text{ sr}$$

$$D = 762/0.116 = 476 \text{ cm}^2$$

$$H_d = (49)(0.9)(0.016) = 0.71 \text{ W/cm}^2$$

The irradiance onto the vanes then is 0.70 W/cm^2, for a lens transmittance of 0.90. Since there are two lamps to be used this can be doubled to 1.41 W/cm^2. If the vanes are indeed Lambertian, and perfect reflectors, then they act as a new source with an effective radiance of $N_r = H/\pi = 0.45$ W/cm^2-sr. (This is equivalent to multiplying by the bidirectional reflectance of a perfect diffuse source of .318). The effective radiance as seen by the seeker at the display window then is decreased by the pupil expansion, the transmission of the projection lens, reflectance of the vanes, ρ, and the reflectivity of the mirrors in the exterior optics. From Section 6, it is seen that the opacity (inverse transmission) factors are:

Pupil Expansion = 135

Reflectivity Factor = $1/(0.78)^9 = 9.35$

Transmission of Projection lens = 0.92

$\rho \tilde{\sim}$ 0.90 (aluminum, typical)

Hence N_{eff} at display window in using Equation (D-7)

$$N_{eff} = (0.45)(\frac{1}{136})(\frac{1}{9.35})(0.9)(0.9) = 286\ \mu W/cm^2.sr$$

Again, it should be noted that this is assuming a perfectly symmetrically radiating source, and this calculation does not include transmission losses for an additional cylindrical lenses to help even out the illumination in the collimated beam.

Conclusions drawn from these calculations are 1) Even though the capillary lamps have a high UV output, the radiance is not adequate, 2) Cooling of the lamps causes another problem because of extra water lines needed, 3) Design and manufacturer of cylindrical reflectors and clyndrical lenses are not cost effective for this sytem, 4) Vignetting might occur due to removal of the field lens, 5) Cloud wheel imaging capability no longer exists and 6) There is no provision for variable contrast ratios between the background and target.

It is Dynetics opinion that this design concept is not an effective modification to the existing IRSS facility

REFERENCES

3-1. Baessler, R. J., and H. Popper, "Infrared Simulation System (IRSS) Phase 1 Final Report", Contract DAAH01-71-C-0571, July 1971.

5-1. "Spectral Master Infrared Research Radiometer Instruction Manual", Barnes Engineering Company, Stamford, Connecticut.

B-1. Nicodemus, Fred E., "Directional Reflectance and Emissivity of an Opaque Surface", Applied Optics, July 1965, pp 767-773.

B-2. Bennett, H. E., and J. O. Porteus, "Relation Between Surface Roughness and Specular Reflectance at Normal Incidence", JOSA, February 1961, pp 123-129.

B-4. Torrance, K. E., and E. M. Sparrow, "Polarization, Directional Distribution, and Off-Specular Peak Phenomena in Light Reflected From Roughened Surfaces", JOSA, July 1966, pp 916-925.

B-5. Birkebak, R. C., and E. R. G. Eckert, "Effects of Roughness of Metal Surfaces on the Angular Distribution of Reflected Radiation", Journal of Heat Transfer, February 1965, pp 85-93.

C-1. Hass, Georg, and Calvin D. Salzberg, "Optical Properties of Silicon Monoxide in the Wavelength Region From .24 to 14 Microns", JOSA, March 1954, pp 181-187.

C-2. Born, Max, and Emil Wolf, Principles of Optics, Pergamon Press, New York, 1975, pp G11-G13.

C-3. Heavens, O. S., "Optical Properties of Thin Solid Films", Dover Publications, Inc., New York, New York, 1965.

C-4. Hass, G., et. al., "Reflectance and Durability of Ag Mirrors Coated With Thin Layers of Al_2O_3 Plus Reactivity Deposited Silicon Oxide", Applied Optics, November 1975, pp 2369-2371.

DISTRIBUTION

Name of Organization	Number of Copies
Headquarters U.S. Army Missile Research and Development Command ATTN: DRDMI-TD Redstone Arsenal, Alabama 35809	7
Headquarters U.S. Army Missile Research and Development Command ATTN: DRDMI-ICBB/Lukens Redstone Arsenal, Alabama 35809	Letter Only